

12-1-2012

Method of Moments Analysis of an Aperture in a Thick Ground Plane

Ahmet Burak Olcen

Syracuse University, abolcen@yahoo.com

Follow this and additional works at: http://surface.syr.edu/eecs_etd

 Part of the [Electrical and Computer Engineering Commons](#)

Recommended Citation

Olcen, Ahmet Burak, "Method of Moments Analysis of an Aperture in a Thick Ground Plane" (2012). *Electrical Engineering and Computer Science - Dissertations*. Paper 327.

This Dissertation is brought to you for free and open access by the L.C. Smith College of Engineering and Computer Science at SURface. It has been accepted for inclusion in Electrical Engineering and Computer Science - Dissertations by an authorized administrator of SURface. For more information, please contact surface@syr.edu.

ABSTRACT

The problem of electromagnetic scattering from and transmission through an arbitrarily shaped aperture is considered. The aperture is in a thick infinite perfectly conducting ground plane. The conducting walls of the cavity inside the ground plane are of arbitrary shape. The apertures at both ends of the cavity are also of arbitrary shape. The structure is illuminated by an incident plane electromagnetic wave. The Green's function for this complicated problem is almost impossible to determine. Therefore the surface equivalence principle is used to reduce this complex problem into three simpler ones. Each such problem consists of equivalent surface currents radiating in unbounded media. Therefore the free space Green's function is used for each problem. An equivalent surface magnetic current placed on the top aperture produces the scattered field in the region where the impressed sources are. The total field inside the cavity is produced by two surface equivalent magnetic currents on the apertures and an equivalent surface electric current residing on the walls of the cavity as well as on both apertures. The transmitted field on the opposite side of the impressed sources is computed by an equivalent surface magnetic current residing on the bottom aperture. Enforcing the boundary conditions on the tangential components of electric and magnetic fields on both apertures and on the tangential components of electric field on the cavity walls results in a set of three coupled integral equations for the equivalent surface currents. Whenever possible, image theory is used to simplify the equations. These equations are numerically solved using the method of moments. The surfaces are approximated by planar triangular patches. RWG functions are used for expansion functions. An approximate Galerkin method is used for testing. The method is applicable for the general case where all three

regions have different material parameters. Results are computed for the case where all these parameters are the same. The method is applicable for arbitrary sized apertures and cavities. However due to limited computing resources, only problems in the resonance region, where dimensions are comparable to wavelength, are considered here.

Computed results are given for the case of two square apertures connected by a square prism, two cross apertures connected by a square prism cavity, two circular apertures connected by a cylindrical cavity, and finally two circular apertures connected by a conical cavity. Our computed results are compared with results in the literature obtained by using other methods. Very good agreement is observed.

METHOD OF MOMENTS ANALYSIS OF AN APERTURE IN A THICK GROUND PLANE

By

Ahmet Burak Olcen

B.S. Istanbul Technical University, 1999

M.S. Syracuse University, 2002

DISSERTATION

Submitted in partial fulfillment of the requirements for the
degree of Doctor of Philosophy in Electrical Engineering
in the Graduate School of Syracuse University

December 2012

Copyright © 2012 Ahmet Burak Olcen

All Rights Reserved

ACKNOWLEDGMENTS

First, I would like to thank my advisor Dr. Ercument Arvas for his guidance during my time in Syracuse University. Without his support, I wouldn't be able to carry on the heavy burden of the work towards the Ph.D. degree. His advisement on academic matters as well as on my career endeavors has the utmost importance on my achievements so far as a Ph.D. candidate and as an electrical engineer. For this, I am forever indebted to Dr. Arvas. I am honored to work under his supervision and personally, I fell very lucky to be able to receive his mentorship during all these years. His valuable insight had an immense effect on my personal development.

I would also like to thank Dr. Joe Mautz for his careful proofreading of the content and the feedback he provided. During heated discussions with Dr. Mautz, I was amazed by his powerful grasp of the material and realized many intricacies of the work completed in this dissertation.

My parents, Yilmaz and Muberra Olcen, are the sole reason for me to undertake the hardship of getting an education so far away from home. I am humbled by their patience and unending love. I hope I live up to a life which I can make them proud. I am also thankful for my brother Nuri Enes' constant encouragement.

A lot of friends helped me along the way. However, I can't skip without mentioning two of them: Huseyin Erkut and Erdogan Alkan. What wonderful friends a person could have...

Finally, I would like to thank my beloved wife, Busra, for her patience and the comfort she provided. Her devotion is what made me to accomplish this work.

Dedicated to my grandfathers,
Yaşar “Hacı Dede” Ölçen and Nuri Tanrıseven
for instilling the foundation of the moral values
that later became the beacons of my life.

TABLE OF CONTENTS

TABLE OF FIGURES	ix
LIST OF TABLES	xv
CHAPTER 1 INTRODUCTION	1
1.1 The Purpose	1
1.2 The Motivation	3
1.3 The Structure of the Dissertation	6
CHAPTER 2 TRANSMISSION THROUGH AN ARBITRARILY SHAPED APERTURE IN A THICK GROUND PLANE	9
2.1 Application of the Equivalence Principle and Image Theory	11
2.2 Application of the Method of Moments	20
2.3 Setting up the Moment Matrix	23
2.4 Evaluation of the Elements of the Matrices	28
2.5 Calculated Quantities	40
CHAPTER 3 NUMERICAL RESULTS	42
3.1 Results for Square Apertures	42
3.2 Results for a Cross Aperture	49
3.3 Results for Circular Apertures	52
3.4 Effect of Conductor Thickness	55

3.5	Results for Circular Apertures with a Conic Cavity.....	63
3.6	Apertures in Ground Planes of Zero Thickness	66
3.7	Effect of Meshing on Convergence	77
CHAPTER 4	CONCLUSIONS AND FUTURE WORK.....	94
BIBLIOGRAPHY	97
VITA	102

TABLE OF FIGURES

Fig. 1.1	Problem to be solved. (a) top view; (b) cross-section view taken at the outline of (a).	2
Fig. 2.1	Original problem. (a) cross-section view; (b) top view.	10
Fig. 2.2	The equivalent problem for region a	12
Fig. 2.3	Application of image theory to Fig. 2.2.	13
Fig. 2.4	The equivalent problem for region b	14
Fig. 2.5	The equivalence for the cavity region.	15
Fig. 2.6	The equivalent problem for region c	16
Fig. 2.7	Application of image theory to Fig. 2.6.	17
Fig. 2.8	The arbitrarily shaped cavity surface of Fig. 2.4 modeled by triangular patches.	24
Fig. 2.9	Triangle pair and geometrical parameters associated with the n^{th} edge.	25
Fig. 2.10	Geometry of vectors to centroids of triangles associated with an edge.	27
Fig. 3.1	Triangular meshing of the problem with square apertures (0.4λ -by- 0.4λ) on top and bottom; conductor thickness $d = 0.25\lambda$, $\epsilon_a = \epsilon_b = \epsilon_c = \epsilon_0$, $\mu_a = \mu_b = \mu_c = \mu_0$, $\vec{\mathbf{E}}^{\text{inc}} = \vec{\mathbf{x}}e^{jkz}$	43
Fig. 3.2	Electric field along x -axis at the upper (solid line) and lower (dashed line) apertures [29].	44
Fig. 3.3	Electric field at the upper (solid line) and lower (dashed line) apertures.	44
Fig. 3.4	Electric field along y -axis at the upper (solid line) and lower (dashed line) apertures [29].	45
Fig. 3.5	Electric field at the upper (solid line) and lower (dashed line) apertures	45
Fig. 3.6	Backscatter RCS of the structure in Fig. 3.1 as a function of incidence angle in the $\phi = 0^\circ$ plane; $\vec{\mathbf{E}}^{\text{inc}}(\vec{\mathbf{r}}) = (\vec{\boldsymbol{\theta}}^{\text{inc}} \cos \alpha + \vec{\boldsymbol{\phi}}^{\text{inc}} \sin \alpha)e^{-j\vec{\mathbf{k}}^{\text{inc}} \cdot \vec{\mathbf{r}}}$ [29].	47
Fig. 3.7	Backscatter RCS of the structure in Fig. 3.1.	47

Fig. 3.8	Transmission coefficient plots of the structure in Fig. 3.1 as a function of incidence angle in the $\phi = 0^\circ$ plane;	
	$\vec{\mathbf{E}}^{\text{inc}}(\vec{\mathbf{r}}) = (\vec{\mathbf{\theta}}^{\text{inc}} \cos \alpha + \vec{\mathbf{\phi}}^{\text{inc}} \sin \alpha) e^{-j\vec{\mathbf{k}}^{\text{inc}} \cdot \vec{\mathbf{r}}}$ [29].....	48
Fig. 3.9	Transmission coefficient plots of the structure in Fig. 3.1.....	48
Fig. 3.10	Cross shaped aperture with $A = B = 0.5\lambda$, $w = 0.125\lambda$, conductor thickness $d = 0.25\lambda$, $\varepsilon_a = \varepsilon_b = \varepsilon_c = \varepsilon_0$, $\mu_a = \mu_b = \mu_c = \mu_0$	49
Fig. 3.11	Meshing of the problem in Fig. 3.10.	49
Fig. 3.12	Backscatter RCS of the structure in Fig. 3.11 as a function of incidence angle in the $\phi = 0^\circ$ plane; $\vec{\mathbf{E}}^{\text{inc}}(\vec{\mathbf{r}}) = (\vec{\mathbf{\theta}}^{\text{inc}} \cos \alpha + \vec{\mathbf{\phi}}^{\text{inc}} \sin \alpha) e^{-j\vec{\mathbf{k}}^{\text{inc}} \cdot \vec{\mathbf{r}}}$ [29].	50
Fig. 3.13	Backscatter RCS of Fig. 3.11	50
Fig. 3.14	Transmission coefficient plots of the structure in Fig. 3.11 as a function of incidence angle in the $\phi = 0^\circ$ plane;	
	$\vec{\mathbf{E}}^{\text{inc}}(\vec{\mathbf{r}}) = (\vec{\mathbf{\theta}}^{\text{inc}} \cos \alpha + \vec{\mathbf{\phi}}^{\text{inc}} \sin \alpha) e^{-j\vec{\mathbf{k}}^{\text{inc}} \cdot \vec{\mathbf{r}}}$ [29].....	51
Fig. 3.15	Transmission coefficient plots of the structure in Fig. 3.11.	51
Fig. 3.16	A cylindrical cavity with small circular apertures in a thick ground plane [21].	52
Fig. 3.17	Meshing of the structure in Fig. 3.16, $\vec{\mathbf{E}}^{\text{inc}} = \vec{\mathbf{y}} e^{jkz}$	53
Fig. 3.18	Magnetic current on top aperture (solid line) and on bottom aperture (dashed line) along the x -axis for the problem in Fig. 3.16.	54
Fig. 3.19	Magnetic current on top aperture (solid line) and on bottom aperture (dashed line) along the y -axis for the problem in Fig. 3.16.	54
Fig. 3.20	Triangular meshing of the problem with square apertures (0.4λ -by- 0.4λ) on top and bottom; conductor thickness $d = 0.062\lambda$, $\varepsilon_a = \varepsilon_b = \varepsilon_c = \varepsilon_0$, $\mu_a = \mu_b = \mu_c = \mu_0$, $\vec{\mathbf{E}}^{\text{inc}} = \vec{\mathbf{y}} e^{jkz}$	55
Fig. 3.21	Magnetic current on top aperture (solid line) and on bottom aperture (dashed line) along the x -axis for the problem in Fig. 3.20.	56
Fig. 3.22	Magnetic current on top aperture (solid line) and on bottom aperture (dashed line) along the y -axis for the problem in Fig. 3.20.	56

Fig. 3.23	Triangular meshing of the problem with square apertures (0.4λ-by-0.4λ) on top and bottom; conductor thickness $d = 0.125\lambda$, $\varepsilon_a = \varepsilon_b = \varepsilon_c = \varepsilon_0$, $\mu_a = \mu_b = \mu_c = \mu_0$, $\vec{\mathbf{E}}^{\text{inc}} = \vec{\mathbf{y}}e^{jkz}$.	57
Fig. 3.24	Magnetic current on top aperture (solid line) and on bottom aperture (dashed line) along the x -axis for the problem in Fig. 3.23.	58
Fig. 3.25	Magnetic current on top aperture (solid line) and on bottom aperture (dashed line) along the y -axis for the problem in Fig. 3.23.	58
Fig. 3.26	Triangular meshing of the problem with square apertures (0.4λ-by-0.4λ) on top and bottom; conductor thickness $d = 0.5\lambda$, $\varepsilon_a = \varepsilon_b = \varepsilon_c = \varepsilon_0$, $\mu_a = \mu_b = \mu_c = \mu_0$, $\vec{\mathbf{E}}^{\text{inc}} = \vec{\mathbf{y}}e^{jkz}$.	59
Fig. 3.27	Magnetic current on top aperture (solid line) and on bottom aperture (dashed line) along the x -axis for the problem in Fig. 3.26.	60
Fig. 3.28	Magnetic current on top aperture (solid line) and on bottom aperture (dashed line) along the y -axis for the problem in Fig. 3.26.	60
Fig. 3.29	Triangular meshing of the problem with square apertures (0.4λ-by-0.4λ) on top and bottom; conductor thickness $d = 0.75\lambda$, $\varepsilon_a = \varepsilon_b = \varepsilon_c = \varepsilon_0$, $\mu_a = \mu_b = \mu_c = \mu_0$, $\vec{\mathbf{E}}^{\text{inc}} = \vec{\mathbf{y}}e^{jkz}$.	61
Fig. 3.30	Magnetic current on top aperture (solid line) and on bottom aperture (dashed line) along the x -axis for the problem in Fig. 3.29.	62
Fig. 3.31	Magnetic current on top aperture (solid line) and on bottom aperture (dashed line) along the y -axis for the problem in Fig. 3.29.	62
Fig. 3.32	Circular apertures with a conic cavity, $\vec{\mathbf{E}}^{\text{inc}} = \vec{\mathbf{y}}e^{jkz}$.	63
Fig. 3.33	Magnetic current on top aperture (solid line) and on bottom aperture (dashed line) along the x -axis for the problem in Fig. 3.32.	64
Fig. 3.34	Magnetic current on top aperture (solid line) and on bottom aperture (dashed line) along the y -axis for the problem in Fig. 3.32.	64
Fig. 3.35	Backscatter RCS of the structure in Fig. 3.32 as a function of incidence angle in the $\phi = 0^\circ$ plane; solid line: $\vec{\mathbf{E}}^{\text{inc}}$ is phi polarized; dashed line: $\vec{\mathbf{E}}^{\text{inc}}$ is theta polarized.	65

Fig. 3.36	Transmission coefficient plots of the structure in Fig. 3.32 as a function of incidence angle in the $\phi = 0^\circ$ plane; solid line: $\vec{\mathbf{E}}^{\text{inc}}$ is phi polarized; dashed line: $\vec{\mathbf{E}}^{\text{inc}}$ is theta polarized.	65
Fig. 3.37	Triangulation of the circular aperture ($R = 0.25\lambda$) in thin conducting plane, given by Chih Lin I [25].	67
Fig. 3.38	Transmission coefficient for the circular aperture in Fig. 3.37 given by Chih Lin I [25]. x: computed result by [25] for phi polarization; +: computed result by [25] for theta polarization; o, Δ : corresponding data from another reference.	67
Fig. 3.39	Circular aperture with cylindrical cavity, $R = 0.25\lambda$, $d = 0.25\lambda$, $\vec{\mathbf{E}}^{\text{inc}} = \vec{\mathbf{y}}e^{jkz}$	68
Fig. 3.40	Magnetic current on top aperture (solid line) and on bottom aperture (dashed line) along the x -axis for the problem in Fig. 3.39.	69
Fig. 3.41	Magnetic current on top aperture (solid line) and on bottom aperture (dashed line) along the y -axis for the problem in Fig. 3.39.	69
Fig. 3.42	Backscatter RCS of the structure in Fig. 3.39 as a function of incidence angle in the $\phi = 0^\circ$ plane; solid line: $\vec{\mathbf{E}}^{\text{inc}}$ is phi polarized; dashed line: $\vec{\mathbf{E}}^{\text{inc}}$ is theta polarized.	70
Fig. 3.43	Transmission coefficient plots of the structure in Fig. 3.39 as a function of incidence angle in the $\phi = 0^\circ$ plane; solid line: $\vec{\mathbf{E}}^{\text{inc}}$ is phi polarized; dashed line: $\vec{\mathbf{E}}^{\text{inc}}$ is theta polarized.	70
Fig. 3.44	Circular aperture with cylindrical cavity, $R = 0.25\lambda$, $d = 0.1\lambda$, $\vec{\mathbf{E}}^{\text{inc}} = \vec{\mathbf{y}}e^{jkz}$	71
Fig. 3.45	Magnetic current on top aperture (solid line) and on bottom aperture (dashed line) along the x -axis for the problem in Fig. 3.44.	72
Fig. 3.46	Magnetic current on top aperture (solid line) and on bottom aperture (dashed line) along the y -axis for the problem in Fig. 3.44.	72
Fig. 3.47	Backscatter RCS of the structure in Fig. 3.44 as a function of incidence angle in the $\phi = 0^\circ$ plane; solid line: $\vec{\mathbf{E}}^{\text{inc}}$ is phi polarized; dashed line: $\vec{\mathbf{E}}^{\text{inc}}$ is theta polarized.	73

Fig. 3.48	Transmission coefficient plots of the structure in Fig. 3.44 as a function of incidence angle in the $\phi = 0^\circ$ plane; solid line: $\vec{\mathbf{E}}^{\text{inc}}$ is phi polarized; dashed line: $\vec{\mathbf{E}}^{\text{inc}}$ is theta polarized.	73
Fig. 3.49	Circular aperture with cylindrical cavity, $R = 0.25\lambda$, $d = 0.01\lambda$, $\vec{\mathbf{E}}^{\text{inc}} = \vec{\mathbf{y}}e^{jkz}$	74
Fig. 3.50	Magnetic current on top aperture (solid line) and on bottom aperture (dashed line) along the x -axis for the problem in Fig. 3.49.	75
Fig. 3.51	Magnetic current on top aperture (solid line) and on bottom aperture (dashed line) along the y -axis for the problem in Fig. 3.49.	75
Fig. 3.52	Backscatter RCS of the structure in Fig. 3.49 as a function of incidence angle in the $\phi = 0^\circ$ plane; solid line: $\vec{\mathbf{E}}^{\text{inc}}$ is phi polarized; dashed line: $\vec{\mathbf{E}}^{\text{inc}}$ is theta polarized.	76
Fig. 3.53	Transmission coefficient plots of the structure in Fig. 3.49 as a function of incidence angle in the $\phi = 0^\circ$ plane; solid line: $\vec{\mathbf{E}}^{\text{inc}}$ is phi polarized; dashed line: $\vec{\mathbf{E}}^{\text{inc}}$ is theta polarized.	76
Fig. 3.54	The problem of square apertures (0.4λ -by- 0.4λ) with $d = 0.25\lambda$ is meshed with 500 triangles, $\epsilon_a = \epsilon_b = \epsilon_c = \epsilon_0$, $\mu_a = \mu_b = \mu_c = \mu_0$, $\vec{\mathbf{E}}^{\text{inc}} = \vec{\mathbf{y}}e^{jkz}$	79
Fig. 3.55	The problem of square apertures (0.4λ -by- 0.4λ) with $d = 0.25\lambda$ is meshed with 1000 triangles, $\epsilon_a = \epsilon_b = \epsilon_c = \epsilon_0$, $\mu_a = \mu_b = \mu_c = \mu_0$, $\vec{\mathbf{E}}^{\text{inc}} = \vec{\mathbf{y}}e^{jkz}$	80
Fig. 3.56	The problem of square apertures (0.4λ -by- 0.4λ) with $d = 0.25\lambda$ is meshed with 2000 triangles, $\epsilon_a = \epsilon_b = \epsilon_c = \epsilon_0$, $\mu_a = \mu_b = \mu_c = \mu_0$, $\vec{\mathbf{E}}^{\text{inc}} = \vec{\mathbf{y}}e^{jkz}$	81
Fig. 3.57	Magnetic current on the top aperture along the x -axis when the meshing is done using 500, 1000, and 2000 triangles.	82
Fig. 3.58	Magnetic current on the bottom aperture along the x -axis when the meshing is done using 500, 1000, and 2000 triangles.....	82
Fig. 3.59	Magnetic current on the top aperture along the y -axis when the meshing is done using 500, 1000, and 2000 triangles.	83

Fig. 3.60	Magnetic current on the bottom aperture along the y -axis when the meshing is done using 500, 1000, and 2000 triangles.....	83
Fig. 3.61	Backscatter RCS in the $\phi = 0^\circ$ plane when $\vec{\mathbf{E}}^{\text{inc}}$ is theta polarized. The meshing is done using 500, 1000 and 2000 triangles.....	84
Fig. 3.62	Backscatter RCS in the $\phi = 0^\circ$ plane when $\vec{\mathbf{E}}^{\text{inc}}$ is phi polarized. The meshing is done using 500, 1000 and 2000 triangles.....	84
Fig. 3.63	Transmission coefficient plots in the $\phi = 0^\circ$ plane when $\vec{\mathbf{E}}^{\text{inc}}$ is theta polarized. The meshing is done using 500, 1000 and 2000 triangles.	85
Fig. 3.64	Transmission coefficient plots in the $\phi = 0^\circ$ plane when $\vec{\mathbf{E}}^{\text{inc}}$ is phi polarized. The meshing is done using 500, 1000 and 2000 triangles.	85
Fig. 3.65	The problem of square apertures (0.4λ -by- 0.4λ) with $d = 0.25\lambda$ is meshed with 500 refined triangles, $\epsilon_a = \epsilon_b = \epsilon_c = \epsilon_0$, $\mu_a = \mu_b = \mu_c = \mu_0$, $\vec{\mathbf{E}}^{\text{inc}} = \vec{\mathbf{y}}e^{jkz}$	86
Fig. 3.66	The problem of square apertures (0.4λ -by- 0.4λ) with $d = 0.25\lambda$ is meshed with 2000 refined triangles, $\epsilon_a = \epsilon_b = \epsilon_c = \epsilon_0$, $\mu_a = \mu_b = \mu_c = \mu_0$, $\vec{\mathbf{E}}^{\text{inc}} = \vec{\mathbf{y}}e^{jkz}$	87
Fig. 3.67	Magnetic current on the top aperture along the x -axis when the meshing is done using 500 and 2000 triangles. Triangle refinement is applied.....	88
Fig. 3.68	Magnetic current on the bottom aperture along the x -axis when the meshing is done using 500 and 2000 triangles. Triangle refinement is applied.....	88
Fig. 3.69	Magnetic current on the top aperture along the y -axis when the meshing is done using 500 and 2000 triangles. Triangle refinement is applied.....	89
Fig. 3.70	Magnetic current on the bottom aperture along the y -axis when the meshing is done using 500 and 2000 triangles. Triangle refinement is applied.....	89
Fig. 3.71	Backscatter RCS in the $\phi = 0^\circ$ plane when $\vec{\mathbf{E}}^{\text{inc}}$ is theta polarized. The meshing is done using 500 and 2000 triangles. Triangle refinement is applied.....	90
Fig. 3.72	Backscatter RCS in the $\phi = 0^\circ$ plane when $\vec{\mathbf{E}}^{\text{inc}}$ is phi polarized. The meshing is done using 500 and 2000 triangles. Triangle refinement is applied.....	90

Fig. 3.73	Transmission coefficient plots in the $\phi = 0^\circ$ plane when $\vec{\mathbf{E}}^{\text{inc}}$ is theta polarized. The meshing is done using 500 and 2000 triangles. Triangle refinement is applied.	91
Fig. 3.74	Transmission coefficient plots in the $\phi = 0^\circ$ plane when $\vec{\mathbf{E}}^{\text{inc}}$ is phi polarized. The meshing is done using 500 and 2000 triangles. Triangle refinement is applied.	91

LIST OF TABLES

Table. 3.1	Required time and memory for solving the square aperture problem of Section 3.1 while using a mesh of 500, 1000, and 2000 triangles.....	93
------------	--	----

CHAPTER 1

INTRODUCTION

1.1 The Purpose

The coupling of electromagnetic energy through apertures is an important problem in electromagnetic engineering. Many applications, such as aperture antennas, electromagnetic compatibility and interference, electromagnetic pulse interaction with shielded devices, and coupled resonator filters deal with the determination of the fields coupled through apertures.

Specifically, this dissertation investigates electromagnetic transmission through and scattering by an arbitrarily shaped aperture in a thick ground plane. The general problem considered is shown in Fig. 1.1. The ground plane is perfect electric conductor (PEC). It is infinite in $z = 0$ plane and has a thickness of “ d ” in z direction. In this ground plane, two arbitrarily shaped apertures are located on the top and bottom surfaces and arbitrarily shaped cavity walls connect these apertures. Inside this cavity, the medium is linear, homogeneous, and isotropic with (ϵ_b, μ_b) for dielectric permittivity and magnetic permeability. The region above the ground plane has (ϵ_a, μ_a) and the region below the plane has (ϵ_c, μ_c) . A time harmonic plane wave $(\vec{\mathbf{E}}^{\text{inc}}, \vec{\mathbf{H}}^{\text{inc}})$ is incident on the top aperture coming from sources that are infinitely far away. The fields in each region have to be solved for. A method of moment approach is sought to solve for the fields in each region.

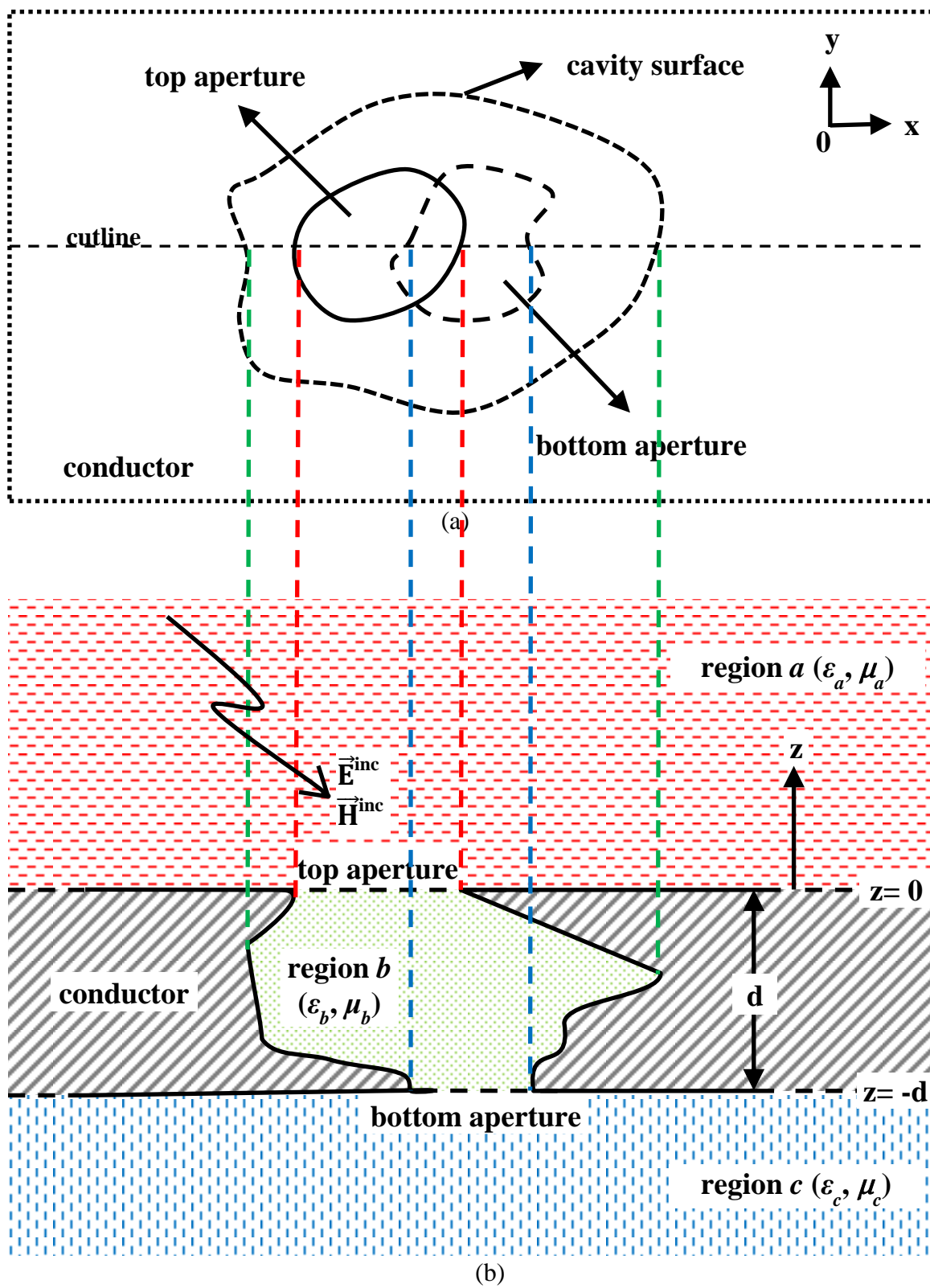


Fig. 1.1 Problem to be solved. (a) top view; (b) cross-section view taken at the cutline of (a).

The equivalence principle is applied to separate each region from the rest and equivalent sources are placed on the boundaries. Integro-differential equations are obtained. Image theory is used whenever it is possible, to simplify the problem. The equations are solved numerically with the moment method. The solution provides the equivalent sources, which then can be used to find the fields or other quantities sought throughout the problem space.

1.2 The Motivation

In 1944, Bethe [1] offered solutions for coupling through a small circular aperture in a conducting plane wall of zero thickness, utilizing electric and magnetic dipole moments. His solution, the so-called aperture polarizability method, has been used extensively as a basis for future research on aperture coupled systems. However, Bethe's solution is suitable for circular apertures only, not applicable to rectangular or more complicated geometrical figures. Bouwkamp [2] worked on small holes and pointed out errors in Bethe's solution. Cohn [3], [4] improved Bethe's work to include arbitrarily shaped apertures in walls of zero thickness. McDonald [5] combined the aperture polarizability method with a waveguide modes method to solve for the coupling through small apertures in plane walls of arbitrary thickness. Chen used waveguide modes to solve the problem of periodic circular apertures in thin plates [6], [7] and later in thick plates [8].

A major breakthrough in dealing with aperture problems came in 1975 when Harrington and Mautz [9] expressed aperture characteristics as admittance matrices, which depend only on the region being considered, being independent of the other region. The aperture coupling is then expressible as the sum of the two independent aperture

admittance matrices. The numeric solution is carried out with the method of moments formulated by Harrington [10]. Many canonical problems can be solved by this approach. After Harrington popularized the method of moments for electromagnetic field problems, many researchers tackled aperture problems by applying moment methods to electric and magnetic field integral equations.

Mautz and Harrington provided the solution for rectangular apertures in thin conducting planes [11], [12] and for rectangular waveguide to rectangular aperture coupling [13]. Butler and Umashankar investigated coupling to a wire through an aperture in a thin plate [14]. Butler, Rahmat-Samii, and Mittra [15] presented a work in 1978 which summarizes different methods employed so far for solving various kinds of aperture problems. Their work mentions integro-differential equations, which are expanded as Rayleigh series; aperture polarizabilities for small apertures; general formulation using equivalence principle and the method of moments. At the end of their work, an extensive bibliography, comprising papers published on apertures till 1978, is provided.

Auckland solved the problem of electromagnetic transmission through a slit in a thick conducting plane, when the cross-section of the slit is rectangular [16] and when it is arbitrarily shaped [17]. Although the cross-section is arbitrarily shaped and the conducting plane is thick, this problem is not a real 3-D problem. Since a slit is defined as having infinite length, slit in a thick conductor becomes a 2-D problem. A technical report by Harrington, Mautz, and Auckland [18] summarizes several problems that were solved using the method of moments.

Another important milestone is the development of expansion functions for moment methods when triangular surface patch modeling is used, brought to fruition by the hard work of Rao [19] and Rao, Wilton, and Glisson [20]. Arbitrarily shaped objects are easier to be modeled by triangular patches and the triangular expansion functions have many properties suited aptly to solve the problem analyzed in this dissertation.

Leviatan, Harrington, and Mautz [21] analyzed the transmission problem when the conducting plane is thick and the aperture is a circular cavity. Arvas solved for radiation and scattering from an arbitrary conducting body [22]. He specifically dealt with the problem in the Rayleigh region where the conducting body is much smaller than the wavelength. This problem separates into an electrostatic problem and a magnetostatic problem. Then Arvas showed that the problem of determining the electric polarizability of a small aperture is the dual of the problem of determining the magnetic polarizability of a conducting disc [23]. In this dissertation, the problem considered is in the resonant region, where the apertures and the cavities are comparable with the wavelength.

Harrington investigated aperture coupling to a cavity when an arbitrarily shaped body existed [24]. Chih-Lin I solved the general problem of arbitrarily shaped apertures in thin plates [25]. An extension of this problem, where the aperture is covered with a mesh, is solved by Sarkar, et al. [26]. Hsi furthered the arbitrarily shaped aperture in thin plane problem by solving for the coupling between such an aperture and a conducting wire [27].

In 1991, Jian-Ming Jin and John L. Volakis presented a solution for 3-D arbitrarily shaped cavities and apertures in thick conducting planes by combining boundary integral methods with the finite element method (FEM) [28], [29]. Their paper

is the one which the results from this research are compared to so as to validate the moment method approach. FEM requires generating a volume mesh to find the fields. However, the formulation based on the method of moments in this dissertation only requires surface meshing to calculate the fields. That makes it inherently faster to obtain results in a computer.

In 1994, Luebbers and Penney devised a method where they can use the finite difference time domain (FDTD) method to solve for the scattering from an arbitrarily shaped aperture in a thin ground plane [30]. In 1999, Park and Eom used Fourier transform and mode matching technique to obtain a fast converging series solution for scattering from rectangular apertures in a thick conducting screen [31]. In 2004, Park and Eom published a paper in which they use the aforementioned method to solve for the electromagnetic transmission through circular apertures in a thick conducting plane [32].

In other notable research related to the area of aperture coupling, modified basis functions developed by Andersson that incorporate the edge and the corner singularities [33] are used; and several papers from 1993 onward concentrate on accurate calculation of the singular integrals faced while using RWG triangular basis functions [34]–[41].

1.3 The Structure of the Dissertation

After the introduction of the problem and the literature survey, the organization of this dissertation is as follows:

Chapter 2 restates the problem to be solved and then describes the solution method in detail. First, the equivalence principle is applied to simplify the problem and to separate the complex problem into three simple regions. The problem is reduced to finding the equivalent sources in each of these regions. Since the problem deals with an

infinite ground plane in two of these regions, image theory can be used and the unknown sources reduced solely to magnetic currents. The integro-differential equations to be solved numerically are obtained at the end of these steps.

Then, the application of the method of moments as a numerical process is described. Discretization of the integro-differential equations is performed. The matrix equation that is going to be solved is obtained.

An important step in the method of moments is to select proper expansion functions. Rao-Wilton-Glissson triangular expansion functions [20] are selected to expand unknown currents. Galerkin's method is used for the testing procedure, where the expansion functions are also used as testing functions.

Evaluation of the matrix elements requires surface integrations of the currents over triangular patches. The evaluation of the double integrals faced during this step is computationally very intensive and places a burden on computer resources. One way to reduce the burden is to use central point approach where the value of a function is assumed to be a constant over a patch. Then, any integral whose integrand is proportional to the function is simplified by replacing the function by its value at the centroid of the triangle. This approximation is used for the integrations with respect to the arguments of the testing functions. However, expansion functions are integrated using well-established numeric methods. Another difficulty faced when calculating the integrals is when the integrands are singular. The singularity extraction method is used where a singular integrand is expressed as a singular but integrable integrand plus a nonsingular integrand. The singular but integrable integrand is integrated analytically and the non-singular integrand is calculated using a Gaussian quadrature rule modified for a triangular domain.

At the end of Chapter 2, the calculation of the fields in each region is formulated using solved equivalent sources.

Chapter 3 presents the computed results for several problem geometries. A MATLAB program is developed based on the formulation of Chapter 2. The program and the formulation are validated by two test cases; a square aperture in a thick conducting plane and a cross aperture in a thick conducting plane. After the validation, results for circular apertures with a cylindrical cavity inside the conductor and a conic cavity inside the conductor are given. The effect of conductor thickness is also shown in a separate section.

An arbitrarily shaped aperture in a thin conducting plane is a special case of the problem treated in this research. The results for an aperture in a thick plane should converge to the results for an aperture in a thin plane when the thickness of the plane goes to zero. This is verified for a circular aperture by starting with a thick conducting plane and reducing the thickness in steps.

Convergence of the computed results is also analyzed in Chapter 3. Results are provided for a sample problem when the number of triangles in a mesh is increased. Also the effect of refining triangles on the aperture edges is investigated.

Chapter 4 presents the conclusions and gives a brief summary.

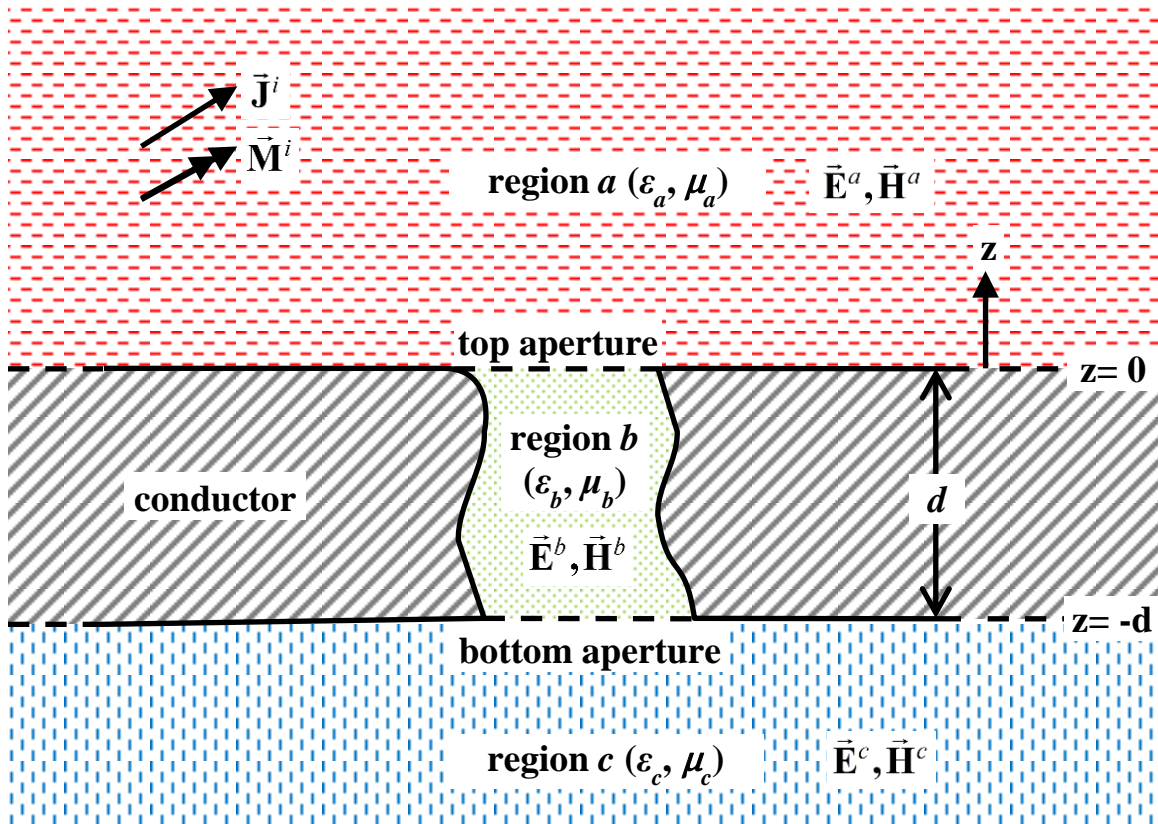
CHAPTER 2

TRANSMISSION THROUGH AN ARBITRARILY SHAPED APERTURE IN A THICK GROUND PLANE

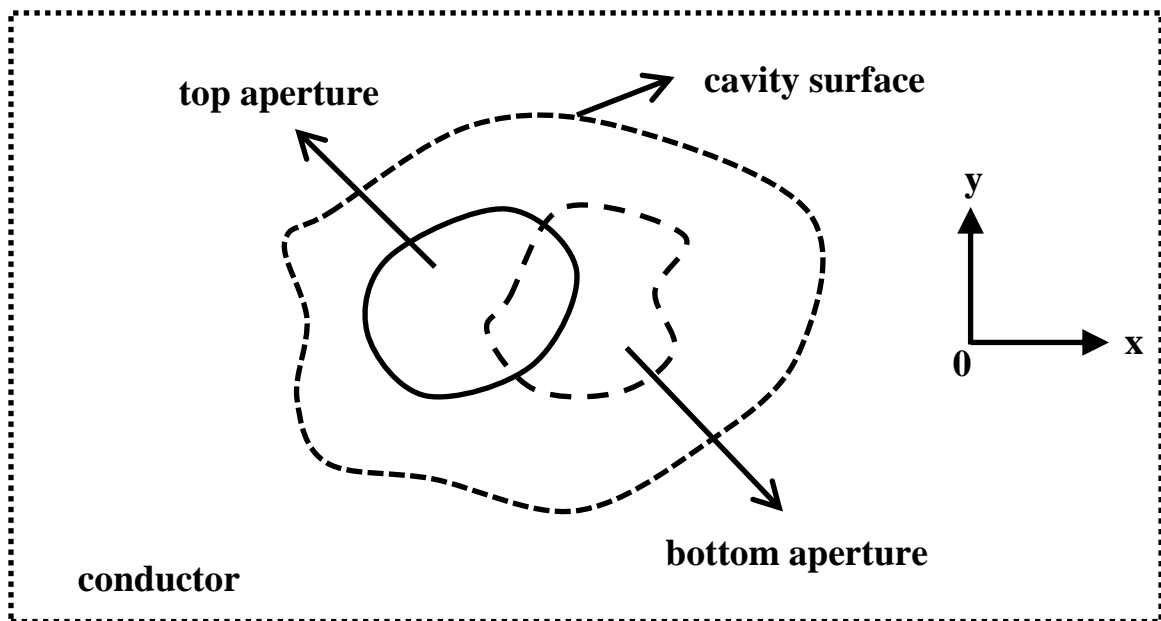
This chapter presents a method of moments solution to the three-dimensional problem of electromagnetic transmission through an arbitrarily shaped aperture in a thick ground plane. The problem geometry is shown in Fig. 2.1.

The ground plane is assumed to be a perfect electric conductor (PEC) of infinite size in x and y directions. It has a finite thickness of “ d ” along the z axis. An arbitrarily shaped aperture exists on each side of the thick ground plane. These apertures are connected with an arbitrarily shaped cavity. The regions above and below the ground plane as well as inside the cavity are linear, homogeneous, isotropic dielectric mediums. These regions are named regions a , b , and c from the top to the bottom. In general, each region has a different electric permittivity (ϵ) and magnetic permeability (μ) than the others. The top region, region a , also contains impressed sources ($\vec{\mathbf{J}}^i, \vec{\mathbf{M}}^i$) far away. These sources excite a time harmonic plane wave which illuminates the ground plane on the top side. The electric and magnetic fields in each region are unknown and they are going to be calculated by applying the equivalence principle, image theory and the method of moments.

The integro-differential expressions for the fields due to sources in an unbounded homogeneous medium are



(a)



(b)

Fig. 2.1 Original problem. (a) cross-section view; (b) top view.

$$\vec{\mathbf{E}}(\vec{\mathbf{r}}) = -j\omega\vec{\mathbf{A}}(\vec{\mathbf{r}}) - \nabla V(\vec{\mathbf{r}}) - \nabla \times \frac{\vec{\mathbf{F}}(\vec{\mathbf{r}})}{\varepsilon} \quad (2.1)$$

$$\vec{\mathbf{H}}(\vec{\mathbf{r}}) = -j\omega\vec{\mathbf{F}}(\vec{\mathbf{r}}) - \nabla U(\vec{\mathbf{r}}) + \nabla \times \frac{\vec{\mathbf{A}}(\vec{\mathbf{r}})}{\mu} \quad (2.2)$$

where the potentials are given by

$$\vec{\mathbf{A}}(\vec{\mathbf{r}}) = \frac{\mu}{4\pi} \iint \vec{\mathbf{J}}(\vec{\mathbf{r}}') G(\vec{\mathbf{r}}, \vec{\mathbf{r}}') ds' \quad (2.3)$$

$$\vec{\mathbf{F}}(\vec{\mathbf{r}}) = \frac{\varepsilon}{4\pi} \iint \vec{\mathbf{M}}(\vec{\mathbf{r}}') G(\vec{\mathbf{r}}, \vec{\mathbf{r}}') ds' \quad (2.4)$$

$$V(\vec{\mathbf{r}}) = j \frac{1}{4\pi\varepsilon\omega} \iint \nabla' \cdot \vec{\mathbf{J}}(\vec{\mathbf{r}}') G(\vec{\mathbf{r}}, \vec{\mathbf{r}}') ds' \quad (2.5)$$

$$U(\vec{\mathbf{r}}) = j \frac{1}{4\pi\mu\omega} \iint \nabla' \cdot \vec{\mathbf{M}}(\vec{\mathbf{r}}') G(\vec{\mathbf{r}}, \vec{\mathbf{r}}') ds' . \quad (2.6)$$

G is the free-space Green's function and it is defined as

$$G(\vec{\mathbf{r}}, \vec{\mathbf{r}}') = \frac{e^{-jk|\vec{\mathbf{r}}-\vec{\mathbf{r}}'|}}{|\vec{\mathbf{r}}-\vec{\mathbf{r}}'|} . \quad (2.7)$$

$\vec{\mathbf{r}}$ is the field point vector and $\vec{\mathbf{r}}'$ is the source point vector. The source currents are taken as surface current densities as evidenced by the double integrals. An $e^{j\omega t}$ time dependence is assumed and suppressed everywhere.

2.1 Application of the Equivalence Principle and Image Theory

The equivalence principle [42] is used to decouple the fields in the three regions of Fig. 2.1a by covering the apertures with PEC and placing equivalent magnetic currents over where we originally had the apertures [9].

The equivalent problem for the top region is shown in Fig. 2.2. The impressed sources ($\vec{\mathbf{J}}^i, \vec{\mathbf{M}}^i$) and the material (ε_a, μ_a) are kept the same as those in the original

problem. The top aperture surface of Fig. 2.1a is now covered by a patch of PEC in Fig. 2.2. Hence, the whole $z=0$ plane in Fig. 2.2 is a PEC. Below this plane, the fields are set to be null fields. The tangential electric field in region a of Fig. 2.1a is zero just above the $z=0$ plane except over the top aperture region. The electric field in the top

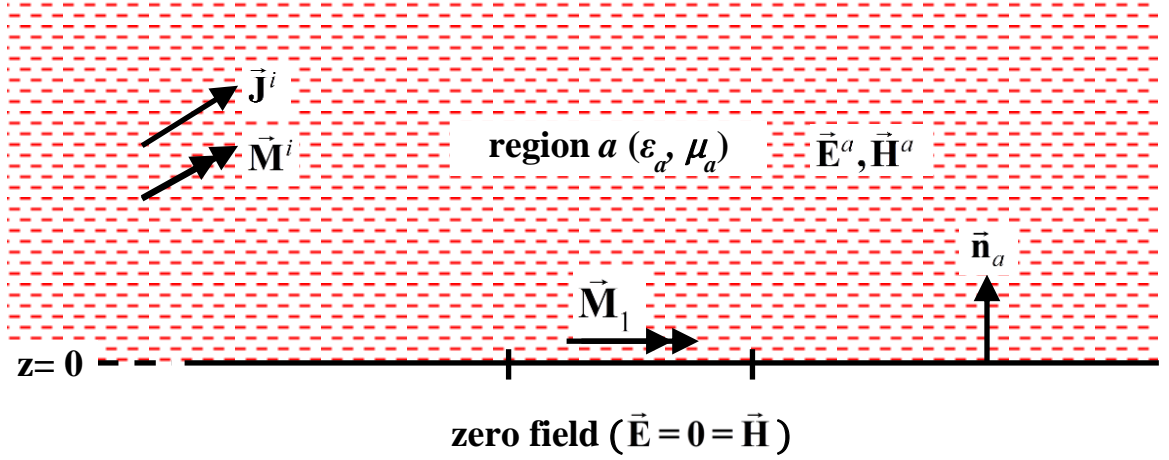


Fig. 2.2 The equivalent problem for region a .

aperture region is $\vec{\mathbf{E}}^a|_{z=0} = \vec{\mathbf{E}}^a|_{z=0^+}$ in Fig. 2.1a. By placing an equivalent magnetic surface current

$$\vec{\mathbf{M}}_1 = \vec{\mathbf{E}}^a|_{z=0^+} \times \vec{\mathbf{n}}_a = \vec{\mathbf{E}}^a|_{z=0^+} \times \vec{\mathbf{z}} \quad (2.8)$$

over this newly placed patch of PEC in Fig. 2.2, we guarantee that the tangential electric field just above this current in Fig. 2.2 is the same as the tangential electric field at the same points of Fig. 2.1. In (2.8), $\vec{\mathbf{z}}$ is the unit vector in the z -direction and $z=0^+$ indicates the limit as z approaches zero from the above. Then the fields in Fig. 2.2, produced by the impressed sources $(\vec{\mathbf{J}}^i, \vec{\mathbf{M}}^i)$ and the equivalent magnetic surface current $\vec{\mathbf{M}}_1$ (residing just above the PEC plane), are identical to $(\vec{\mathbf{E}}^a, \vec{\mathbf{H}}^a)$ in Fig. 2.1. That is,

$$\vec{\mathbf{E}}^a = \vec{\mathbf{E}}^a(\vec{\mathbf{J}}^i, \vec{\mathbf{M}}^i) + \vec{\mathbf{E}}^a(\vec{\mathbf{M}}_1) \quad (2.9)$$

$$\vec{\mathbf{H}}^a = \vec{\mathbf{H}}^a(\vec{\mathbf{J}}^i, \vec{\mathbf{M}}^i) + \vec{\mathbf{H}}^a(\vec{\mathbf{M}}_1). \quad (2.10)$$

The problem in Fig. 2.2 is a radiation problem of current sources over an infinite ground plane in a half-space filled with homogeneous dielectric medium. This type of problem is solved many times before [14], [15], [25] by using image theory.

Fig. 2.3 shows the application of image theory to Fig. 2.2. The ground plane is removed by using image theory and the equivalent magnetic surface current is doubled. Impressed sources also have their images taken. All sources are now radiating in an unbounded homogeneous medium (ϵ_a, μ_a). The fields in region a of Fig. 2.3 are the same as the fields of region a in Fig. 2.1a.

$$\vec{\mathbf{E}}^a = \vec{\mathbf{E}}^a(\vec{\mathbf{J}}^i, \vec{\mathbf{M}}^i) + \vec{\mathbf{E}}^a(\vec{\mathbf{J}}^{i,\text{img}}, \vec{\mathbf{M}}^{i,\text{img}}) + \vec{\mathbf{E}}^a(2\vec{\mathbf{M}}_1) \quad (2.11)$$

$$\vec{\mathbf{H}}^a = \vec{\mathbf{H}}^a(\vec{\mathbf{J}}^i, \vec{\mathbf{M}}^i) + \vec{\mathbf{H}}^a(\vec{\mathbf{J}}^{i,\text{img}}, \vec{\mathbf{M}}^{i,\text{img}}) + \vec{\mathbf{H}}^a(2\vec{\mathbf{M}}_1). \quad (2.12)$$

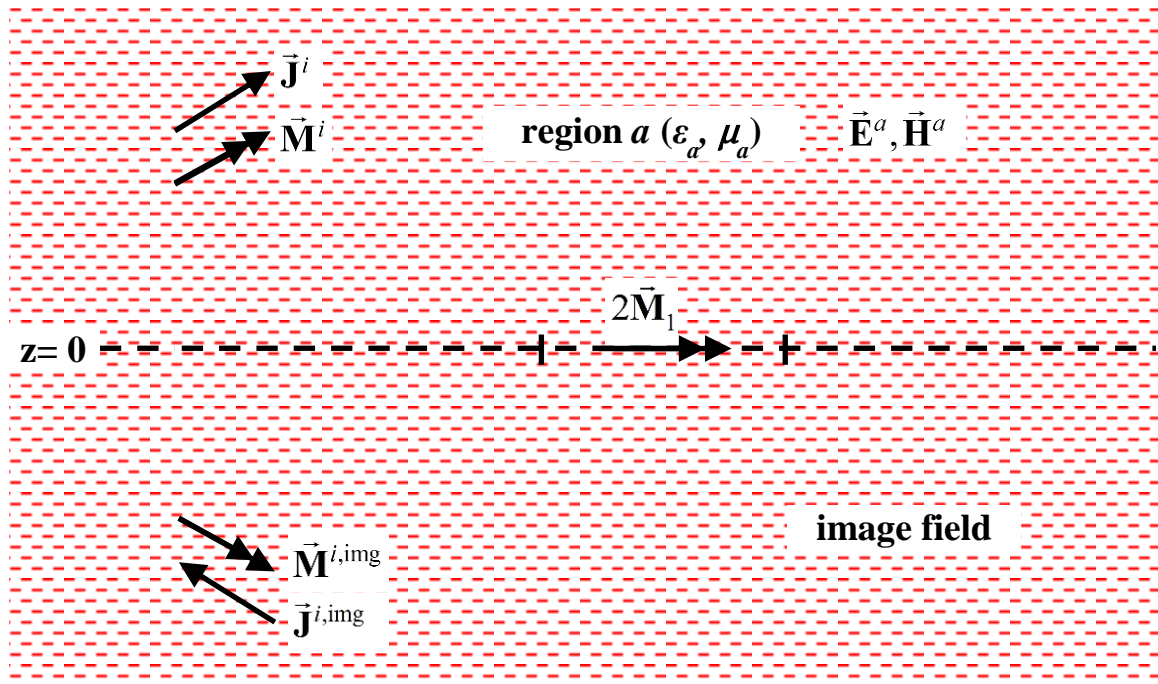


Fig. 2.3 Application of image theory to Fig. 2.2.

The equivalence for region b of Fig. 2.1a is set up as follows: The top and bottom apertures are covered with PEC patches. The material (ϵ_b, μ_b) is kept and the fields outside of region b are set to be zero. Equivalent magnetic surface currents are placed on the newly placed patches inside region b . The values of these currents are chosen to be

$$\text{on top aperture in region } b: -\vec{M}_1 = \vec{E}^b|_{z=0^-} \times \vec{n}_b = \vec{E}^b|_{z=0^-} \times (-\vec{z}) \quad (2.13)$$

$$\text{on bottom aperture in region } b: -\vec{M}_2 = \vec{E}^b|_{z=(-d)^+} \times \vec{n}_b = \vec{E}^b|_{z=(-d)^+} \times \vec{z} \quad (2.14)$$

where \vec{n}_b is the unit vector normal to the conductor pointing into region b and $z=0^-$ indicates the limit as z approaches zero from the below. This equivalent problem for the cavity region is shown in Fig. 2.4.

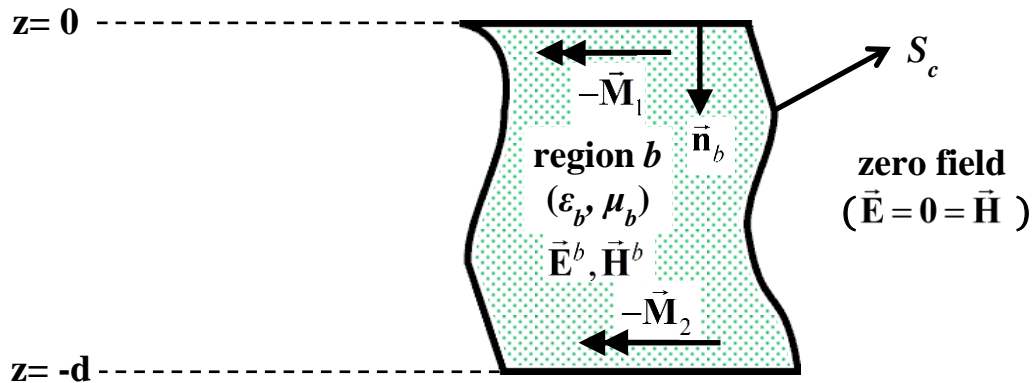


Fig. 2.4 The equivalent problem for region b .

The fields in region b of Fig. 2.4 are due to the equivalent currents radiating in a closed PEC cavity. Solving for these fields requires the knowledge of the arbitrarily shaped cavity's Green's function. However it is impossible to obtain a closed form of the Green's function for such a cavity. In order to overcome this difficulty, another equivalent problem is considered for the cavity region as shown in Fig. 2.5.

$$\vec{\mathbf{E}}^b = \vec{\mathbf{E}}^b(-\vec{\mathbf{M}}_1) + \vec{\mathbf{E}}^b(-\vec{\mathbf{M}}_2) + \vec{\mathbf{E}}^b(\vec{\mathbf{J}}) \quad (2.16)$$

$$\vec{\mathbf{H}}^b = \vec{\mathbf{H}}^b(-\vec{\mathbf{M}}_1) + \vec{\mathbf{H}}^b(-\vec{\mathbf{M}}_2) + \vec{\mathbf{H}}^b(\vec{\mathbf{J}}). \quad (2.17)$$

The boundary condition to be satisfied in this problem is vanishing tangential electric fields over the conductor:

$$\vec{\mathbf{E}}_{\text{tan}}^b = 0 \text{ over cavity surface } (S_c). \quad (2.18)$$

Lastly, the equivalent problem for the bottom region is set up as in Fig. 2.6. This is very similar to the top region equivalent problem with the major difference being not having impressed sources in the bottom region problem. The bottom aperture of Fig. 2.1a is covered by a patch of PEC in Fig. 2.6 and an equivalent magnetic surface current $\vec{\mathbf{M}}_2$ is placed just below this patch in region c . The material (ϵ_c, μ_c) is kept the same as in the original problem. The fields above the $z = -d$ plane are set to be zero. The value of the equivalent magnetic current is

$$\vec{\mathbf{M}}_2 = \vec{\mathbf{E}}^c \Big|_{z=(-d)^-} \times \vec{\mathbf{n}}_c = \vec{\mathbf{E}}^c \Big|_{z=(-d)^-} \times (-\vec{\mathbf{z}}). \quad (2.19)$$

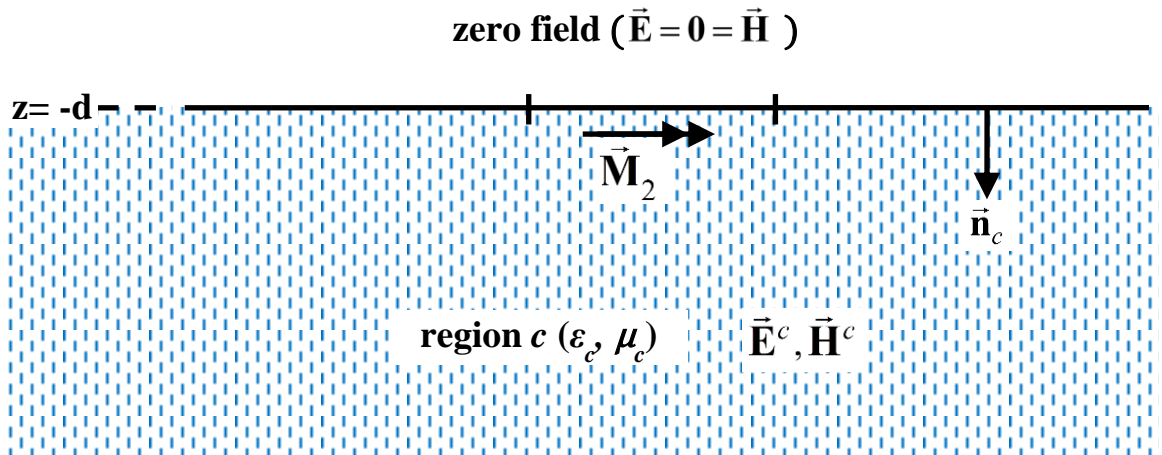


Fig. 2.6 The equivalent problem for region c .

The fields in region c are only due to this equivalent current radiating in the presence of an infinite ground plane. That is,

$$\vec{\mathbf{E}}^c = \vec{\mathbf{E}}^c(\vec{\mathbf{M}}_2) \quad (2.20)$$

$$\vec{\mathbf{H}}^c = \vec{\mathbf{H}}^c(\vec{\mathbf{M}}_2). \quad (2.21)$$

If image theory is used, the ground plane can be removed. In this case, the magnetic current is doubled and it radiates in an unbounded medium filled with (ϵ_c, μ_c) as shown in Fig. 2.7. The fields in region c can be written as

$$\vec{\mathbf{E}}^c = \vec{\mathbf{E}}^c(2\vec{\mathbf{M}}_2) \quad (2.22)$$

$$\vec{\mathbf{H}}^c = \vec{\mathbf{H}}^c(2\vec{\mathbf{M}}_2). \quad (2.23)$$

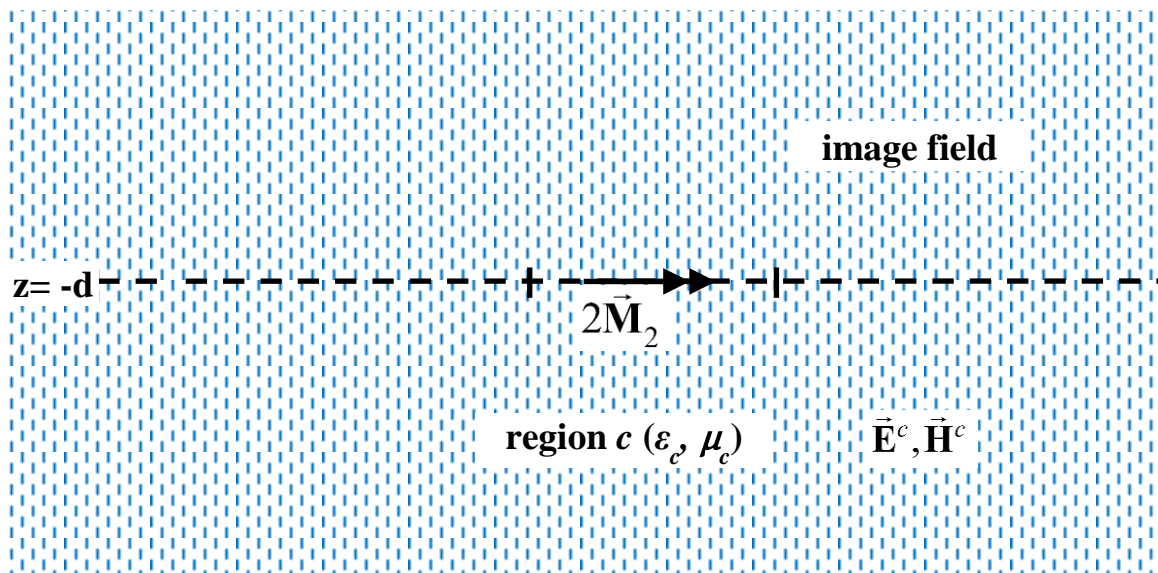


Fig. 2.7 Application of image theory to Fig. 2.6.

After extracting these three equivalent problems from the original problem in Fig. 2.1, the next step is to satisfy the boundary conditions. Thus, the continuity of the tangential electric and magnetic fields across the aperture regions and vanishing tangential electric field over the conductor have to be satisfied.

The first boundary condition, the continuity of the tangential electric field, is automatically satisfied by taking the signs of the magnetic currents residing on each side of an aperture to be opposite each other. This can be seen in (2.8) and (2.13) for $\vec{\mathbf{M}}_1$ and in (2.14) and (2.19) for $\vec{\mathbf{M}}_2$.

The second boundary condition to satisfy is the continuity of tangential magnetic fields across the apertures. In other words;

$$\vec{\mathbf{H}}_{\text{tan}}^a = \vec{\mathbf{H}}_{\text{tan}}^b \text{ across the top aperture} \quad (2.24)$$

$$\vec{\mathbf{H}}_{\text{tan}}^b = \vec{\mathbf{H}}_{\text{tan}}^c \text{ across the bottom aperture.} \quad (2.25)$$

$\vec{\mathbf{H}}_{\text{tan}}^a$, $\vec{\mathbf{H}}_{\text{tan}}^b$ and $\vec{\mathbf{H}}_{\text{tan}}^c$ can be found from (2.12), (2.17) and (2.23) as

$$\vec{\mathbf{H}}_{\text{tan}}^a = \vec{\mathbf{H}}_{\text{tan}}^a(\vec{\mathbf{J}}^i, \vec{\mathbf{M}}^i) + \vec{\mathbf{H}}_{\text{tan}}^a(\vec{\mathbf{J}}^{i,\text{img}}, \vec{\mathbf{M}}^{i,\text{img}}) + \vec{\mathbf{H}}_{\text{tan}}^a(2\vec{\mathbf{M}}_1) \quad (2.26)$$

$$\vec{\mathbf{H}}_{\text{tan}}^b = \vec{\mathbf{H}}_{\text{tan}}^b(-\vec{\mathbf{M}}_1) + \vec{\mathbf{H}}_{\text{tan}}^b(-\vec{\mathbf{M}}_2) + \vec{\mathbf{H}}_{\text{tan}}^b(\vec{\mathbf{J}}) \quad (2.27)$$

$$\vec{\mathbf{H}}_{\text{tan}}^c = \vec{\mathbf{H}}_{\text{tan}}^c(2\vec{\mathbf{M}}_2). \quad (2.28)$$

The tangential magnetic field due to the impressed sources ($\vec{\mathbf{J}}^i, \vec{\mathbf{M}}^i$) and their images is twice the field of the impressed sources radiating in an unbounded medium. So (2.26) can be rewritten as

$$\vec{\mathbf{H}}_{\text{tan}}^a = 2\vec{\mathbf{H}}_{\text{tan}}^{\text{inc}} + \vec{\mathbf{H}}_{\text{tan}}^a(2\vec{\mathbf{M}}_1). \quad (2.29)$$

Using (2.27)–(2.29) in (2.24) and (2.25), the continuity of magnetic fields across apertures can be written as

$$2\vec{\mathbf{H}}_{\text{tan}}^{\text{inc}} + \vec{\mathbf{H}}_{\text{tan}}^a(2\vec{\mathbf{M}}_1) = \vec{\mathbf{H}}_{\text{tan}}^b(-\vec{\mathbf{M}}_1) + \vec{\mathbf{H}}_{\text{tan}}^b(-\vec{\mathbf{M}}_2) + \vec{\mathbf{H}}_{\text{tan}}^b(\vec{\mathbf{J}}) \text{ across top aperture} \quad (2.30)$$

$$\vec{\mathbf{H}}_{\text{tan}}^b(-\vec{\mathbf{M}}_1) + \vec{\mathbf{H}}_{\text{tan}}^b(-\vec{\mathbf{M}}_2) + \vec{\mathbf{H}}_{\text{tan}}^b(\vec{\mathbf{J}}) = \vec{\mathbf{H}}_{\text{tan}}^c(2\vec{\mathbf{M}}_2) \text{ across bottom aperture} \quad (2.31)$$

Any tangential magnetic field due to any magnetic current is continuous across the magnetic current. However, any tangential magnetic field due to any electric current is discontinuous across the electric current so that $\vec{\mathbf{H}}_{\text{tan}}^b(\vec{\mathbf{J}})$ in (2.30) is evaluated at $z = 0^-$ and $\vec{\mathbf{H}}_{\text{tan}}^b(\vec{\mathbf{J}})$ in (2.31) is evaluated at $z = (-d)^+$.

The third boundary condition comes from the equivalent problem for region b in Fig. 2.5; tangential electric field is zero over a perfect electric conductor. Using (2.16) in (2.18), the last boundary equation is found as

$$\vec{\mathbf{E}}_{\text{tan}}^b(-\vec{\mathbf{M}}_1) + \vec{\mathbf{E}}_{\text{tan}}^b(-\vec{\mathbf{M}}_2) + \vec{\mathbf{E}}_{\text{tan}}^b(\vec{\mathbf{J}}) = 0 \text{ on } S_c. \quad (2.32)$$

Any tangential electric field due to any electric current is continuous across the electric current. However, any tangential electric field due to any magnetic current is discontinuous across the magnetic current so that, in (2.32), $\vec{\mathbf{E}}_{\text{tan}}^b(-\vec{\mathbf{M}}_1)$ and $\vec{\mathbf{E}}_{\text{tan}}^b(-\vec{\mathbf{M}}_2)$ are evaluated on S_c with $-\vec{\mathbf{M}}_1$ placed at $z = 0^-$ and $-\vec{\mathbf{M}}_2$ placed at $z = (-d)^+$. Equivalently, $-\vec{\mathbf{M}}_1$ and $-\vec{\mathbf{M}}_2$ could be placed on S_c , $\vec{\mathbf{E}}_{\text{tan}}^b(-\vec{\mathbf{M}}_1)$ evaluated at $z = 0^+$, and $\vec{\mathbf{E}}_{\text{tan}}^b(-\vec{\mathbf{M}}_2)$ evaluated at $z = (-d)^-$.

Using linearity of the fields and arranging terms in equations (2.30)–(2.32), the final form of the integral equations is obtained:

$$-2\vec{\mathbf{H}}_{\text{tan}}^a(\vec{\mathbf{M}}_1) - \vec{\mathbf{H}}_{\text{tan}}^b(\vec{\mathbf{M}}_1) - \vec{\mathbf{H}}_{\text{tan}}^b(\vec{\mathbf{M}}_2) + \vec{\mathbf{H}}_{\text{tan}}^b(\vec{\mathbf{J}}) = 2\vec{\mathbf{H}}_{\text{tan}}^{\text{inc}} \text{ across top aperture} \quad (2.33)$$

$$-\vec{\mathbf{H}}_{\text{tan}}^b(\vec{\mathbf{M}}_1) - \vec{\mathbf{H}}_{\text{tan}}^b(\vec{\mathbf{M}}_2) - 2\vec{\mathbf{H}}_{\text{tan}}^c(\vec{\mathbf{M}}_2) + \vec{\mathbf{H}}_{\text{tan}}^b(\vec{\mathbf{J}}) = 0 \text{ across bottom aperture} \quad (2.34)$$

$$\vec{\mathbf{E}}_{\text{tan}}^b(\vec{\mathbf{M}}_1) + \vec{\mathbf{E}}_{\text{tan}}^b(\vec{\mathbf{M}}_2) - \vec{\mathbf{E}}_{\text{tan}}^b(\vec{\mathbf{J}}) = 0 \text{ on } S_c. \quad (2.35)$$

These three equations are going to be used to solve for the three unknowns, $\vec{\mathbf{M}}_1$, $\vec{\mathbf{M}}_2$ and $\vec{\mathbf{J}}$ by the help of the method of moments.

2.2 Application of the Method of Moments

The integral equations (2.33)–(2.35) are going to be solved numerically by using the method of moments (MoM) [10].

First, the unknowns are approximated by linear combinations of linearly independent expansion functions as

$$\vec{\mathbf{M}}_1 = \sum_{n=1}^{N_a} v_n \vec{\mathbf{M}}_{1n} \quad (2.36)$$

$$\vec{\mathbf{M}}_2 = \sum_{n=1}^{N_c} u_n \vec{\mathbf{M}}_{2n} \quad (2.37)$$

$$\vec{\mathbf{J}} = \sum_{n=1}^{N_b} y_n \vec{\mathbf{J}}_n \quad (2.38)$$

where v_n, u_n and y_n are coefficients to be determined. Equations (2.36)–(2.38) are substituted for $\vec{\mathbf{M}}_1, \vec{\mathbf{M}}_2$ and $\vec{\mathbf{J}}$ in (2.33)–(2.35):

$$-2 \sum_{n=1}^{N_a} v_n \vec{\mathbf{H}}_{\tan}^a(\vec{\mathbf{M}}_{1n}) - \sum_{n=1}^{N_a} v_n \vec{\mathbf{H}}_{\tan}^b(\vec{\mathbf{M}}_{1n}) - \sum_{n=1}^{N_c} u_n \vec{\mathbf{H}}_{\tan}^b(\vec{\mathbf{M}}_{2n}) + \sum_{n=1}^{N_b} y_n \vec{\mathbf{H}}_{\tan}^b(\vec{\mathbf{J}}_n) = 2\vec{\mathbf{H}}_{\tan}^{\text{inc}} \text{ on top} \quad (2.39)$$

$$-\sum_{n=1}^{N_a} v_n \vec{\mathbf{H}}_{\tan}^b(\vec{\mathbf{M}}_{1n}) - \sum_{n=1}^{N_c} u_n \vec{\mathbf{H}}_{\tan}^b(\vec{\mathbf{M}}_{2n}) - 2 \sum_{n=1}^{N_c} u_n \vec{\mathbf{H}}_{\tan}^c(\vec{\mathbf{M}}_{2n}) + \sum_{n=1}^{N_b} y_n \vec{\mathbf{H}}_{\tan}^b(\vec{\mathbf{J}}_n) = 0 \text{ on bottom} \quad (2.40)$$

$$\sum_{n=1}^{N_a} v_n \vec{\mathbf{E}}_{\tan}^b(\vec{\mathbf{M}}_{1n}) + \sum_{n=1}^{N_c} u_n \vec{\mathbf{E}}_{\tan}^b(\vec{\mathbf{M}}_{2n}) - \sum_{n=1}^{N_b} y_n \vec{\mathbf{E}}_{\tan}^b(\vec{\mathbf{J}}_n) = 0 \text{ on } S_c. \quad (2.41)$$

Next, sets of testing functions $\vec{\mathbf{W}}_{1m}, \vec{\mathbf{W}}_{2m}$, and $\vec{\mathbf{T}}_m$ ($m = 1, 2, \dots, N_a, N_c, N_b$, respectively) are defined for the top aperture, the bottom aperture, and the cavity region respectively. Also the following symmetric products of two vector functions are defined:

$$\langle \vec{\mathbf{A}}, \vec{\mathbf{B}} \rangle_{\text{top}} = \iint_{\text{top}} \vec{\mathbf{A}} \cdot \vec{\mathbf{B}} \, ds \text{ on top aperture} \quad (2.42)$$

$$\langle \vec{\mathbf{A}}, \vec{\mathbf{B}} \rangle_{\text{bot}} = \iint_{\text{bot}} \vec{\mathbf{A}} \cdot \vec{\mathbf{B}} \, ds \text{ on bottom aperture} \quad (2.43)$$

$$\langle \vec{\mathbf{A}}, \vec{\mathbf{B}} \rangle_{S_c} = \iint_{S_c} \vec{\mathbf{A}} \cdot \vec{\mathbf{B}} \, ds \text{ on } S_c. \quad (2.44)$$

The last step is to take symmetric products of (2.39)–(2.41) with the testing functions. The following equations are obtained:

$$\begin{aligned} & -2 \sum_{n=1}^{N_a} v_n \langle \vec{\mathbf{W}}_{1m}, \vec{\mathbf{H}}_{\text{tan}}^a(\vec{\mathbf{M}}_{1n}) \rangle_{\text{top}} - \sum_{n=1}^{N_a} v_n \langle \vec{\mathbf{W}}_{1m}, \vec{\mathbf{H}}_{\text{tan}}^b(\vec{\mathbf{M}}_{1n}) \rangle_{\text{top}} - \sum_{n=1}^{N_c} u_n \langle \vec{\mathbf{W}}_{1m}, \vec{\mathbf{H}}_{\text{tan}}^b(\vec{\mathbf{M}}_{2n}) \rangle_{\text{top}} \\ & + \sum_{n=1}^{N_b} y_n \langle \vec{\mathbf{W}}_{1m}, \vec{\mathbf{H}}_{\text{tan}}^b(\vec{\mathbf{J}}_n) \rangle_{\text{top}} = 2 \langle \vec{\mathbf{W}}_{1m}, \vec{\mathbf{H}}_{\text{tan}}^{\text{inc}} \rangle_{\text{top}}, \end{aligned} \quad (m = 1, 2, \dots, N_a) \quad (2.45)$$

$$\begin{aligned} & - \sum_{n=1}^{N_a} v_n \langle \vec{\mathbf{W}}_{2m}, \vec{\mathbf{H}}_{\text{tan}}^b(\vec{\mathbf{M}}_{1n}) \rangle_{\text{bot}} - \sum_{n=1}^{N_c} u_n \langle \vec{\mathbf{W}}_{2m}, \vec{\mathbf{H}}_{\text{tan}}^b(\vec{\mathbf{M}}_{2n}) \rangle_{\text{bot}} - 2 \sum_{n=1}^{N_c} u_n \langle \vec{\mathbf{W}}_{2m}, \vec{\mathbf{H}}_{\text{tan}}^c(\vec{\mathbf{M}}_{2n}) \rangle_{\text{bot}} \\ & + \sum_{n=1}^{N_b} y_n \langle \vec{\mathbf{W}}_{2m}, \vec{\mathbf{H}}_{\text{tan}}^b(\vec{\mathbf{J}}_n) \rangle_{\text{bot}} = 0, \end{aligned} \quad (m = 1, 2, \dots, N_c) \quad (2.46)$$

$$\begin{aligned} & \sum_{n=1}^{N_a} v_n \langle \vec{\mathbf{T}}_m, \vec{\mathbf{E}}_{\text{tan}}^b(\vec{\mathbf{M}}_{1n}) \rangle_{S_c} + \sum_{n=1}^{N_c} u_n \langle \vec{\mathbf{T}}_m, \vec{\mathbf{E}}_{\text{tan}}^b(\vec{\mathbf{M}}_{2n}) \rangle_{S_c} - \sum_{n=1}^{N_b} y_n \langle \vec{\mathbf{T}}_m, \vec{\mathbf{E}}_{\text{tan}}^b(\vec{\mathbf{J}}_n) \rangle_{S_c} = 0, \\ & (m = 1, 2, \dots, N_b). \end{aligned} \quad (2.47)$$

This set of equations can also be written in a matrix form:

$$\begin{bmatrix} [Y_{11mn}]_{N_a \times N_a} & [Y_{12mn}]_{N_a \times N_c} & [D_{13mn}]_{N_a \times N_b} \\ [Y_{21mn}]_{N_c \times N_a} & [Y_{22mn}]_{N_c \times N_c} & [D_{23mn}]_{N_c \times N_b} \\ [C_{31mn}]_{N_b \times N_a} & [C_{32mn}]_{N_b \times N_c} & [Z_{33mn}]_{N_b \times N_b} \end{bmatrix} \begin{bmatrix} [v_n]_{N_a} \\ [u_n]_{N_c} \\ [y_n]_{N_b} \end{bmatrix} = \begin{bmatrix} [2 \langle \vec{\mathbf{W}}_{1m}, \vec{\mathbf{H}}_{\text{tan}}^{\text{inc}} \rangle_{\text{top}}]_{N_a} \\ [0]_{N_c} \\ [0]_{N_b} \end{bmatrix} \quad (2.48)$$

where the matrix elements are

$$[Y_{11mn}] = \left[-2 \langle \vec{\mathbf{W}}_{1m}, \vec{\mathbf{H}}_{\text{tan}}^a(\vec{\mathbf{M}}_{1n}) \rangle_{\text{top}} - \langle \vec{\mathbf{W}}_{1m}, \vec{\mathbf{H}}_{\text{tan}}^b(\vec{\mathbf{M}}_{1n}) \rangle_{\text{top}} \right]_{N_a \times N_a} \quad (2.49)$$

$$[Y_{12mn}] = \left[- \langle \vec{\mathbf{W}}_{1m}, \vec{\mathbf{H}}_{\text{tan}}^b(\vec{\mathbf{M}}_{2n}) \rangle_{\text{top}} \right]_{N_a \times N_c} \quad (2.50)$$

$$[D_{13mn}] = \left[\left\langle \vec{\mathbf{W}}_{1m}, \vec{\mathbf{H}}_{\tan}^b(\vec{\mathbf{J}}_n) \right\rangle_{\text{top}} \right]_{N_a \times N_b} \quad (2.51)$$

$$[Y_{21mn}] = \left[-\left\langle \vec{\mathbf{W}}_{2m}, \vec{\mathbf{H}}_{\tan}^b(\vec{\mathbf{M}}_{1n}) \right\rangle_{\text{bot}} \right]_{N_c \times N_a} \quad (2.52)$$

$$[Y_{22mn}] = \left[-\left\langle \vec{\mathbf{W}}_{2m}, \vec{\mathbf{H}}_{\tan}^b(\vec{\mathbf{M}}_{2n}) \right\rangle_{\text{bot}} - 2\left\langle \vec{\mathbf{W}}_{2m}, \vec{\mathbf{H}}_{\tan}^c(\vec{\mathbf{M}}_{2n}) \right\rangle_{\text{bot}} \right]_{N_c \times N_c} \quad (2.53)$$

$$[D_{23mn}] = \left[\left\langle \vec{\mathbf{W}}_{2m}, \vec{\mathbf{H}}_{\tan}^b(\vec{\mathbf{J}}_n) \right\rangle_{\text{bot}} \right]_{N_c \times N_b} \quad (2.54)$$

$$[C_{31mn}] = \left[\left\langle \vec{\mathbf{T}}_m, \vec{\mathbf{E}}_{\tan}^b(\vec{\mathbf{M}}_{1n}) \right\rangle_{S_c} \right]_{N_b \times N_a} \quad (2.55)$$

$$[C_{32mn}] = \left[\left\langle \vec{\mathbf{T}}_m, \vec{\mathbf{E}}_{\tan}^b(\vec{\mathbf{M}}_{2n}) \right\rangle_{S_c} \right]_{N_b \times N_c} \quad (2.56)$$

$$[Z_{33mn}] = \left[-\left\langle \vec{\mathbf{T}}_m, \vec{\mathbf{E}}_{\tan}^b(\vec{\mathbf{J}}_n) \right\rangle_{S_c} \right]_{N_b \times N_b} . \quad (2.57)$$

The first matrix in (2.48) is called the moment matrix which is a square matrix with a size of $(N_a + N_b + N_c)$ by $(N_a + N_b + N_c)$. The second matrix is the coefficients matrix which is a column vector of dimension $(N_a + N_b + N_c)$. It contains the unknown coefficients that need to be solved. The matrix on the right side of (2.48) is the excitation matrix which is a column vector of dimension $(N_a + N_b + N_c)$.

In (2.51) and (2.54), the unit normal vector, which is $\vec{\mathbf{n}}_b$, points into region b and $\vec{\mathbf{H}}_{\tan}^b(\vec{\mathbf{J}}_n)$ is evaluated on the side of the electric current sheet $\vec{\mathbf{J}}_n$ facing region b . In (2.55) and (2.56), the unit normal vector points into the complement of region b , $\vec{\mathbf{E}}_{\tan}^b(\vec{\mathbf{M}}_{1n})$ is evaluated on the side of the magnetic current sheet $\vec{\mathbf{M}}_{1n}$ facing the complement of region b , and $\vec{\mathbf{E}}_{\tan}^b(\vec{\mathbf{M}}_{2n})$ is evaluated on the side of the magnetic current sheet $\vec{\mathbf{M}}_{2n}$ facing the complement of region b .

The matrix elements in (2.49)–(2.57) are evaluated by first placing $\vec{\mathbf{M}}_{1n}$ at $z = 0$, $\vec{\mathbf{M}}_{2n}$ at $z = -d$, and $\vec{\mathbf{J}}$ on S_c and then evaluating $\vec{\mathbf{H}}_{\text{tan}}^b(\vec{\mathbf{J}}_n)$ in (2.51) at $z = 0^-$, $\vec{\mathbf{H}}_{\text{tan}}^b(\vec{\mathbf{J}}_n)$ in (2.54) at $z = (-d)^+$, $\vec{\mathbf{E}}_{\text{tan}}^b(\vec{\mathbf{M}}_{1n})$ in (2.55) at $z = 0^+$, and $\vec{\mathbf{E}}_{\text{tan}}^b(\vec{\mathbf{M}}_{2n})$ in (2.56) at $z = (-d)^-$.

The moment matrix will be set up by selecting proper expansion and testing functions.

2.3 Setting up the Moment Matrix

The discretization of the integral equations (2.33)–(2.35) by the method of moments requires subdividing the surfaces that have unknown equivalent currents into smaller elements. That means the top aperture surface, the bottom aperture surface and “the cavity surface” of Fig. 2.1 have to be patched by simple elements and then suitable expansion functions have to be applied to these subdomains.

Planar triangular patch modeling is well-developed for arbitrarily shaped surfaces [19]. Triangular patches have the advantage of conforming to any surface easily, they permit greater resolution to be used on boundaries, and the vertices of triangular patches can be set up independently which makes them easier to input on a computer. These patches can be generated manually per the rules defined in [19, pp. 137-147] or by the help of a program specifically written to generate high-quality meshes [43] [38]. Fig. 2.8 shows a triangular patched model of the entire surface of the cavity in Fig. 2.4.

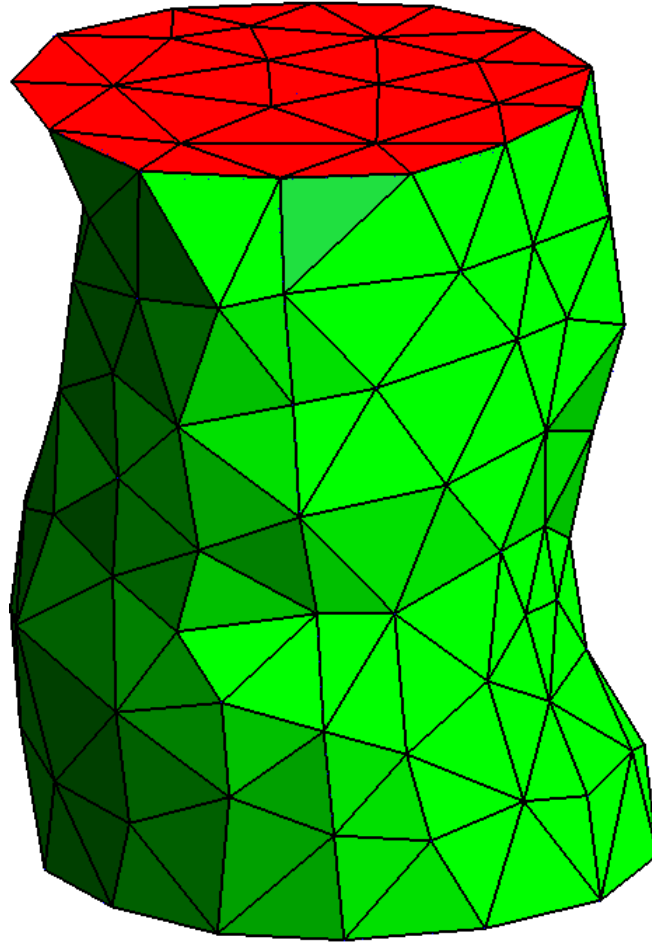


Fig. 2.8 The arbitrarily shaped cavity surface of Fig. 2.4 modeled by triangular patches.

After dividing the whole structure into subdomains, suitable expansion functions such as the ones developed by Rao-Wilton-Glisson [20] are applied. RWG expansion functions are generated for each edge that is common to two triangles. That means if an edge is on the boundary, no expansion function is associated with that edge. A triangle pair with a common edge and geometrical parameters associated with that edge is shown in Fig. 2.9.

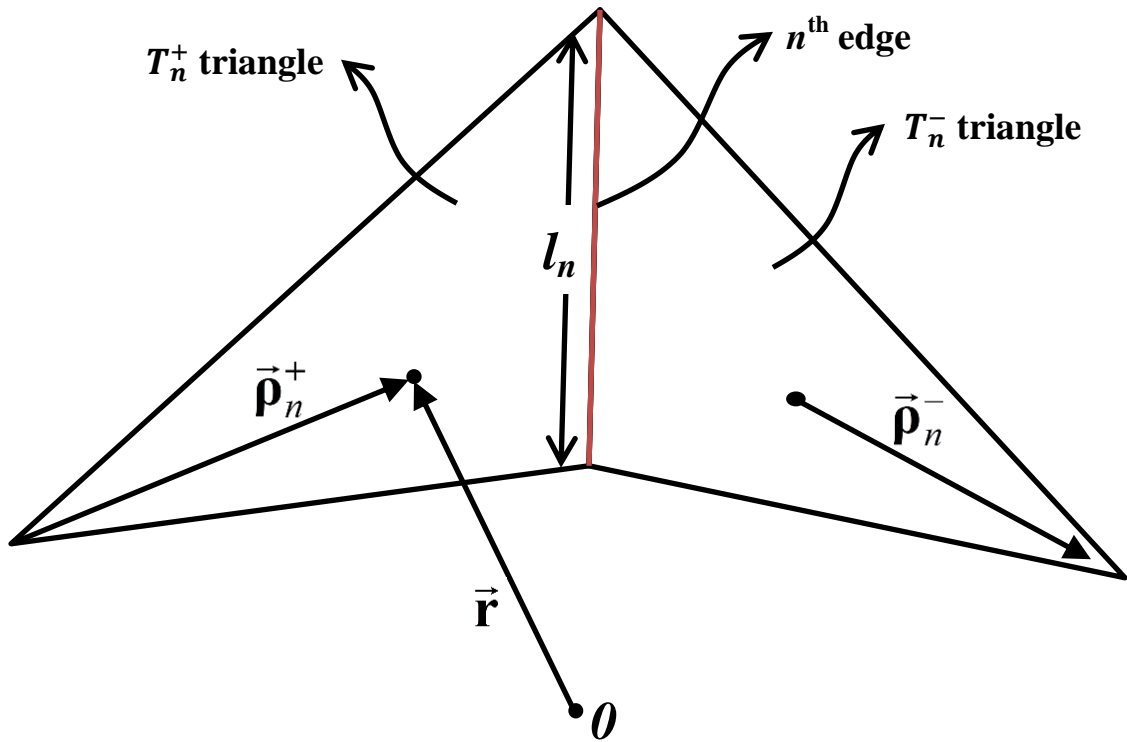


Fig. 2.9 Triangle pair and geometrical parameters associated with the n^{th} edge.

The expansion function associated with the n^{th} edge is defined as

$$\vec{f}_n(\vec{r}) = \begin{cases} \frac{l_n}{2A_n^+} \vec{\rho}_n^+, & \vec{r} \text{ in } T_n^+ \\ \frac{l_n}{2A_n^-} \vec{\rho}_n^-, & \vec{r} \text{ in } T_n^- \\ 0, & \text{otherwise.} \end{cases} \quad (2.58)$$

l_n is the length of the edge, A_n^+ is the area of T_n^+ triangle, A_n^- is the area of T_n^- triangle, $\vec{\rho}_n^+$ is the position vector of a point in T_n^+ with respect to the free vertex of T_n^+ and its direction is away from the vertex, and $\vec{\rho}_n^-$ is the position vector of a point in T_n^- with respect to the free vertex of T_n^- and its direction is toward the vertex. The designation of

T_n^+ and T_n^- for the triangle pair means that the reference direction for current flow across the common edge is from T_n^+ into T_n^- . $\vec{\mathbf{r}}$ is the global position vector of a point with respect to global O .

RWG functions are uniquely suited to express surface currents because of the following properties [20]:

- 1) The expansion function $\vec{\mathbf{f}}_n$ has no component normal to the boundary of the surface formed by the associated triangle pair, and hence no line charges exist along the boundary.
- 2) The component of $\vec{\mathbf{f}}_n$ normal to the n^{th} edge is unity and continuous across the edge. This ensures continuity of current normal to the edge. This result, together with 1), implies that all edges of T_n^+ and T_n^- are free of line charges.
- 3) The surface divergence of $\vec{\mathbf{f}}_n$, which is proportional to the surface charge density is

$$\nabla_s \cdot \vec{\mathbf{f}}_n(\vec{\mathbf{r}}) = \begin{cases} \frac{l_n}{A_n^+}, & \vec{\mathbf{r}} \text{ in } T_n^+ \\ -\frac{l_n}{A_n^-}, & \vec{\mathbf{r}} \text{ in } T_n^- \\ 0, & \text{otherwise,} \end{cases} \quad (2.59)$$

where the surface divergence in T_n^\pm is $\pm \frac{1}{\rho_n^\pm} \frac{d}{d\rho_n^\pm} (\rho_n^\pm f_n)$ where $\rho_n^\pm = |\vec{\mathbf{p}}_n^\pm|$ and

$f_n = |\vec{\mathbf{f}}_n|$. The charge density is thus constant in each triangle and the total charge

associated with the triangle pair T_n^+ and T_n^- is zero.

4) The moment of $\vec{\mathbf{f}}_n$ is given by

$$\iint_{T_n^\pm} \vec{\mathbf{f}}_n ds = \frac{l_n}{2} \vec{\rho}_n^{c\pm} \quad (2.60)$$

where $\vec{\rho}_n^{c\pm}$ is a vector defined between the free vertex and the centroid of T_n^\pm with

$\vec{\rho}_n^{c+}$ directed away from the vertex and $\vec{\rho}_n^{c-}$ directed toward the vertex as shown in

Fig. 2.10.

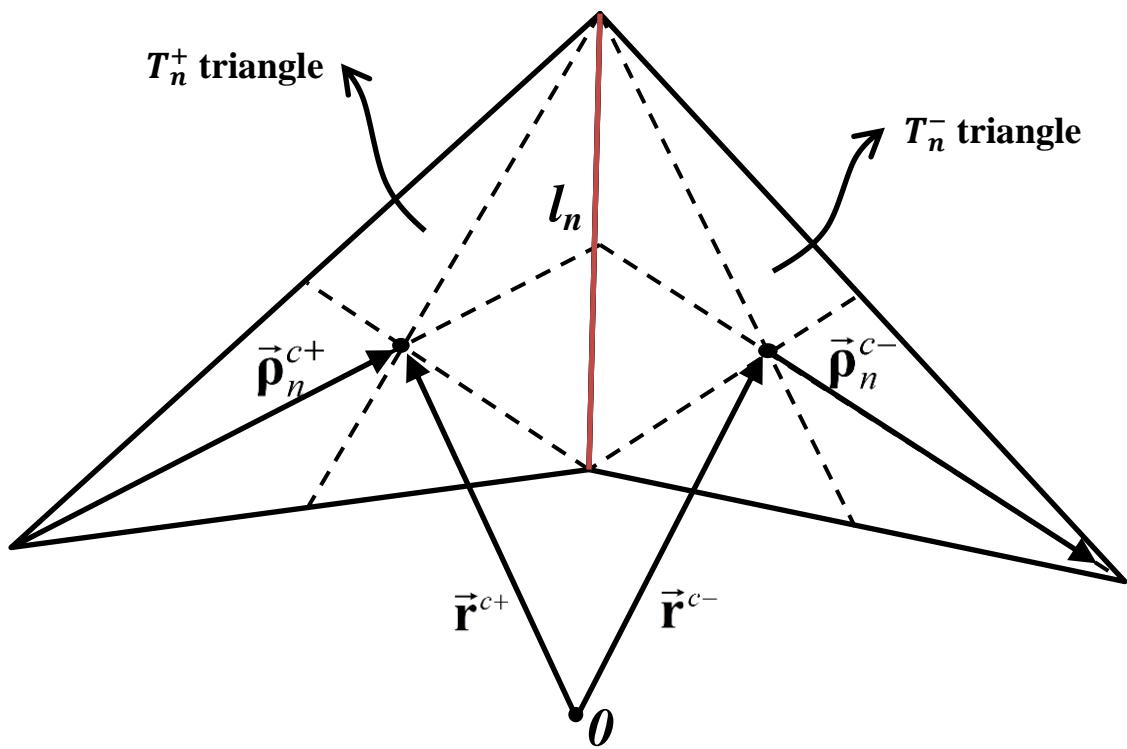


Fig. 2.10 Geometry of vectors to centroids of triangles associated with an edge.

RWG expansion functions of (2.58) are used for $\vec{\mathbf{M}}_{1n}$, $\vec{\mathbf{M}}_{2n}$ and $\vec{\mathbf{J}}_n$ in (2.36)–(2.38)

to approximate the unknown surface currents. Thus, $\vec{\mathbf{M}}_{1n} = \vec{\mathbf{f}}_{1n}$, $\vec{\mathbf{M}}_{2n} = \vec{\mathbf{f}}_{2n}$, and $\vec{\mathbf{J}}_n = \vec{\mathbf{f}}_n$

where $\vec{\mathbf{f}}_{1n}$, $\vec{\mathbf{f}}_{2n}$, and $\vec{\mathbf{f}}_n$ are RWG expansion functions. Since RWG expansion functions

are generated only for non-boundary edges, each of the N_a expansion functions for $\vec{\mathbf{M}}_1$

is confined to the top aperture and each of the N_c expansion functions for $\vec{\mathbf{M}}_2$ is confined to the bottom aperture. There aren't any boundary edges for the closed cavity, so an expansion function is associated with every edge of the triangles in the patched model of the cavity.

For testing procedure, the expansion functions are used as testing functions. This is so-called *Galerkin's method*. Then $\vec{\mathbf{W}}_{1m}$, $\vec{\mathbf{W}}_{2m}$, and $\vec{\mathbf{T}}_m$ in (2.45)–(2.47) become $\vec{\mathbf{f}}_{1m}$, $\vec{\mathbf{f}}_{2m}$, and $\vec{\mathbf{f}}_m$ respectively. The symmetric products are defined for the top aperture, the bottom aperture, and the closed cavity surface in (2.42)–(2.44).

2.4 Evaluation of the Elements of the Matrices

The elements of the matrices in (2.48)–(2.57) will be expressed in detail using the expansion and testing procedures of the previous section.

The excitation matrix in (2.48) has the following N_a non-zero elements:

$$2\langle \vec{\mathbf{W}}_{1m}, \vec{\mathbf{H}}_{\text{tan}}^{\text{inc}} \rangle_{\text{top}} = 2\langle \vec{\mathbf{f}}_{1m}, \vec{\mathbf{H}}_{\text{tan}}^{\text{inc}} \rangle_{\text{top}} = 2\iint_{\text{top}} \vec{\mathbf{f}}_{1m} \cdot \vec{\mathbf{H}}^{\text{inc}} ds. \quad (2.61)$$

The subscript “tan” is dropped for the integration in (2.61) because $\vec{\mathbf{f}}_{1m}$ doesn't have any components normal to the surface. The surface integral in (2.61) can be approximated by taking the value of $\vec{\mathbf{H}}^{\text{inc}}$ on any triangle on the top aperture to be constant and equal to $\vec{\mathbf{H}}^{\text{inc}}(\vec{\mathbf{r}}_{1m}^{c\pm})$, where $\vec{\mathbf{r}}_{1m}^{c\pm}$ is the vector from 0 to the centroid of T_{1m}^{\pm} . This will eliminate calculating double surface integrals and the value of the integral in (2.61) can be found by using the property in (2.60) as

$$\begin{aligned}
2 \iint_{\text{top}} \vec{\mathbf{f}}_{1m} \cdot \vec{\mathbf{H}}^{\text{inc}} ds &\cong 2 \left(\vec{\mathbf{H}}^{\text{inc}}(\vec{\mathbf{r}}_{1m}^{c+}) \cdot \iint_{T_{1m}^+} \vec{\mathbf{f}}_{1m} ds + \vec{\mathbf{H}}^{\text{inc}}(\vec{\mathbf{r}}_{1m}^{c-}) \cdot \iint_{T_{1m}^-} \vec{\mathbf{f}}_{1m} ds \right) \\
&= 2 \left(\vec{\mathbf{H}}^{\text{inc}}(\vec{\mathbf{r}}_{1m}^{c+}) \cdot \frac{l_{1m}}{2} \vec{\boldsymbol{\rho}}_{1m}^{c+} + \vec{\mathbf{H}}^{\text{inc}}(\vec{\mathbf{r}}_{1m}^{c-}) \cdot \frac{l_{1m}}{2} \vec{\boldsymbol{\rho}}_{1m}^{c-} \right) \\
&= l_{1m} \left(\vec{\mathbf{H}}^{\text{inc}}(\vec{\mathbf{r}}_{1m}^{c+}) \cdot \vec{\boldsymbol{\rho}}_{1m}^{c+} + \vec{\mathbf{H}}^{\text{inc}}(\vec{\mathbf{r}}_{1m}^{c-}) \cdot \vec{\boldsymbol{\rho}}_{1m}^{c-} \right). \tag{2.62}
\end{aligned}$$

The excitation is a plane wave incident on the top aperture in region a and it is set as

$$\vec{\mathbf{H}}^{\text{inc}}(\vec{\mathbf{r}}) = (\vec{\boldsymbol{\theta}}^{\text{inc}} H_{\theta} + \vec{\boldsymbol{\phi}}^{\text{inc}} H_{\phi}) e^{-j\vec{\mathbf{k}}^{\text{inc}} \cdot \vec{\mathbf{r}}}, \tag{2.63}$$

where $\vec{\boldsymbol{\theta}}^{\text{inc}}$ and $\vec{\boldsymbol{\phi}}^{\text{inc}}$ are spherical unit vectors associated with the incidence angles $(\theta^{\text{inc}}, \phi^{\text{inc}})$ and $\vec{\mathbf{k}}^{\text{inc}}$ is the propagation vector given by

$$\vec{\mathbf{k}}^{\text{inc}} = -\vec{\mathbf{r}}^{\text{inc}} k_a = -k_a (\sin \theta^{\text{inc}} \cos \phi^{\text{inc}} \vec{\mathbf{x}} + \sin \theta^{\text{inc}} \sin \phi^{\text{inc}} \vec{\mathbf{y}} + \cos \theta^{\text{inc}} \vec{\mathbf{z}}), \tag{2.64}$$

where k_a is the wavenumber for region a and is calculated by

$$k_a = \omega \sqrt{\epsilon_a \mu_a}. \tag{2.65}$$

The elements of the moment matrix in a brief form are given in (2.49)–(2.57). To evaluate these elements, again, the expansion and testing procedures from the previous section are used. The fields are discretized by substituting (2.36)–(2.38) for the unknown surface currents, and then the fields are tested using Galerkin's method with the symmetric products defined in (2.42)–(2.44). All testing and expansion functions are taken to be RWG functions in (2.58).

Each element of the moment matrix in (2.49)–(2.57) is either a symmetric product or a linear combination of symmetric products of the testing functions with the electric or magnetic fields due to one of the discretized surface current sources. So, these elements can be expressed easily if the general symmetric products are written.

First, the fields in (2.1)–(2.2) are separated into fields due to electric and magnetic sources:

$$\vec{\mathbf{E}}(\vec{\mathbf{J}}) = -j\omega\vec{\mathbf{A}} - \nabla V \quad (2.66)$$

$$\vec{\mathbf{E}}(\vec{\mathbf{M}}) = -\nabla \times \frac{\vec{\mathbf{F}}}{\varepsilon} \quad (2.67)$$

$$\vec{\mathbf{H}}(\vec{\mathbf{J}}) = \nabla \times \frac{\vec{\mathbf{A}}}{\mu} \quad (2.68)$$

$$\vec{\mathbf{H}}(\vec{\mathbf{M}}) = -j\omega\vec{\mathbf{F}} - \nabla U. \quad (2.69)$$

Then, these fields in (2.66)–(2.69) are tested with $\vec{\mathbf{f}}_m$ over S :

$$\begin{aligned} \langle \vec{\mathbf{f}}_m, \vec{\mathbf{E}}(\vec{\mathbf{J}}) \rangle_S &= \iint_S \vec{\mathbf{f}}_m \cdot \vec{\mathbf{E}}(\vec{\mathbf{J}}) \, ds = \iint_S \vec{\mathbf{f}}_m \cdot (-j\omega\vec{\mathbf{A}} - \nabla V) \, ds \\ &= -j\omega \iint_S \vec{\mathbf{f}}_m \cdot \vec{\mathbf{A}} \, ds - \iint_S \vec{\mathbf{f}}_m \cdot \nabla V \, ds \end{aligned} \quad (2.70)$$

$$\langle \vec{\mathbf{f}}_m, \vec{\mathbf{E}}(\vec{\mathbf{M}}) \rangle_S = \iint_S \vec{\mathbf{f}}_m \cdot \vec{\mathbf{E}}(\vec{\mathbf{M}}) \, ds = \iint_S \vec{\mathbf{f}}_m \cdot \left(-\nabla \times \frac{\vec{\mathbf{F}}}{\varepsilon} \right) \, ds \quad (2.71)$$

$$\langle \vec{\mathbf{f}}_m, \vec{\mathbf{H}}(\vec{\mathbf{J}}) \rangle_S = \iint_S \vec{\mathbf{f}}_m \cdot \vec{\mathbf{H}}(\vec{\mathbf{J}}) \, ds = \iint_S \vec{\mathbf{f}}_m \cdot \left(\nabla \times \frac{\vec{\mathbf{A}}}{\mu} \right) \, ds \quad (2.72)$$

$$\begin{aligned} \langle \vec{\mathbf{f}}_m, \vec{\mathbf{H}}(\vec{\mathbf{M}}) \rangle_S &= \iint_S \vec{\mathbf{f}}_m \cdot \vec{\mathbf{H}}(\vec{\mathbf{M}}) \, ds = \iint_S \vec{\mathbf{f}}_m \cdot (-j\omega\vec{\mathbf{F}} - \nabla U) \, ds \\ &= -j\omega \iint_S \vec{\mathbf{f}}_m \cdot \vec{\mathbf{F}} \, ds - \iint_S \vec{\mathbf{f}}_m \cdot \nabla U \, ds. \end{aligned} \quad (2.73)$$

The last terms in (2.70) and (2.73) can be written as

$$\iint_S \vec{\mathbf{f}}_m \cdot \nabla V \, ds = -\iint_S V(\nabla \cdot \vec{\mathbf{f}}_m) \, ds, \quad (2.74)$$

$$\iint_S \vec{\mathbf{f}}_m \cdot \nabla U \, ds = -\iint_S U(\nabla \cdot \vec{\mathbf{f}}_m) \, ds \quad (2.75)$$

using the following vector identity for divergence operation [45]

$$\nabla \cdot (\phi \vec{\mathbf{A}}) = \phi (\nabla \cdot \vec{\mathbf{A}}) + \vec{\mathbf{A}} \cdot (\nabla \phi), \quad (2.76)$$

where ϕ is a scalar function, in conjunction with the Gauss theorem and considering that $\vec{\mathbf{f}}_m$ doesn't have a component perpendicular to the surface boundary.

The surface integrals over S in (2.70)–(2.73) can be approximated by taking the values of the potentials on any triangle to be constant and equal to their values at the centroid of that triangle. The integrals are written as a sum of integrals over T_m^+ and T_m^- , and (2.74)–(2.75) are used in (2.70) and (2.73):

$$\begin{aligned} \langle \vec{\mathbf{f}}_m, \vec{\mathbf{E}}(\vec{\mathbf{J}}) \rangle_S &= -j\omega \left(\vec{\mathbf{A}}(\vec{\mathbf{r}}_m^{c+}) \cdot \iint_{T_m^+} \vec{\mathbf{f}}_m \, ds + \vec{\mathbf{A}}(\vec{\mathbf{r}}_m^{c-}) \cdot \iint_{T_m^-} \vec{\mathbf{f}}_m \, ds \right) \\ &\quad + V(\vec{\mathbf{r}}_m^{c+}) \iint_{T_m^+} \nabla \cdot \vec{\mathbf{f}}_m \, ds + V(\vec{\mathbf{r}}_m^{c-}) \iint_{T_m^-} \nabla \cdot \vec{\mathbf{f}}_m \, ds \end{aligned} \quad (2.77)$$

$$\langle \vec{\mathbf{f}}_m, \vec{\mathbf{E}}(\vec{\mathbf{M}}) \rangle_S = - \left(\nabla \times \frac{\vec{\mathbf{F}}(\vec{\mathbf{r}}_m^{c+})}{\varepsilon} \cdot \iint_{T_m^+} \vec{\mathbf{f}}_m \, ds + \nabla \times \frac{\vec{\mathbf{F}}(\vec{\mathbf{r}}_m^{c-})}{\varepsilon} \cdot \iint_{T_m^-} \vec{\mathbf{f}}_m \, ds \right) \quad (2.78)$$

$$\langle \vec{\mathbf{f}}_m, \vec{\mathbf{H}}(\vec{\mathbf{J}}) \rangle_S = \nabla \times \frac{\vec{\mathbf{A}}(\vec{\mathbf{r}}_m^{c+})}{\mu} \cdot \iint_{T_m^+} \vec{\mathbf{f}}_m \, ds + \nabla \times \frac{\vec{\mathbf{A}}(\vec{\mathbf{r}}_m^{c-})}{\mu} \cdot \iint_{T_m^-} \vec{\mathbf{f}}_m \, ds \quad (2.79)$$

$$\begin{aligned} \langle \vec{\mathbf{f}}_m, \vec{\mathbf{H}}(\vec{\mathbf{M}}) \rangle_S &= -j\omega \left(\vec{\mathbf{F}}(\vec{\mathbf{r}}_m^{c+}) \cdot \iint_{T_m^+} \vec{\mathbf{f}}_m \, ds + \vec{\mathbf{F}}(\vec{\mathbf{r}}_m^{c-}) \cdot \iint_{T_m^-} \vec{\mathbf{f}}_m \, ds \right) \\ &\quad + U(\vec{\mathbf{r}}_m^{c+}) \iint_{T_m^+} \nabla \cdot \vec{\mathbf{f}}_m \, ds + U(\vec{\mathbf{r}}_m^{c-}) \iint_{T_m^-} \nabla \cdot \vec{\mathbf{f}}_m \, ds. \end{aligned} \quad (2.80)$$

The integrals over the triangles in (2.77)–(2.80) can be calculated now using the properties of RWG functions in (2.59) and (2.60):

$$\langle \vec{\mathbf{f}}_m, \vec{\mathbf{E}}(\vec{\mathbf{J}}) \rangle_S = -j\omega \frac{l_m}{2} \left(\vec{\mathbf{A}}(\vec{\mathbf{r}}_m^{c+}) \cdot \vec{\mathbf{p}}_m^{c+} + \vec{\mathbf{A}}(\vec{\mathbf{r}}_m^{c-}) \cdot \vec{\mathbf{p}}_m^{c-} \right) + l_m \left(V(\vec{\mathbf{r}}_m^{c+}) - V(\vec{\mathbf{r}}_m^{c-}) \right) \quad (2.81)$$

$$\langle \vec{\mathbf{f}}_m, \vec{\mathbf{E}}(\vec{\mathbf{M}}) \rangle_S = -\frac{l_m}{2} \left(\nabla \times \frac{\vec{\mathbf{F}}(\vec{\mathbf{r}}_m^{c+})}{\varepsilon} \cdot \vec{\rho}_m^{c+} + \nabla \times \frac{\vec{\mathbf{F}}(\vec{\mathbf{r}}_m^{c-})}{\varepsilon} \cdot \vec{\rho}_m^{c-} \right) \quad (2.82)$$

$$\langle \vec{\mathbf{f}}_m, \vec{\mathbf{H}}(\vec{\mathbf{J}}) \rangle_S = \frac{l_m}{2} \left(\nabla \times \frac{\vec{\mathbf{A}}(\vec{\mathbf{r}}_m^{c+})}{\mu} \cdot \vec{\rho}_m^{c+} + \nabla \times \frac{\vec{\mathbf{A}}(\vec{\mathbf{r}}_m^{c-})}{\mu} \cdot \vec{\rho}_m^{c-} \right) \quad (2.83)$$

$$\langle \vec{\mathbf{f}}_m, \vec{\mathbf{H}}(\vec{\mathbf{M}}) \rangle_S = -j\omega \frac{l_m}{2} \left(\vec{\mathbf{F}}(\vec{\mathbf{r}}_m^{c+}) \cdot \vec{\rho}_m^{c+} + \vec{\mathbf{F}}(\vec{\mathbf{r}}_m^{c-}) \cdot \vec{\rho}_m^{c-} \right) + l_m \left(U(\vec{\mathbf{r}}_m^{c+}) - U(\vec{\mathbf{r}}_m^{c-}) \right). \quad (2.84)$$

The potentials in (2.81)–(2.84) are replaced with their expressions given in (2.3)–(2.6), and $\vec{\mathbf{J}}$ and $\vec{\mathbf{M}}$ in these expressions are replaced with $\vec{\mathbf{J}}_n$ and $\vec{\mathbf{M}}_n$. The integration is over S where $\vec{\mathbf{J}}_n$ and $\vec{\mathbf{M}}_n$ exist:

$$\begin{aligned} \langle \vec{\mathbf{f}}_m, \vec{\mathbf{E}}(\vec{\mathbf{J}}_n) \rangle_S &= -j\omega \frac{l_m \mu}{8\pi} \left(\vec{\rho}_m^{c+} \cdot \iint_S \vec{\mathbf{J}}_n(\vec{\mathbf{r}}') G(\vec{\mathbf{r}}_m^{c+}, \vec{\mathbf{r}}') ds' + \vec{\rho}_m^{c-} \cdot \iint_S \vec{\mathbf{J}}_n(\vec{\mathbf{r}}') G(\vec{\mathbf{r}}_m^{c-}, \vec{\mathbf{r}}') ds' \right) \\ &\quad + j \frac{l_m}{4\pi \varepsilon \omega} \left(\iint_S \nabla' \cdot \vec{\mathbf{J}}_n(\vec{\mathbf{r}}') G(\vec{\mathbf{r}}_m^{c+}, \vec{\mathbf{r}}') ds' - \iint_S \nabla' \cdot \vec{\mathbf{J}}_n(\vec{\mathbf{r}}') G(\vec{\mathbf{r}}_m^{c-}, \vec{\mathbf{r}}') ds' \right) \end{aligned} \quad (2.85)$$

$$\begin{aligned} \langle \vec{\mathbf{f}}_m, \vec{\mathbf{E}}(\vec{\mathbf{M}}_n) \rangle_S &= -\frac{l_m}{8\pi} \left(\vec{\rho}_m^{c+} \cdot \iint_S \vec{\mathbf{M}}_n(\vec{\mathbf{r}}') \times (\vec{\mathbf{r}}_m^{c+} - \vec{\mathbf{r}}') \frac{1 + jk |\vec{\mathbf{r}}_m^{c+} - \vec{\mathbf{r}}'|}{|\vec{\mathbf{r}}_m^{c+} - \vec{\mathbf{r}}'|^2} G(\vec{\mathbf{r}}_m^{c+}, \vec{\mathbf{r}}') ds' \right. \\ &\quad \left. + \vec{\rho}_m^{c-} \cdot \iint_S \vec{\mathbf{M}}_n(\vec{\mathbf{r}}') \times (\vec{\mathbf{r}}_m^{c-} - \vec{\mathbf{r}}') \frac{1 + jk |\vec{\mathbf{r}}_m^{c-} - \vec{\mathbf{r}}'|}{|\vec{\mathbf{r}}_m^{c-} - \vec{\mathbf{r}}'|^2} G(\vec{\mathbf{r}}_m^{c-}, \vec{\mathbf{r}}') ds' \right) \\ &\quad - \frac{l_m}{2} \left[\vec{\rho}_m^{c+} \cdot \left(\frac{\vec{\mathbf{M}}_n(\vec{\mathbf{r}}_m^{c+})}{2} \times \vec{\mathbf{n}} \right) + \vec{\rho}_m^{c-} \cdot \left(\frac{\vec{\mathbf{M}}_n(\vec{\mathbf{r}}_m^{c-})}{2} \times \vec{\mathbf{n}} \right) \right] \end{aligned} \quad (2.86)$$

$$\langle \vec{\mathbf{f}}_m, \vec{\mathbf{H}}(\vec{\mathbf{J}}_n) \rangle_S = \frac{l_m}{8\pi} \left(\vec{\rho}_m^{c+} \cdot \iint_S \vec{\mathbf{J}}_n(\vec{\mathbf{r}}') \times (\vec{\mathbf{r}}_m^{c+} - \vec{\mathbf{r}}') \frac{1 + jk |\vec{\mathbf{r}}_m^{c+} - \vec{\mathbf{r}}'|}{|\vec{\mathbf{r}}_m^{c+} - \vec{\mathbf{r}}'|^2} G(\vec{\mathbf{r}}_m^{c+}, \vec{\mathbf{r}}') ds' \right)$$

$$\begin{aligned}
& + \bar{\rho}_m^{c-} \cdot \iint_S \bar{\mathbf{J}}_n(\bar{\mathbf{r}}') \times (\bar{\mathbf{r}}_m^{c-} - \bar{\mathbf{r}}') \frac{1 + jk |\bar{\mathbf{r}}_m^{c-} - \bar{\mathbf{r}}'|}{|\bar{\mathbf{r}}_m^{c-} - \bar{\mathbf{r}}'|^2} G(\bar{\mathbf{r}}_m^{c-}, \bar{\mathbf{r}}') ds' \Big) \\
& + \frac{l_m}{2} \left[\bar{\rho}_m^{c+} \cdot \left(\frac{\bar{\mathbf{J}}_n(\bar{\mathbf{r}}_m^{c+})}{2} \times \bar{\mathbf{n}} \right) + \bar{\rho}_m^{c-} \cdot \left(\frac{\bar{\mathbf{J}}_n(\bar{\mathbf{r}}_m^{c-})}{2} \times \bar{\mathbf{n}} \right) \right] \quad (2.87)
\end{aligned}$$

$$\begin{aligned}
\langle \bar{\mathbf{f}}_m, \bar{\mathbf{H}}(\bar{\mathbf{M}}_n) \rangle_S & = -j\omega \frac{l_m \mathcal{E}}{8\pi} \left(\bar{\rho}_m^{c+} \cdot \iint_S \bar{\mathbf{M}}_n(\bar{\mathbf{r}}') G(\bar{\mathbf{r}}_m^{c+}, \bar{\mathbf{r}}') ds' + \bar{\rho}_m^{c-} \cdot \iint_S \bar{\mathbf{M}}_n(\bar{\mathbf{r}}') G(\bar{\mathbf{r}}_m^{c-}, \bar{\mathbf{r}}') ds' \right) \\
& + j \frac{l_m}{4\pi\mu\omega} \left(\iint_S \nabla' \cdot \bar{\mathbf{M}}_n(\bar{\mathbf{r}}') G(\bar{\mathbf{r}}_m^{c+}, \bar{\mathbf{r}}') ds' - \iint_S \nabla' \cdot \bar{\mathbf{M}}_n(\bar{\mathbf{r}}') G(\bar{\mathbf{r}}_m^{c-}, \bar{\mathbf{r}}') ds' \right), \quad (2.88)
\end{aligned}$$

where $\bar{\mathbf{n}}$ is the unit normal vector pointing from the source surface into the region where the fields are to be calculated. The derivation of (2.86) and (2.87) can be found in [46, pp. 155-159]. Briefly, the tangential components of $\bar{\mathbf{E}}(\bar{\mathbf{M}})$ and $\bar{\mathbf{H}}(\bar{\mathbf{J}})$ are discontinuous on the current surface, so the fields jump out while traversing the surface. The expressions for this can be written as

$$\begin{aligned}
\bar{\mathbf{E}}(\bar{\mathbf{M}}) & = -\nabla \times \frac{\bar{\mathbf{F}}}{\varepsilon} = - \left(\frac{1}{4\pi} \iint \bar{\mathbf{M}}(\bar{\mathbf{r}}') \times \nabla' G(\bar{\mathbf{r}}, \bar{\mathbf{r}}') ds' + \frac{\bar{\mathbf{M}}(\bar{\mathbf{r}})}{2} \times \bar{\mathbf{n}} \right) \\
& = - \left(\frac{1}{4\pi} \iint \bar{\mathbf{M}}(\bar{\mathbf{r}}') \times (\bar{\mathbf{r}} - \bar{\mathbf{r}}') \frac{1 + jk |\bar{\mathbf{r}} - \bar{\mathbf{r}}'|}{|\bar{\mathbf{r}} - \bar{\mathbf{r}}'|^2} G(\bar{\mathbf{r}}, \bar{\mathbf{r}}') ds' + \frac{\bar{\mathbf{M}}(\bar{\mathbf{r}})}{2} \times \bar{\mathbf{n}} \right) \quad (2.89)
\end{aligned}$$

$$\begin{aligned}
\bar{\mathbf{H}}(\bar{\mathbf{J}}) & = \nabla \times \frac{\bar{\mathbf{A}}}{\mu} = \frac{1}{4\pi} \iint \bar{\mathbf{J}}(\bar{\mathbf{r}}') \times \nabla' G(\bar{\mathbf{r}}, \bar{\mathbf{r}}') ds' + \frac{\bar{\mathbf{J}}(\bar{\mathbf{r}})}{2} \times \bar{\mathbf{n}} \\
& = \frac{1}{4\pi} \iint \bar{\mathbf{J}}(\bar{\mathbf{r}}') \times (\bar{\mathbf{r}} - \bar{\mathbf{r}}') \frac{1 + jk |\bar{\mathbf{r}} - \bar{\mathbf{r}}'|}{|\bar{\mathbf{r}} - \bar{\mathbf{r}}'|^2} G(\bar{\mathbf{r}}, \bar{\mathbf{r}}') ds' + \frac{\bar{\mathbf{J}}(\bar{\mathbf{r}})}{2} \times \bar{\mathbf{n}} \quad (2.90)
\end{aligned}$$

for field evaluation on the side of S facing the region into which $\bar{\mathbf{n}}$ points. In the limit as the location where the field is evaluated approaches the source surface from one side of the source surface, each integral in (2.89)–(2.90) becomes a principal value integral in

which an infinitesimal source region which includes the field point is deleted. However, the source region that was deleted cannot be overlooked because, if it was not deleted, it would produce the field that jumps out.

Finally, the general symmetric products are obtained by replacing $\vec{\mathbf{J}}_n$ and $\vec{\mathbf{M}}_n$ in (2.85)–(2.88) with (2.58) since both are equal to $\vec{\mathbf{f}}_n$, replacing $\nabla' \cdot \vec{\mathbf{J}}_n(\vec{\mathbf{r}}')$ in (2.85) and $\nabla' \cdot \vec{\mathbf{M}}_n(\vec{\mathbf{r}}')$ in (2.88) with (2.59), and writing the integrals over S as a summation of integrals over T_n^+ and T_n^- triangles:

$$\begin{aligned} \langle \vec{\mathbf{f}}_m, \vec{\mathbf{E}}(\vec{\mathbf{J}}_n) \rangle_S &= -j\omega \frac{l_m l_n \mu}{16\pi} \left[\vec{\mathbf{p}}_m^{c+} \cdot \left(\frac{1}{A_n^+} \iint_{T_n^+} \vec{\mathbf{p}}_n^+ G(\vec{\mathbf{r}}_m^{c+}, \vec{\mathbf{r}}') ds' + \frac{1}{A_n^-} \iint_{T_n^-} \vec{\mathbf{p}}_n^- G(\vec{\mathbf{r}}_m^{c+}, \vec{\mathbf{r}}') ds' \right) \right. \\ &\quad \left. + \vec{\mathbf{p}}_m^{c-} \cdot \left(\frac{1}{A_n^+} \iint_{T_n^+} \vec{\mathbf{p}}_n^+ G(\vec{\mathbf{r}}_m^{c-}, \vec{\mathbf{r}}') ds' + \frac{1}{A_n^-} \iint_{T_n^-} \vec{\mathbf{p}}_n^- G(\vec{\mathbf{r}}_m^{c-}, \vec{\mathbf{r}}') ds' \right) \right] \\ &\quad + j \frac{l_m l_n}{4\pi\epsilon\omega} \left(\frac{1}{A_n^+} \iint_{T_n^+} G(\vec{\mathbf{r}}_m^{c+}, \vec{\mathbf{r}}') ds' - \frac{1}{A_n^-} \iint_{T_n^-} G(\vec{\mathbf{r}}_m^{c+}, \vec{\mathbf{r}}') ds' \right. \\ &\quad \left. - \frac{1}{A_n^+} \iint_{T_n^+} G(\vec{\mathbf{r}}_m^{c-}, \vec{\mathbf{r}}') ds' + \frac{1}{A_n^-} \iint_{T_n^-} G(\vec{\mathbf{r}}_m^{c-}, \vec{\mathbf{r}}') ds' \right) \end{aligned} \quad (2.91)$$

$$\begin{aligned} \langle \vec{\mathbf{f}}_m, \vec{\mathbf{E}}(\vec{\mathbf{M}}_n) \rangle_S &= -\frac{l_m l_n}{16\pi} \left[\vec{\mathbf{p}}_m^{c+} \cdot \left(\frac{1}{A_n^+} \iint_{T_n^+} \vec{\mathbf{p}}_n^+ \times (\vec{\mathbf{r}}_m^{c+} - \vec{\mathbf{r}}') \frac{1 + jk |\vec{\mathbf{r}}_m^{c+} - \vec{\mathbf{r}}'|}{|\vec{\mathbf{r}}_m^{c+} - \vec{\mathbf{r}}'|^2} G(\vec{\mathbf{r}}_m^{c+}, \vec{\mathbf{r}}') ds' \right. \right. \\ &\quad \left. \left. + \frac{1}{A_n^-} \iint_{T_n^-} \vec{\mathbf{p}}_n^- \times (\vec{\mathbf{r}}_m^{c+} - \vec{\mathbf{r}}') \frac{1 + jk |\vec{\mathbf{r}}_m^{c+} - \vec{\mathbf{r}}'|}{|\vec{\mathbf{r}}_m^{c+} - \vec{\mathbf{r}}'|^2} G(\vec{\mathbf{r}}_m^{c+}, \vec{\mathbf{r}}') ds' \right) \right. \\ &\quad \left. + \vec{\mathbf{p}}_m^{c-} \cdot \left(\frac{1}{A_n^+} \iint_{T_n^+} \vec{\mathbf{p}}_n^+ \times (\vec{\mathbf{r}}_m^{c-} - \vec{\mathbf{r}}') \frac{1 + jk |\vec{\mathbf{r}}_m^{c-} - \vec{\mathbf{r}}'|}{|\vec{\mathbf{r}}_m^{c-} - \vec{\mathbf{r}}'|^2} G(\vec{\mathbf{r}}_m^{c-}, \vec{\mathbf{r}}') ds' \right. \right. \\ &\quad \left. \left. + \frac{1}{A_n^-} \iint_{T_n^-} \vec{\mathbf{p}}_n^- \times (\vec{\mathbf{r}}_m^{c-} - \vec{\mathbf{r}}') \frac{1 + jk |\vec{\mathbf{r}}_m^{c-} - \vec{\mathbf{r}}'|}{|\vec{\mathbf{r}}_m^{c-} - \vec{\mathbf{r}}'|^2} G(\vec{\mathbf{r}}_m^{c-}, \vec{\mathbf{r}}') ds' \right) \right] \end{aligned}$$

$$\begin{aligned}
& \left. + \frac{1}{A_n^-} \iint_{T_n^-} \bar{\boldsymbol{\rho}}_n^- \times (\bar{\mathbf{r}}_m^{c-} - \bar{\mathbf{r}}') \frac{1 + jk |\bar{\mathbf{r}}_m^{c-} - \bar{\mathbf{r}}'|}{|\bar{\mathbf{r}}_m^{c-} - \bar{\mathbf{r}}'|^2} G(\bar{\mathbf{r}}_m^{c-}, \bar{\mathbf{r}}') ds' \right] \\
& - \frac{l_m l_n}{8} \frac{1}{A_n^\pm} \bar{\boldsymbol{\rho}}_m^{c+} \cdot \left(\begin{pmatrix} \bar{\boldsymbol{\rho}}_n^\pm(\bar{\mathbf{r}}_m^{c+}), & \bar{\mathbf{r}}_m^{c+} \text{ in } T_n^\pm \\ 0, & \bar{\mathbf{r}}_m^{c+} \text{ not in } T_n^\pm \end{pmatrix} \times \bar{\mathbf{n}} \right) \\
& - \frac{l_m l_n}{8} \frac{1}{A_n^\pm} \bar{\boldsymbol{\rho}}_m^{c-} \cdot \left(\begin{pmatrix} \bar{\boldsymbol{\rho}}_n^\pm(\bar{\mathbf{r}}_m^{c-}), & \bar{\mathbf{r}}_m^{c-} \text{ in } T_n^\pm \\ 0, & \bar{\mathbf{r}}_m^{c-} \text{ not in } T_n^\pm \end{pmatrix} \times \bar{\mathbf{n}} \right) \tag{2.92}
\end{aligned}$$

$$\begin{aligned}
\langle \bar{\mathbf{f}}_m, \bar{\mathbf{H}}(\bar{\mathbf{J}}_n) \rangle_S &= \frac{l_m l_n}{16\pi} \left[\bar{\boldsymbol{\rho}}_m^{c+} \cdot \left(\frac{1}{A_n^+} \iint_{T_n^+} \bar{\boldsymbol{\rho}}_n^+ \times (\bar{\mathbf{r}}_m^{c+} - \bar{\mathbf{r}}') \frac{1 + jk |\bar{\mathbf{r}}_m^{c+} - \bar{\mathbf{r}}'|}{|\bar{\mathbf{r}}_m^{c+} - \bar{\mathbf{r}}'|^2} G(\bar{\mathbf{r}}_m^{c+}, \bar{\mathbf{r}}') ds' \right. \right. \\
& \quad \left. \left. + \frac{1}{A_n^-} \iint_{T_n^-} \bar{\boldsymbol{\rho}}_n^- \times (\bar{\mathbf{r}}_m^{c+} - \bar{\mathbf{r}}') \frac{1 + jk |\bar{\mathbf{r}}_m^{c+} - \bar{\mathbf{r}}'|}{|\bar{\mathbf{r}}_m^{c+} - \bar{\mathbf{r}}'|^2} G(\bar{\mathbf{r}}_m^{c+}, \bar{\mathbf{r}}') ds' \right) \right. \\
& \quad \left. + \bar{\boldsymbol{\rho}}_m^{c-} \cdot \left(\frac{1}{A_n^+} \iint_{T_n^+} \bar{\boldsymbol{\rho}}_n^+ \times (\bar{\mathbf{r}}_m^{c-} - \bar{\mathbf{r}}') \frac{1 + jk |\bar{\mathbf{r}}_m^{c-} - \bar{\mathbf{r}}'|}{|\bar{\mathbf{r}}_m^{c-} - \bar{\mathbf{r}}'|^2} G(\bar{\mathbf{r}}_m^{c-}, \bar{\mathbf{r}}') ds' \right. \right. \\
& \quad \left. \left. + \frac{1}{A_n^-} \iint_{T_n^-} \bar{\boldsymbol{\rho}}_n^- \times (\bar{\mathbf{r}}_m^{c-} - \bar{\mathbf{r}}') \frac{1 + jk |\bar{\mathbf{r}}_m^{c-} - \bar{\mathbf{r}}'|}{|\bar{\mathbf{r}}_m^{c-} - \bar{\mathbf{r}}'|^2} G(\bar{\mathbf{r}}_m^{c-}, \bar{\mathbf{r}}') ds' \right) \right] \\
& \quad + \frac{l_m l_n}{8} \frac{1}{A_n^\pm} \bar{\boldsymbol{\rho}}_m^{c+} \cdot \left(\begin{pmatrix} \bar{\boldsymbol{\rho}}_n^\pm(\bar{\mathbf{r}}_m^{c+}), & \bar{\mathbf{r}}_m^{c+} \text{ in } T_n^\pm \\ 0, & \bar{\mathbf{r}}_m^{c+} \text{ not in } T_n^\pm \end{pmatrix} \times \bar{\mathbf{n}} \right) \\
& \quad + \frac{l_m l_n}{8} \frac{1}{A_n^\pm} \bar{\boldsymbol{\rho}}_m^{c-} \cdot \left(\begin{pmatrix} \bar{\boldsymbol{\rho}}_n^\pm(\bar{\mathbf{r}}_m^{c-}), & \bar{\mathbf{r}}_m^{c-} \text{ in } T_n^\pm \\ 0, & \bar{\mathbf{r}}_m^{c-} \text{ not in } T_n^\pm \end{pmatrix} \times \bar{\mathbf{n}} \right) \tag{2.93}
\end{aligned}$$

$$\langle \bar{\mathbf{f}}_m, \bar{\mathbf{H}}(\bar{\mathbf{M}}_n) \rangle_S = -j\omega \frac{l_m l_n \varepsilon}{16\pi} \left[\bar{\boldsymbol{\rho}}_m^{c+} \cdot \left(\frac{1}{A_n^+} \iint_{T_n^+} \bar{\boldsymbol{\rho}}_n^+ G(\bar{\mathbf{r}}_m^{c+}, \bar{\mathbf{r}}') ds' + \frac{1}{A_n^-} \iint_{T_n^-} \bar{\boldsymbol{\rho}}_n^- G(\bar{\mathbf{r}}_m^{c+}, \bar{\mathbf{r}}') ds' \right) \right]$$

$$\begin{aligned}
& + \bar{\mathbf{p}}_m^{c-} \cdot \left(\frac{1}{A_n^+} \iint_{T_n^+} \bar{\mathbf{p}}_n^+ G(\bar{\mathbf{r}}_m^{c-}, \bar{\mathbf{r}}') ds' + \frac{1}{A_n^-} \iint_{T_n^-} \bar{\mathbf{p}}_n^- G(\bar{\mathbf{r}}_m^{c-}, \bar{\mathbf{r}}') ds' \right) \Bigg] \\
& + j \frac{l_m l_n}{4\pi\mu\omega} \left(\frac{1}{A_n^+} \iint_{T_n^+} G(\bar{\mathbf{r}}_m^{c+}, \bar{\mathbf{r}}') ds' - \frac{1}{A_n^-} \iint_{T_n^-} G(\bar{\mathbf{r}}_m^{c+}, \bar{\mathbf{r}}') ds' \right. \\
& \quad \left. - \frac{1}{A_n^+} \iint_{T_n^+} G(\bar{\mathbf{r}}_m^{c-}, \bar{\mathbf{r}}') ds' + \frac{1}{A_n^-} \iint_{T_n^-} G(\bar{\mathbf{r}}_m^{c-}, \bar{\mathbf{r}}') ds' \right), \quad (2.94)
\end{aligned}$$

where the last two terms in each of (2.92) and (2.93) are to be interpreted as themselves with the choice of the upper sign plus themselves with the choice of the lower sign. For $m = n$, there is no jump-out term in (2.92) and (2.93). Given n and m , there could be only one jump-out term in (2.92). If present, it is one of the four possibilities obtained by letting the choice of the upper or lower sign in $(\bar{\mathbf{p}}_m^{c\pm}, T_m^\pm)$ be independent of the choice of the upper or lower sign in $(\bar{\mathbf{p}}_n^{c\pm}, T_n^\pm)$ in

$$-\frac{l_m l_n}{8} \frac{1}{A_n^\pm} \bar{\mathbf{p}}_m^{c\pm} \cdot (\bar{\mathbf{p}}_n^{c\pm} \times \bar{\mathbf{n}}) = -\frac{l_m l_n}{12} \text{sgn} \left[\bar{\mathbf{n}} \cdot (\bar{\mathbf{p}}_m^{c\pm} \times \bar{\mathbf{p}}_n^{c\pm}) \right], \quad T_m^\pm = T_n^\pm, \quad m \neq n \quad (2.95)$$

$\text{sgn}(x)$ in (2.95) is the sign function, which has a value of +1 for $x > 0$ and -1 for $x < 0$. The jump-out term in (2.95) was obtained by using the exact jump-out part of the electric field of the magnetic current $\bar{\mathbf{f}}_n$ in T_n^\pm [47, p. 15]. The jump-out term in (2.93) would be the negative of the quantity in (2.95).

The integrals in (2.92) and (2.93) are equal to 0 if the observation and source triangles are coplanar.

Each integral appearing in (2.91)–(2.94) is one of these three types:

$$\bar{\mathbf{I}}_{\rho\mathbf{G}mn} = \frac{1}{A_n} \iint_{T_n} \bar{\boldsymbol{\rho}}_n \frac{e^{-jk|\bar{\mathbf{r}}_m^c - \bar{\mathbf{r}}'|}}{|\bar{\mathbf{r}}_m^c - \bar{\mathbf{r}}'|} ds' \quad (2.96)$$

$$\mathbf{I}_{\mathbf{G}mn} = \frac{1}{A_n} \iint_{T_n} \frac{e^{-jk|\bar{\mathbf{r}}_m^c - \bar{\mathbf{r}}'|}}{|\bar{\mathbf{r}}_m^c - \bar{\mathbf{r}}'|} ds' \quad (2.97)$$

$$\bar{\mathbf{I}}_{\nabla\mathbf{G}mn} = \frac{1}{A_n} \iint_{T_n} \bar{\boldsymbol{\rho}}_n \times (\bar{\mathbf{r}}_m^c - \bar{\mathbf{r}}') \left(1 + jk|\bar{\mathbf{r}}_m^c - \bar{\mathbf{r}}'|\right) \frac{e^{-jk|\bar{\mathbf{r}}_m^c - \bar{\mathbf{r}}'|}}{|\bar{\mathbf{r}}_m^c - \bar{\mathbf{r}}'|^3} ds', \quad (2.98)$$

where Green's function in (2.91)–(2.94) is replaced with its expression using (2.7). $\bar{\mathbf{I}}_{\rho\mathbf{G}}$ and $\bar{\mathbf{I}}_{\nabla\mathbf{G}}$ are vector-valued integrals, whereas $\mathbf{I}_{\mathbf{G}}$ is a scalar-valued integral. These integrals will be calculated numerically using Gaussian quadrature rules developed for triangular domains [48]. However special care has to be taken evaluating the integrals in (2.96)–(2.98), since the integrands are singular. These integrals will be written in local coordinates, so-called area or barycentric coordinates, instead of global coordinates and then singularities are going to be extracted and calculated analytically using the scheme proposed by D. R. Wilton, et al. [49].

The elements of the moment matrix in (2.49)–(2.57) can be expressed by replacing the symmetric products with their expanded forms using the expressions found for the general symmetric products in (2.91)–(2.94) and by using (2.95) for the jump-out terms. However to give a concise expression, the integrals in (2.91)–(2.94) will be abbreviated as $\bar{\mathbf{I}}_{\rho\mathbf{G}}, \mathbf{I}_{\mathbf{G}}$ and $\bar{\mathbf{I}}_{\nabla\mathbf{G}}$, which are defined in (2.96)–(2.98):

$$\begin{aligned} [Y_{11mn}] = & \left[j\omega \frac{l_{1m}l_{1n}\epsilon_a}{8\pi} \left[\bar{\boldsymbol{\rho}}_{1m}^{c+} \cdot \left(\bar{\mathbf{I}}_{\rho\mathbf{G}1m1n}^{a++} + \bar{\mathbf{I}}_{\rho\mathbf{G}1m1n}^{a+-} \right) + \bar{\boldsymbol{\rho}}_{1m}^{c-} \cdot \left(\bar{\mathbf{I}}_{\rho\mathbf{G}1m1n}^{a-+} + \bar{\mathbf{I}}_{\rho\mathbf{G}1m1n}^{a--} \right) \right] \right. \\ & \left. - j \frac{l_{1m}l_{1n}}{2\pi\mu_a\omega} \left(\mathbf{I}_{\mathbf{G}1m1n}^{a++} - \mathbf{I}_{\mathbf{G}1m1n}^{a+-} - \mathbf{I}_{\mathbf{G}1m1n}^{a-+} + \mathbf{I}_{\mathbf{G}1m1n}^{a--} \right) \right] \end{aligned}$$

$$\begin{aligned}
& +j\omega \frac{l_1 l_n \varepsilon_b}{16\pi} \left[\tilde{\boldsymbol{\rho}}_{1m}^{c+} \cdot \left(\tilde{\mathbf{I}}_{\rho\mathbf{G}1m1n}^{b++} + \tilde{\mathbf{I}}_{\rho\mathbf{G}1m1n}^{b+-} \right) + \tilde{\boldsymbol{\rho}}_{1m}^{c-} \cdot \left(\tilde{\mathbf{I}}_{\rho\mathbf{G}1m1n}^{b-+} + \tilde{\mathbf{I}}_{\rho\mathbf{G}1m1n}^{b--} \right) \right] \\
& -j \frac{l_1 l_n}{4\pi\mu_b \omega} \left(\mathbf{I}_{\mathbf{G}1m1n}^{b++} - \mathbf{I}_{\mathbf{G}1m1n}^{b+-} - \mathbf{I}_{\mathbf{G}1m1n}^{b-+} + \mathbf{I}_{\mathbf{G}1m1n}^{b--} \right) \Big]_{N_a \times N_a} \quad (2.99)
\end{aligned}$$

$$\begin{aligned}
[Y_{12mn}] &= \left[j\omega \frac{l_1 l_n \varepsilon_b}{16\pi} \left[\tilde{\boldsymbol{\rho}}_{1m}^{c+} \cdot \left(\tilde{\mathbf{I}}_{\rho\mathbf{G}1m2n}^{b++} + \tilde{\mathbf{I}}_{\rho\mathbf{G}1m2n}^{b+-} \right) + \tilde{\boldsymbol{\rho}}_{1m}^{c-} \cdot \left(\tilde{\mathbf{I}}_{\rho\mathbf{G}1m2n}^{b-+} + \tilde{\mathbf{I}}_{\rho\mathbf{G}1m2n}^{b--} \right) \right] \right. \\
& \left. -j \frac{l_1 l_n}{4\pi\mu_b \omega} \left(\mathbf{I}_{\mathbf{G}1m2n}^{b++} - \mathbf{I}_{\mathbf{G}1m2n}^{b+-} - \mathbf{I}_{\mathbf{G}1m2n}^{b-+} + \mathbf{I}_{\mathbf{G}1m2n}^{b--} \right) \right]_{N_a \times N_c} \quad (2.100)
\end{aligned}$$

$$\begin{aligned}
[D_{13mn}] &= \left[\frac{l_1 l_n}{16\pi} \left[\tilde{\boldsymbol{\rho}}_{1m}^{c+} \cdot \left(\tilde{\mathbf{I}}_{\nabla\mathbf{G}1mn}^{b++} + \tilde{\mathbf{I}}_{\nabla\mathbf{G}1mn}^{b+-} \right) + \tilde{\boldsymbol{\rho}}_{1m}^{c-} \cdot \left(\tilde{\mathbf{I}}_{\nabla\mathbf{G}1mn}^{b-+} + \tilde{\mathbf{I}}_{\nabla\mathbf{G}1mn}^{b--} \right) \right] \right. \\
& \left. + \begin{cases} \frac{l_1 l_n}{12} \operatorname{sgn} \left[\tilde{\mathbf{n}} \cdot \left(\tilde{\boldsymbol{\rho}}_{1m}^{c\pm} \times \tilde{\boldsymbol{\rho}}_n^{c\pm} \right) \right], T_{1m}^{\pm} = T_n^{\pm}, m \neq n \\ 0, & \text{otherwise.} \end{cases} \right]_{N_a \times N_b} \quad (2.101)
\end{aligned}$$

$$\begin{aligned}
[Y_{21mn}] &= \left[j\omega \frac{l_2 l_n \varepsilon_b}{16\pi} \left[\tilde{\boldsymbol{\rho}}_{2m}^{c+} \cdot \left(\tilde{\mathbf{I}}_{\rho\mathbf{G}2m1n}^{b++} + \tilde{\mathbf{I}}_{\rho\mathbf{G}2m1n}^{b+-} \right) + \tilde{\boldsymbol{\rho}}_{2m}^{c-} \cdot \left(\tilde{\mathbf{I}}_{\rho\mathbf{G}2m1n}^{b-+} + \tilde{\mathbf{I}}_{\rho\mathbf{G}2m1n}^{b--} \right) \right] \right. \\
& \left. -j \frac{l_2 l_n}{4\pi\mu_b \omega} \left(\mathbf{I}_{\mathbf{G}2m1n}^{b++} - \mathbf{I}_{\mathbf{G}2m1n}^{b+-} - \mathbf{I}_{\mathbf{G}2m1n}^{b-+} + \mathbf{I}_{\mathbf{G}2m1n}^{b--} \right) \right]_{N_c \times N_a} \quad (2.102)
\end{aligned}$$

$$\begin{aligned}
[Y_{22mn}] &= \left[j\omega \frac{l_2 l_n \varepsilon_b}{16\pi} \left[\tilde{\boldsymbol{\rho}}_{2m}^{c+} \cdot \left(\tilde{\mathbf{I}}_{\rho\mathbf{G}2m2n}^{b++} + \tilde{\mathbf{I}}_{\rho\mathbf{G}2m2n}^{b+-} \right) + \tilde{\boldsymbol{\rho}}_{2m}^{c-} \cdot \left(\tilde{\mathbf{I}}_{\rho\mathbf{G}2m2n}^{b-+} + \tilde{\mathbf{I}}_{\rho\mathbf{G}2m2n}^{b--} \right) \right] \right. \\
& -j \frac{l_2 l_n}{4\pi\mu_b \omega} \left(\mathbf{I}_{\mathbf{G}2m2n}^{b++} - \mathbf{I}_{\mathbf{G}2m2n}^{b+-} - \mathbf{I}_{\mathbf{G}2m2n}^{b-+} + \mathbf{I}_{\mathbf{G}2m2n}^{b--} \right) \\
& + j\omega \frac{l_2 l_n \varepsilon_c}{8\pi} \left[\tilde{\boldsymbol{\rho}}_{2m}^{c+} \cdot \left(\tilde{\mathbf{I}}_{\rho\mathbf{G}2m2n}^{c++} + \tilde{\mathbf{I}}_{\rho\mathbf{G}2m2n}^{c+-} \right) + \tilde{\boldsymbol{\rho}}_{2m}^{c-} \cdot \left(\tilde{\mathbf{I}}_{\rho\mathbf{G}2m2n}^{c-+} + \tilde{\mathbf{I}}_{\rho\mathbf{G}2m2n}^{c--} \right) \right] \\
& \left. -j \frac{l_2 l_n}{2\pi\mu_c \omega} \left(\mathbf{I}_{\mathbf{G}2m2n}^{c++} - \mathbf{I}_{\mathbf{G}2m2n}^{c+-} - \mathbf{I}_{\mathbf{G}2m2n}^{c-+} + \mathbf{I}_{\mathbf{G}2m2n}^{c--} \right) \right]_{N_c \times N_c} \quad (2.103)
\end{aligned}$$

$$\begin{aligned}
[D_{23mn}] = & \left[\frac{l_{2m}l_n}{16\pi} \left[\vec{\rho}_{2m}^{c+} \cdot (\vec{\mathbf{I}}_{\nabla\mathbf{G}2mn}^{b++} + \vec{\mathbf{I}}_{\nabla\mathbf{G}2mn}^{b+-}) + \vec{\rho}_{2m}^{c-} \cdot (\vec{\mathbf{I}}_{\nabla\mathbf{G}2mn}^{b-+} + \vec{\mathbf{I}}_{\nabla\mathbf{G}2mn}^{b--}) \right] \right. \\
& \left. + \begin{cases} \frac{l_{2m}l_n}{12} \operatorname{sgn} [\vec{\mathbf{n}} \cdot (\vec{\rho}_{2m}^{c\pm} \times \vec{\rho}_n^{c\pm})], & T_{2m}^{\pm} = T_n^{\pm}, m \neq n \\ 0, & \text{otherwise.} \end{cases} \right]_{N_c \times N_b} \quad (2.104)
\end{aligned}$$

$$\begin{aligned}
[C_{31mn}] = & \left[-\frac{l_m l_n}{16\pi} \left[\vec{\rho}_m^{c+} \cdot (\vec{\mathbf{I}}_{\nabla\mathbf{G}m1n}^{b++} + \vec{\mathbf{I}}_{\nabla\mathbf{G}m1n}^{b+-}) + \vec{\rho}_m^{c-} \cdot (\vec{\mathbf{I}}_{\nabla\mathbf{G}m1n}^{b-+} + \vec{\mathbf{I}}_{\nabla\mathbf{G}m1n}^{b--}) \right] \right. \\
& \left. - \begin{cases} \frac{l_m l_n}{12} \operatorname{sgn} [\vec{\mathbf{n}} \cdot (\vec{\rho}_m^{c\pm} \times \vec{\rho}_{1n}^{c\pm})], & T_m^{\pm} = T_{1n}^{\pm}, m \neq n \\ 0, & \text{otherwise.} \end{cases} \right]_{N_b \times N_a} \quad (2.105)
\end{aligned}$$

$$\begin{aligned}
[C_{32mn}] = & \left[-\frac{l_m l_n}{16\pi} \left[\vec{\rho}_m^{c+} \cdot (\vec{\mathbf{I}}_{\nabla\mathbf{G}m2n}^{b++} + \vec{\mathbf{I}}_{\nabla\mathbf{G}m2n}^{b+-}) + \vec{\rho}_m^{c-} \cdot (\vec{\mathbf{I}}_{\nabla\mathbf{G}m2n}^{b-+} + \vec{\mathbf{I}}_{\nabla\mathbf{G}m2n}^{b--}) \right] \right. \\
& \left. - \begin{cases} \frac{l_m l_n}{12} \operatorname{sgn} [\vec{\mathbf{n}} \cdot (\vec{\rho}_m^{c\pm} \times \vec{\rho}_{2n}^{c\pm})], & T_m^{\pm} = T_{2n}^{\pm}, m \neq n \\ 0, & \text{otherwise.} \end{cases} \right]_{N_b \times N_c} \quad (2.106)
\end{aligned}$$

$$\begin{aligned}
[Z_{33mn}] = & \left[j\omega \frac{l_m l_n \mu_b}{16\pi} \left[\vec{\rho}_m^{c+} \cdot (\vec{\mathbf{I}}_{\rho\mathbf{G}mn}^{b++} + \vec{\mathbf{I}}_{\rho\mathbf{G}mn}^{b+-}) + \vec{\rho}_m^{c-} \cdot (\vec{\mathbf{I}}_{\rho\mathbf{G}mn}^{b-+} + \vec{\mathbf{I}}_{\rho\mathbf{G}mn}^{b--}) \right] \right. \\
& \left. - j \frac{l_m l_n}{4\pi\epsilon_b \omega} (\mathbf{I}_{\mathbf{G}mn}^{b++} - \mathbf{I}_{\mathbf{G}mn}^{b+-} - \mathbf{I}_{\mathbf{G}mn}^{b-+} + \mathbf{I}_{\mathbf{G}mn}^{b--}) \right]_{N_b \times N_b} \quad (2.107)
\end{aligned}$$

The subscripts “tan” are suppressed in (2.99)–(2.107) because only the tangential components of the integrals contribute to the symmetric products. The superscripts “a”, “b”, and “c” of $\vec{\mathbf{I}}_{\rho\mathbf{G}}$, $\mathbf{I}_{\mathbf{G}}$, and $\vec{\mathbf{I}}_{\nabla\mathbf{G}}$ mean that the integrals are calculated using the wavenumbers k_a , k_b , and k_c respectively. The first “±” superscripts of $\vec{\mathbf{I}}_{\rho\mathbf{G}}$, $\mathbf{I}_{\mathbf{G}}$, and $\vec{\mathbf{I}}_{\nabla\mathbf{G}}$ indicate that the integrals are evaluated at the centroids of T_m^{\pm} triangles, and the second “±” superscripts indicate that the integrands are integrated over T_n^{\pm} triangles. The

subscripts “1*m*” and “1*n*” of $\vec{\mathbf{I}}_{\rho\mathbf{G}}$, $\mathbf{I}_{\mathbf{G}}$, and $\vec{\mathbf{I}}_{\nabla\mathbf{G}}$ stand for “top aperture T_m ” and “top aperture T_n ”, the subscripts “2*m*” and “2*n*” stand for “bottom aperture T_m ” and “bottom aperture T_n ”, and the sole subscripts “*m*” and “*n*” stand for “closed cavity surface T_m ” and “closed cavity surface T_n ”.

2.5 Calculated Quantities

After setting up the matrices in (2.48) per the previous section, the matrix equation is solved. The solution gives the unknown coefficients matrix. Then the currents $\vec{\mathbf{M}}_1$, $\vec{\mathbf{M}}_2$ and $\vec{\mathbf{J}}$ are calculated according to (2.36)–(2.38). Once the currents are known, fields anywhere can be calculated using the following equations:

In region *a* (using (2.11) and (2.12));

$$\vec{\mathbf{E}}^a(\vec{\mathbf{r}}) = \vec{\mathbf{E}}^{\text{inc}} + \vec{\mathbf{E}}^{\text{inc,img}} - \frac{1}{4\pi} \sum_{n=1}^{N_a} v_n l_{1n} \left(\vec{\mathbf{I}}_{\nabla\mathbf{G}1n}^{a+} + \vec{\mathbf{I}}_{\nabla\mathbf{G}1n}^{a-} \right) \quad (2.108)$$

$$\vec{\mathbf{H}}^a(\vec{\mathbf{r}}) = \vec{\mathbf{H}}^{\text{inc}} + \vec{\mathbf{H}}^{\text{inc,img}} - j \frac{1}{2\pi} \sum_{n=1}^{N_a} v_n l_{1n} \left[\frac{\epsilon_a \omega}{2} \left(\vec{\mathbf{I}}_{\rho\mathbf{G}1n}^{a+} + \vec{\mathbf{I}}_{\rho\mathbf{G}1n}^{a-} \right) + \frac{1}{\mu_a \omega} \nabla \left(\mathbf{I}_{\mathbf{G}1n}^{a+} - \mathbf{I}_{\mathbf{G}1n}^{a-} \right) \right] \quad (2.109)$$

In region *b* (using (2.16) and (2.17));

$$\begin{aligned} \vec{\mathbf{E}}^b(\vec{\mathbf{r}}) = & \frac{1}{8\pi} \sum_{n=1}^{N_a} v_n l_{1n} \left(\vec{\mathbf{I}}_{\nabla\mathbf{G}1n}^{b+} + \vec{\mathbf{I}}_{\nabla\mathbf{G}1n}^{b-} \right) + \frac{1}{8\pi} \sum_{n=1}^{N_c} u_n l_{2n} \left(\vec{\mathbf{I}}_{\nabla\mathbf{G}2n}^{b+} + \vec{\mathbf{I}}_{\nabla\mathbf{G}2n}^{b-} \right) \\ & - j \frac{1}{4\pi} \sum_{n=1}^{N_b} y_n l_n \left[\frac{\mu_b \omega}{2} \left(\vec{\mathbf{I}}_{\rho\mathbf{G}n}^{b+} + \vec{\mathbf{I}}_{\rho\mathbf{G}n}^{b-} \right) + \frac{1}{\epsilon_b \omega} \nabla \left(\mathbf{I}_{\mathbf{G}n}^{b+} - \mathbf{I}_{\mathbf{G}n}^{b-} \right) \right] \end{aligned} \quad (2.110)$$

$$\begin{aligned} \vec{\mathbf{H}}^b(\vec{\mathbf{r}}) = & j \frac{1}{4\pi} \sum_{n=1}^{N_a} v_n l_{1n} \left[\frac{\epsilon_b \omega}{2} \left(\vec{\mathbf{I}}_{\rho\mathbf{G}1n}^{b+} + \vec{\mathbf{I}}_{\rho\mathbf{G}1n}^{b-} \right) + \frac{1}{\mu_b \omega} \nabla \left(\mathbf{I}_{\mathbf{G}1n}^{b+} - \mathbf{I}_{\mathbf{G}1n}^{b-} \right) \right] \\ & + j \frac{1}{4\pi} \sum_{n=1}^{N_c} u_n l_{2n} \left[\frac{\epsilon_b \omega}{2} \left(\vec{\mathbf{I}}_{\rho\mathbf{G}2n}^{b+} + \vec{\mathbf{I}}_{\rho\mathbf{G}2n}^{b-} \right) + \frac{1}{\mu_b \omega} \nabla \left(\mathbf{I}_{\mathbf{G}2n}^{b+} - \mathbf{I}_{\mathbf{G}2n}^{b-} \right) \right] \end{aligned}$$

$$+\frac{1}{8\pi}\sum_{n=1}^{N_b}y_n l_n\left(\vec{\mathbf{I}}_{\nabla\mathbf{G}_n}^{b+}+\vec{\mathbf{I}}_{\nabla\mathbf{G}_n}^{b-}\right) \quad (2.111)$$

In region c (using (2.22) and (2.23));

$$\vec{\mathbf{E}}^c(\vec{\mathbf{r}})=-\frac{1}{4\pi}\sum_{n=1}^{N_c}u_n l_{2n}\left(\vec{\mathbf{I}}_{\nabla\mathbf{G}_{2n}}^{c+}+\vec{\mathbf{I}}_{\nabla\mathbf{G}_{2n}}^{c-}\right) \quad (2.112)$$

$$\vec{\mathbf{H}}^c(\vec{\mathbf{r}})=-j\frac{1}{2\pi}\sum_{n=1}^{N_c}u_n l_{2n}\left[\frac{\epsilon_c\omega}{2}\left(\vec{\mathbf{I}}_{\rho\mathbf{G}_{2n}}^{c+}+\vec{\mathbf{I}}_{\rho\mathbf{G}_{2n}}^{c-}\right)+\frac{1}{\mu_c\omega}\nabla\left(\mathbf{I}_{\mathbf{G}_{2n}}^{c+}-\mathbf{I}_{\mathbf{G}_{2n}}^{c-}\right)\right], \quad (2.113)$$

where the integrals appearing in the expressions are defined similar to (2.96)–(2.98), such

as

$$\vec{\mathbf{I}}_{\rho\mathbf{G}_n}=\frac{1}{A_n}\iint_{T_n}\vec{\mathbf{p}}_n\frac{e^{-jk|\vec{\mathbf{r}}-\vec{\mathbf{r}}'|}}{|\vec{\mathbf{r}}-\vec{\mathbf{r}}'|}ds' \quad (2.114)$$

$$\mathbf{I}_{\mathbf{G}_n}=\frac{1}{A_n}\iint_{T_n}\frac{e^{-jk|\vec{\mathbf{r}}-\vec{\mathbf{r}}'|}}{|\vec{\mathbf{r}}-\vec{\mathbf{r}}'|}ds' \quad (2.115)$$

$$\vec{\mathbf{I}}_{\nabla\mathbf{G}_n}=\frac{1}{A_n}\iint_{T_n}\vec{\mathbf{p}}_n\times(\vec{\mathbf{r}}-\vec{\mathbf{r}}')(1+jk|\vec{\mathbf{r}}-\vec{\mathbf{r}}'|)\frac{e^{-jk|\vec{\mathbf{r}}-\vec{\mathbf{r}}'|}}{|\vec{\mathbf{r}}-\vec{\mathbf{r}}'|^3}ds'. \quad (2.116)$$

CHAPTER 3

NUMERICAL RESULTS

In this chapter, solutions for several geometries will be presented. The solutions are obtained using the formulation developed in Chapter 2. This formulation is implemented in a computer program using MATLAB [50] and then verified by comparing the results to previously published results. After the verification, a novel case is solved and the results are presented.

In all cases, only the cavity region of the problem is going to be shown. The cavity region includes the top and the bottom apertures, and the cavity walls connecting the apertures. This cavity is situated in an infinite ground plane which has a thickness “ d ”. However, this infinite ground plane is not going to be shown in the figures of the problem geometries.

All structures are illuminated with plane waves (2.63) radiated by the sources at infinity and these waves are impinging on the top aperture in region a . The wavelength λ is taken to be 1 meter.

3.1 Results for Square Apertures

The first problem that is going to be analyzed is a thick conductor with square apertures on the top and the bottom. This problem is previously solved using Finite Element Method by J. M. Jin and J. L. Volakis [29]. The results in this research will be compared with their results.

The problem geometry and the meshing of the structure are shown in Fig. 3.1. The sides of the apertures are $l = w = 0.4\lambda$ and the conductor thickness is $d = 0.25\lambda$.

The triangular meshing is done in such a way that the triangles are more refined on the edges and on x and y axes on apertures. The currents rapidly change on the edges so keeping the triangles smaller closer to the edges helps to reduce the error. The currents are plotted along x and y axes; having finer triangles along the axes results in smoother plots.

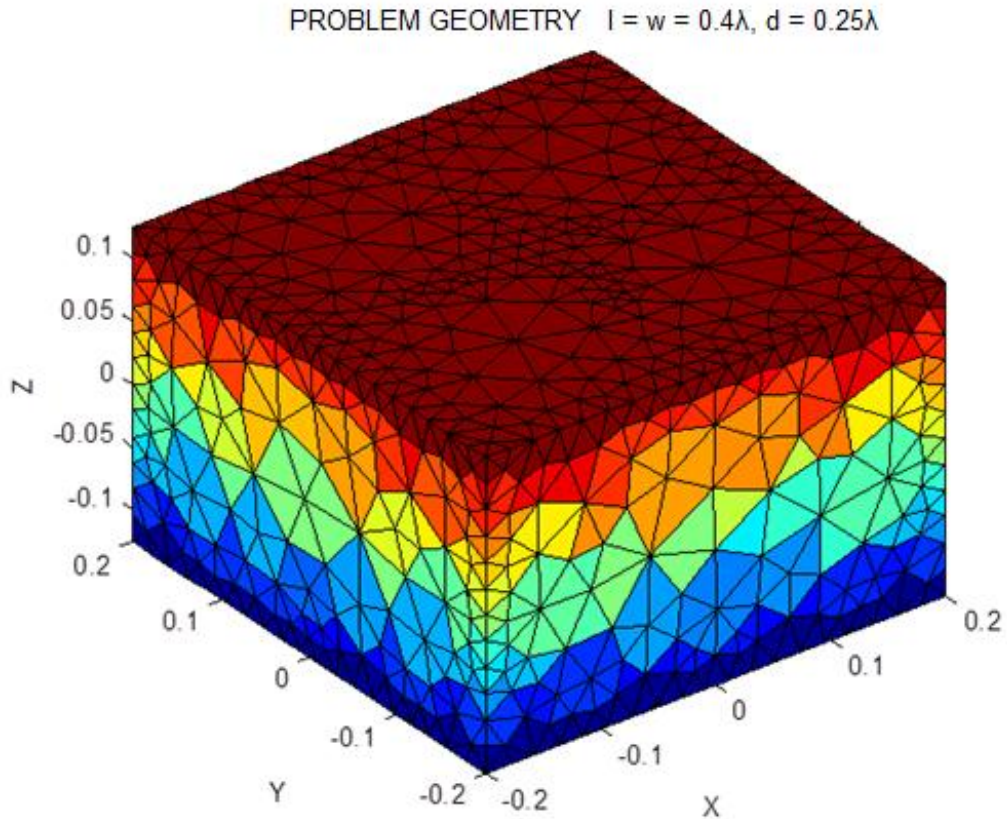


Fig. 3.1 Triangular meshing of the problem with square apertures (0.4λ -by- 0.4λ) on top and bottom; conductor thickness $d = 0.25\lambda$, $\epsilon_a = \epsilon_b = \epsilon_c = \epsilon_0$, $\mu_a = \mu_b = \mu_c = \mu_0$, $\vec{\mathbf{E}}^{\text{inc}} = \vec{\mathbf{x}}e^{jkz}$.

The problem in Fig. 3.1 is excited with a plane wave on normal incidence with polarization given as $\vec{\mathbf{E}}^{\text{inc}} = \vec{\mathbf{x}}e^{jkz}$. All regions are filled with (ϵ_0, μ_0) . The electric fields on the apertures computed in [29] are given in Fig. 3.2 and Fig. 3.4 The electric fields calculated using the MoM formulation in this research are given in Fig. 3.3 and Fig. 3.5.

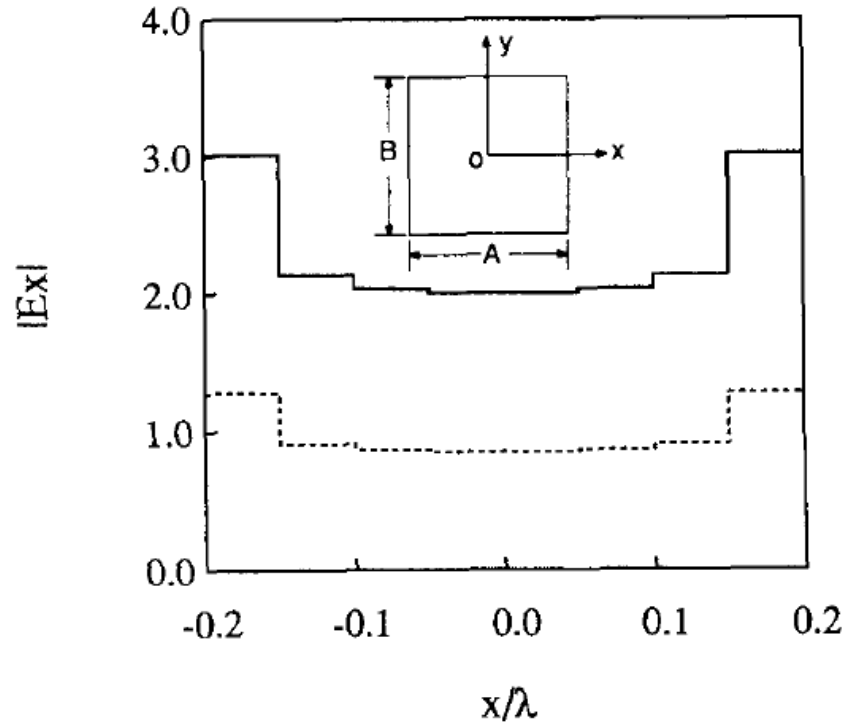


Fig. 3.2 Electric field along x -axis at the upper (solid line) and lower (dashed line) apertures [29].

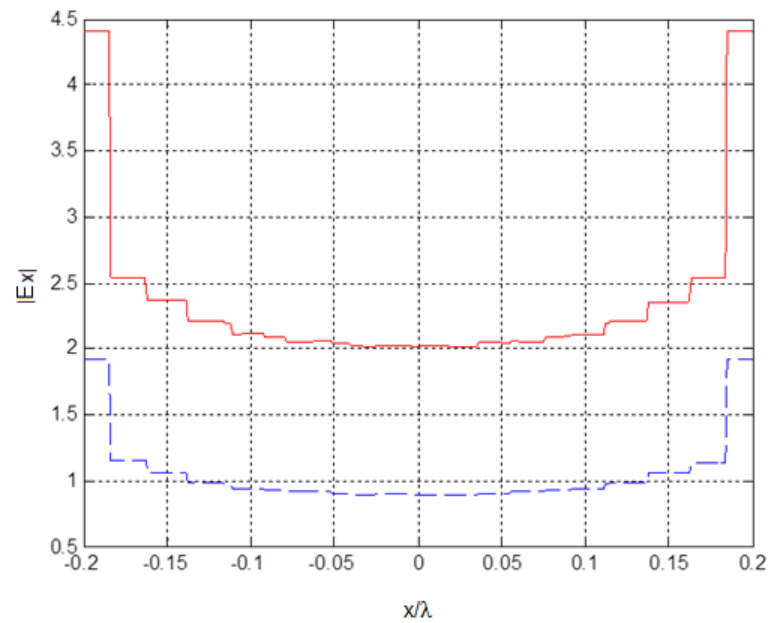


Fig. 3.3 Electric field at the upper (solid line) and lower (dashed line) apertures.

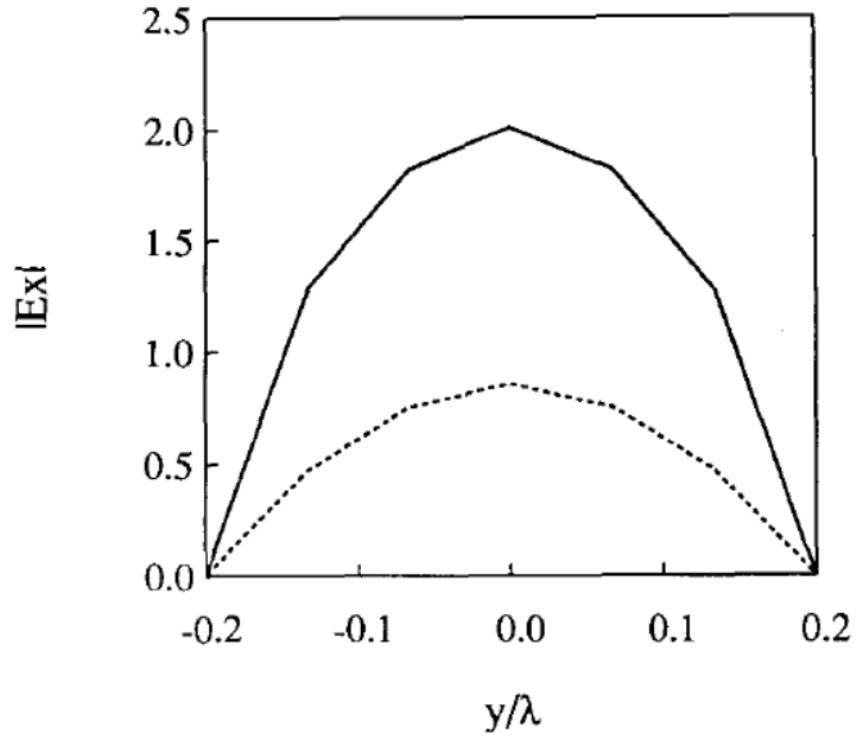


Fig. 3.4 Electric field along y -axis at the upper (solid line) and lower (dashed line) apertures [29].

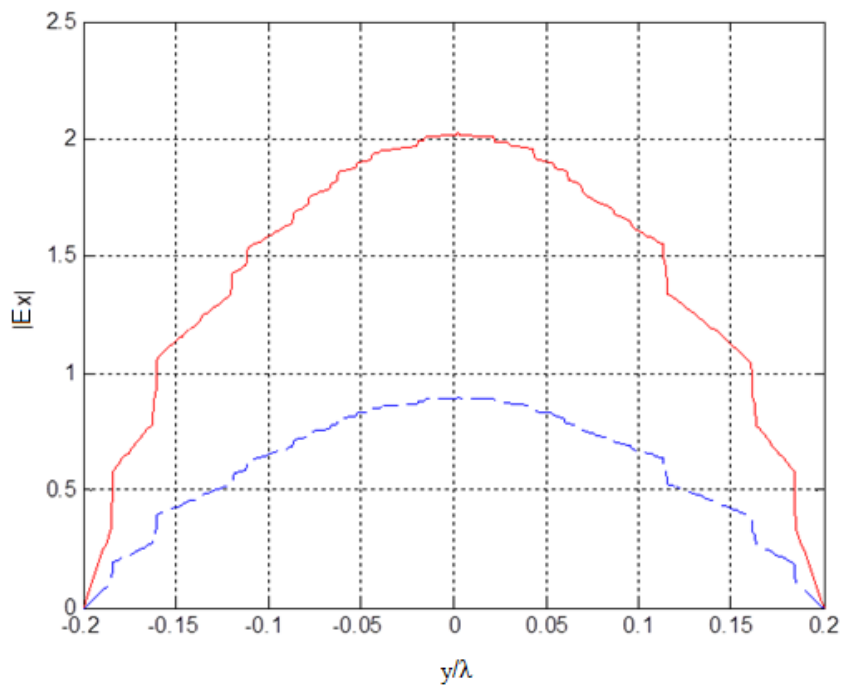


Fig. 3.5 Electric field at the upper (solid line) and lower (dashed line) apertures

Next, the backscattering cross section (RCS) and the transmission coefficient T of the structure are compared. The backscattering cross section is defined as [29]

$$\sigma(\theta, \phi) = \lim_{r \rightarrow \infty} 4\pi r^2 \frac{|\vec{\mathbf{H}}^s(\vec{\mathbf{r}})|^2}{|\vec{\mathbf{H}}^{\text{inc}}|^2}, \quad (3.1)$$

where $\vec{\mathbf{H}}^s(\vec{\mathbf{r}})$ is the far zone scattered field, which is the actual field in the backward direction minus the field that would exist if the entire $z=0$ plane was perfectly conducting. The transmission coefficient is defined as

$$T = \frac{P_{\text{trans}}}{P_{\text{inc}}} = \frac{\text{Re} \left(\iint_{\text{bot.aper.}} (\vec{\mathbf{E}}_c^* \times \vec{\mathbf{H}}_c) \cdot \vec{\mathbf{n}}_c ds \right)}{\eta_a |\vec{\mathbf{H}}^{\text{inc}}|^2 A_1 \cos \theta^{\text{inc}}}, \quad (3.2)$$

where P_{inc} is the time average incident power that would be intercepted by the top aperture if all space was free space, P_{trans} is the time average power transmitted to region c through the bottom aperture, η_a is the impedance of region a , and A_1 is the area of the top aperture.

RCS and transmission coefficient plots of the problem in Fig. 3.1 computed by [29] are given in Fig. 3.6 and Fig. 3.8. Comparable results of this research are given in Fig. 3.7 and Fig. 3.9. As seen from Fig. 3.2–Fig. 3.9, the results are very close to each other for square apertures on top and bottom in a thick conductor.

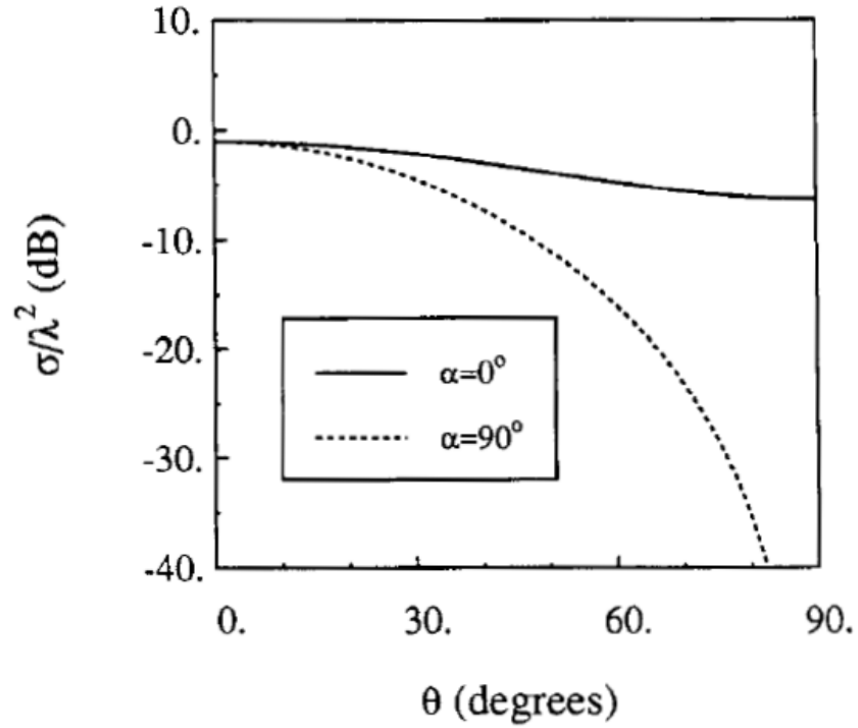


Fig. 3.6 Backscatter RCS of the structure in Fig. 3.1 as a function of incidence angle in the

$$\phi = 0^\circ \text{ plane; } \vec{\mathbf{E}}^{\text{inc}}(\vec{\mathbf{r}}) = (\vec{\mathbf{\theta}}^{\text{inc}} \cos \alpha + \vec{\mathbf{\phi}}^{\text{inc}} \sin \alpha) e^{-j\vec{\mathbf{k}}^{\text{inc}} \cdot \vec{\mathbf{r}}} \quad [29].$$

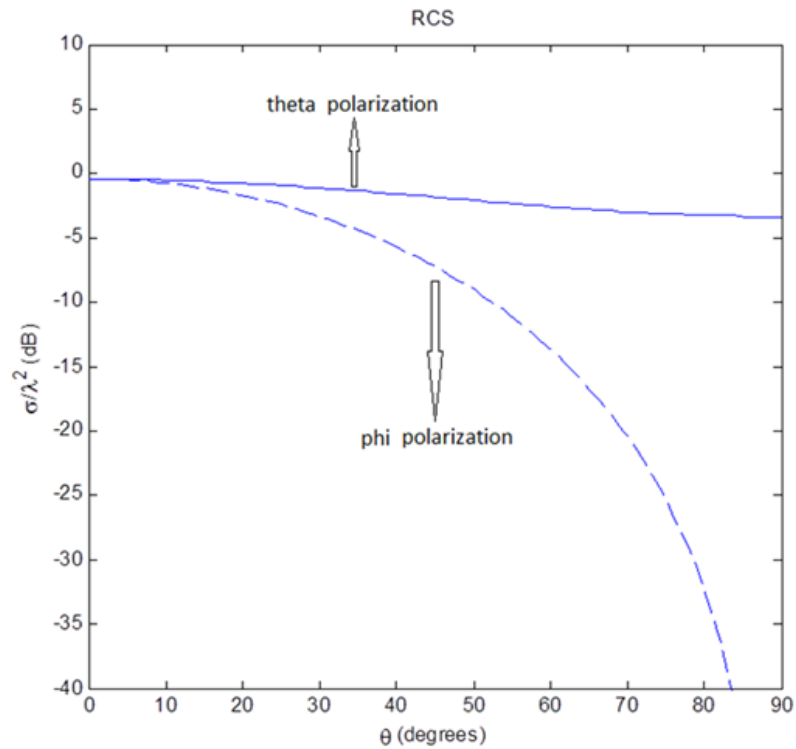


Fig. 3.7 Backscatter RCS of the structure in Fig. 3.1.

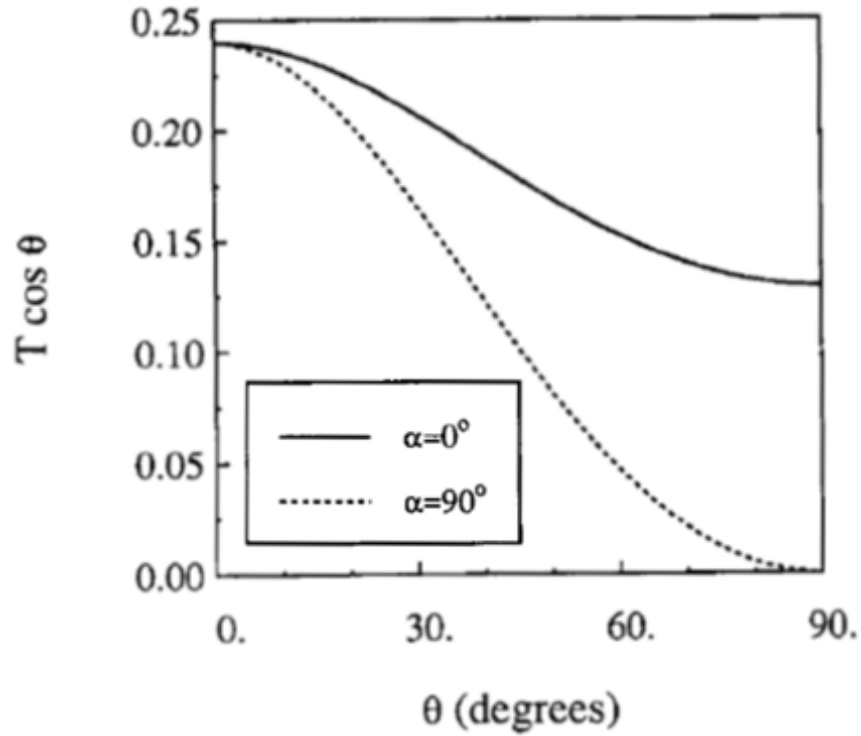


Fig. 3.8 Transmission coefficient plots of the structure in Fig. 3.1 as a function of incidence

angle in the $\phi = 0^\circ$ plane; $\vec{\mathbf{E}}^{\text{inc}}(\vec{\mathbf{r}}) = (\vec{\boldsymbol{\theta}}^{\text{inc}} \cos \alpha + \vec{\boldsymbol{\phi}}^{\text{inc}} \sin \alpha) e^{-j\vec{\mathbf{k}}^{\text{inc}} \cdot \vec{\mathbf{r}}}$ [29].

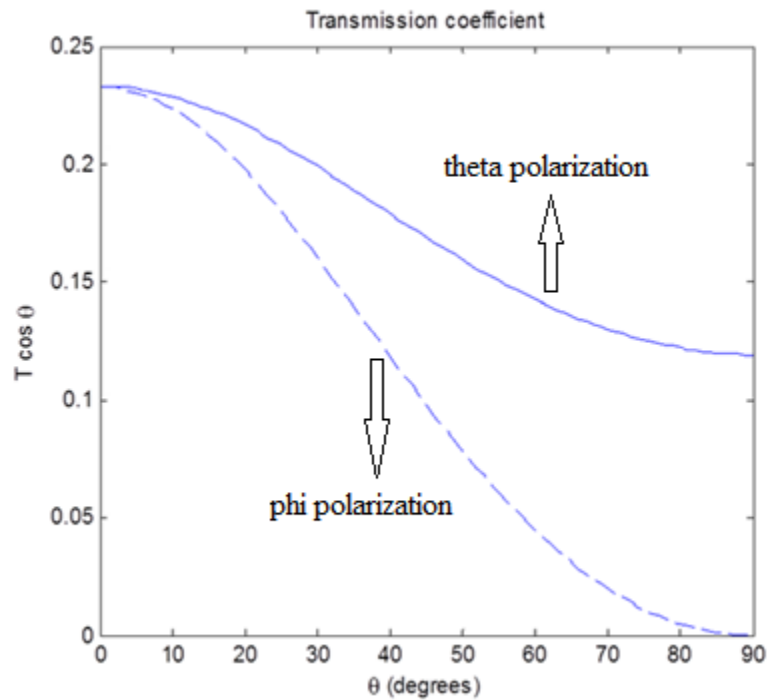


Fig. 3.9 Transmission coefficient plots of the structure in Fig. 3.1.

3.2 Results for a Cross Aperture

A cross aperture on top and bottom is analyzed next. The cavity walls inside the conductor form a square prism and the top and bottom walls are cross-shaped apertures. The geometry is shown in Fig. 3.10 and the meshing is shown in Fig. 3.11.

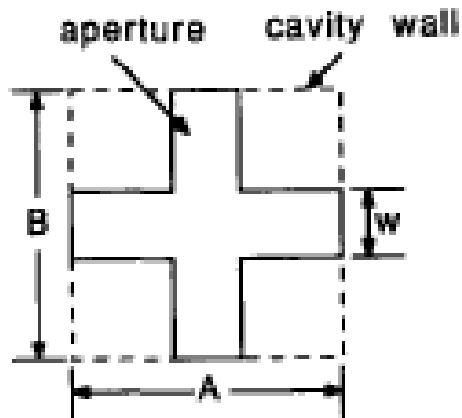


Fig. 3.10 Cross shaped aperture with $A = B = 0.5\lambda$, $w = 0.125\lambda$, conductor thickness

$$d = 0.25\lambda, \epsilon_a = \epsilon_b = \epsilon_c = \epsilon_0, \mu_a = \mu_b = \mu_c = \mu_0.$$

PROBLEM GEOMETRY $A = B = 0.5\lambda$, $w = 0.125\lambda$, $d = 0.25\lambda$

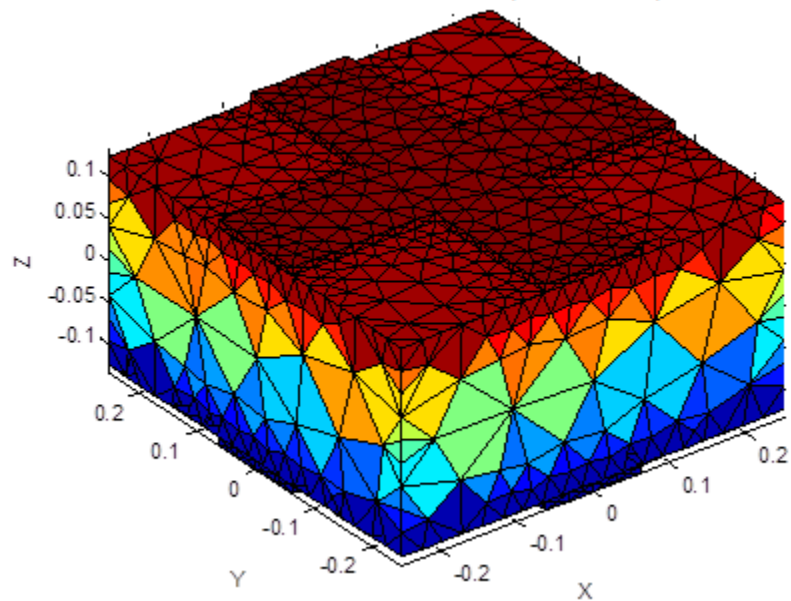


Fig. 3.11 Meshing of the problem in Fig. 3.10.

RCS and transmission coefficient plots are given as Fig. 3.12 and Fig. 3.14 by [29]. The results of this research are given in Fig. 3.13 and Fig. 3.15.

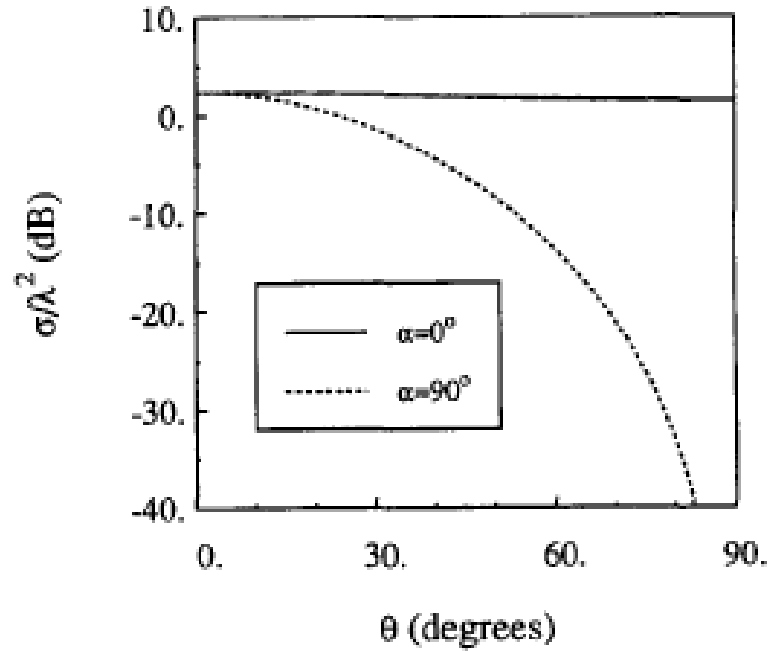


Fig. 3.12 Backscatter RCS of the structure in Fig. 3.11 as a function of incidence in the

$\phi = 0^\circ$ plane; $\vec{\mathbf{E}}^{\text{inc}}(\vec{\mathbf{r}}) = (\vec{\boldsymbol{\theta}}^{\text{inc}} \cos \alpha + \vec{\boldsymbol{\phi}}^{\text{inc}} \sin \alpha) e^{-j\vec{\mathbf{k}}^{\text{inc}} \cdot \vec{\mathbf{r}}}$ [29].

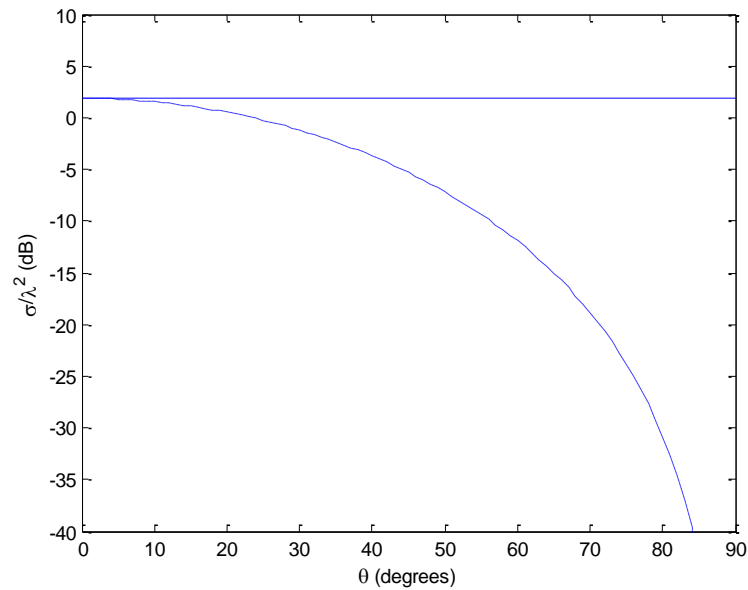


Fig. 3.13 Backscatter RCS of Fig. 3.11

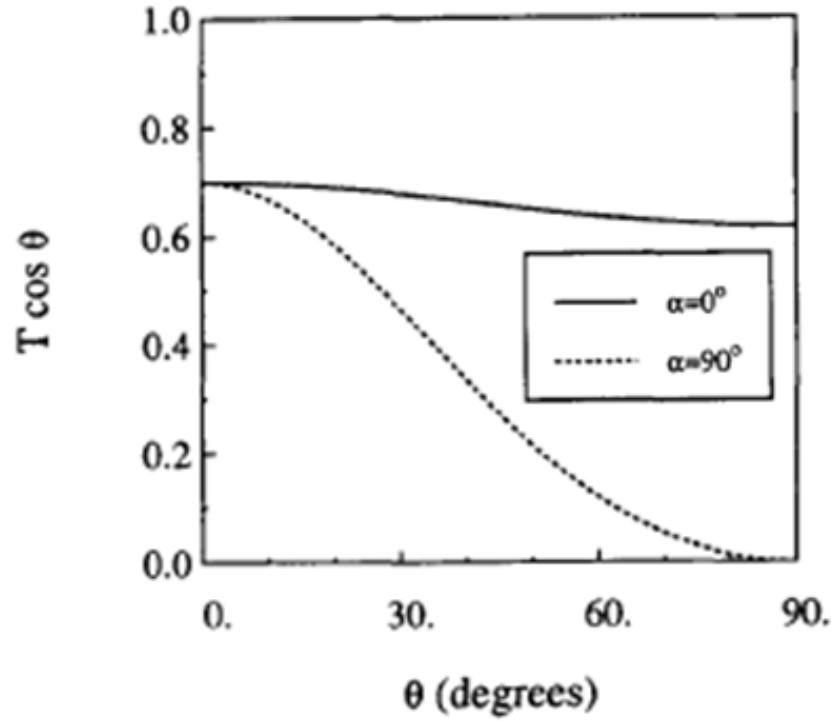


Fig. 3.14 Transmission coefficient plots of the structure in Fig. 3.11 as a function of incidence

angle in the $\phi = 0^\circ$ plane; $\vec{\mathbf{E}}^{\text{inc}}(\vec{\mathbf{r}}) = (\vec{\boldsymbol{\theta}}^{\text{inc}} \cos \alpha + \vec{\boldsymbol{\phi}}^{\text{inc}} \sin \alpha) e^{-j\vec{\mathbf{k}}^{\text{inc}} \cdot \vec{\mathbf{r}}}$ [29].

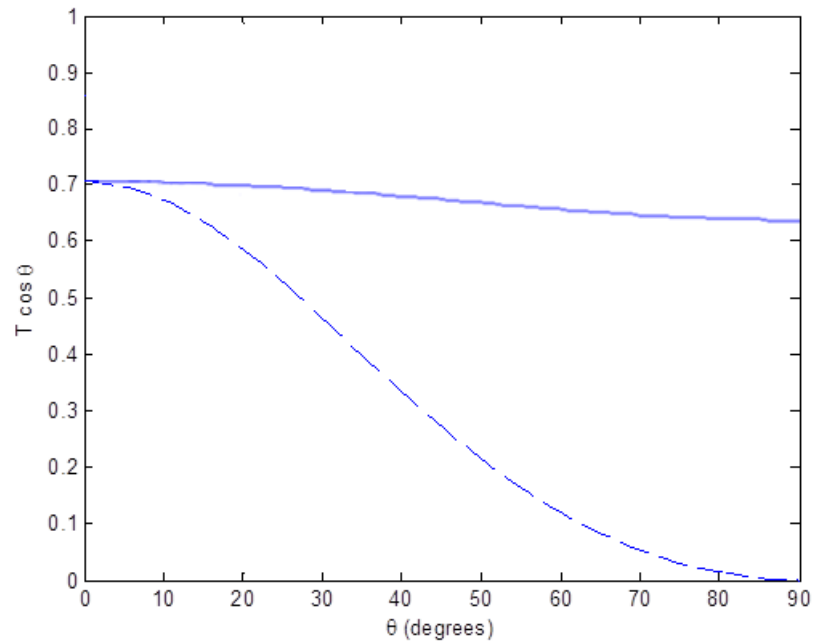


Fig. 3.15 Transmission coefficient plots of the structure in Fig. 3.11.

The results of the FEM method in [29] are very similar to the results of the moment method used in this research. These results validate the accuracy of the method proposed in this thesis.

3.3 Results for Circular Apertures

A cylindrical cavity with small circular apertures whose centers are on the z -axis is analyzed. The geometry is shown in Fig. 3.16. The radii of the small apertures are $r = 0.05\lambda$. The radius of the cylindrical cavity is $R = 0.5\lambda$. The thickness of the conductor is $d = 0.6\lambda$. The flanges covering the cylindrical cavity and forming small circular apertures on top and bottom have a thickness of 0.01λ . All regions are filled with (ϵ_0, μ_0) . The incident field is $\vec{\mathbf{E}}^{\text{inc}} = \vec{\mathbf{y}}e^{jkz}$. The meshing of the problem is shown in Fig. 3.17. The magnetic currents on the top and bottom apertures along x and y axes are in Fig. 3.18 and Fig. 3.19.

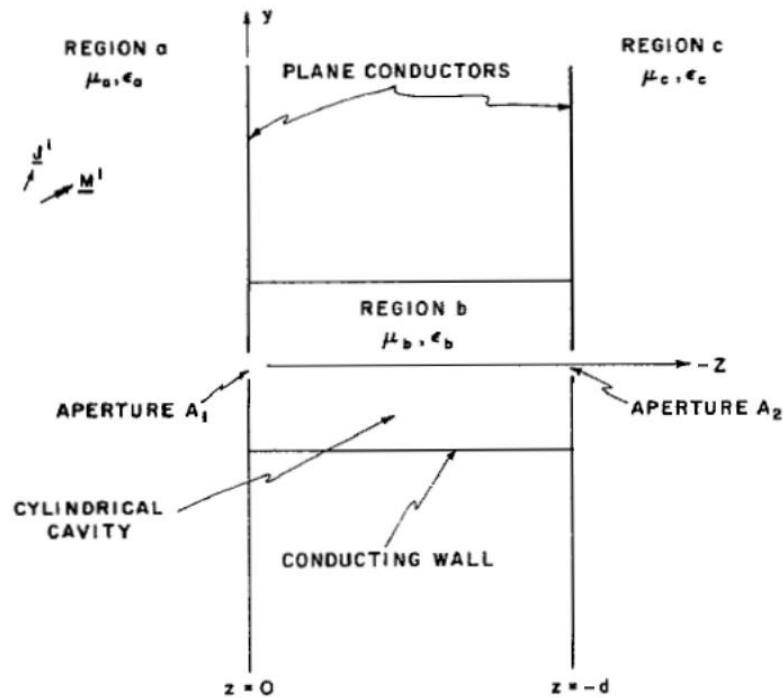


Fig. 3.16 A cylindrical cavity with small circular apertures in a thick ground plane [21].

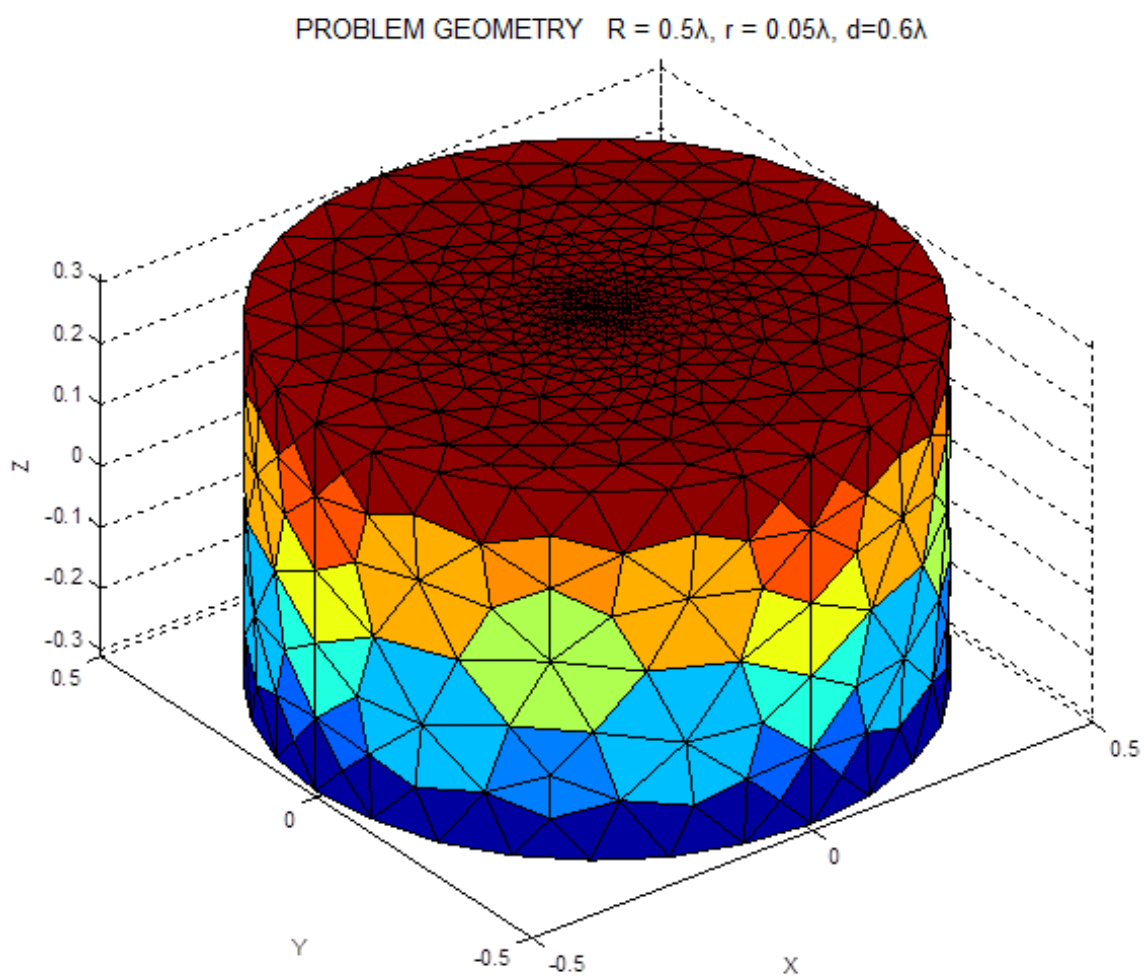


Fig. 3.17 Meshing of the structure in Fig. 3.16, $\vec{\mathbf{E}}^{\text{inc}} = \vec{\mathbf{y}}e^{jkz}$.

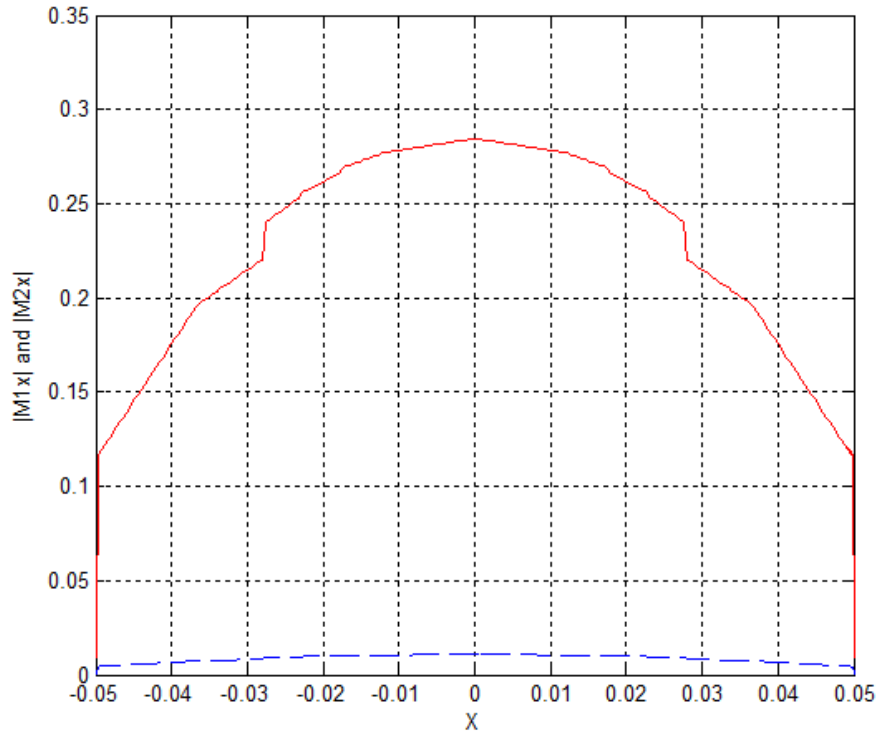


Fig. 3.18 Magnetic current on top aperture (solid line) and on bottom aperture (dashed line) along the x -axis for the problem in Fig. 3.16.

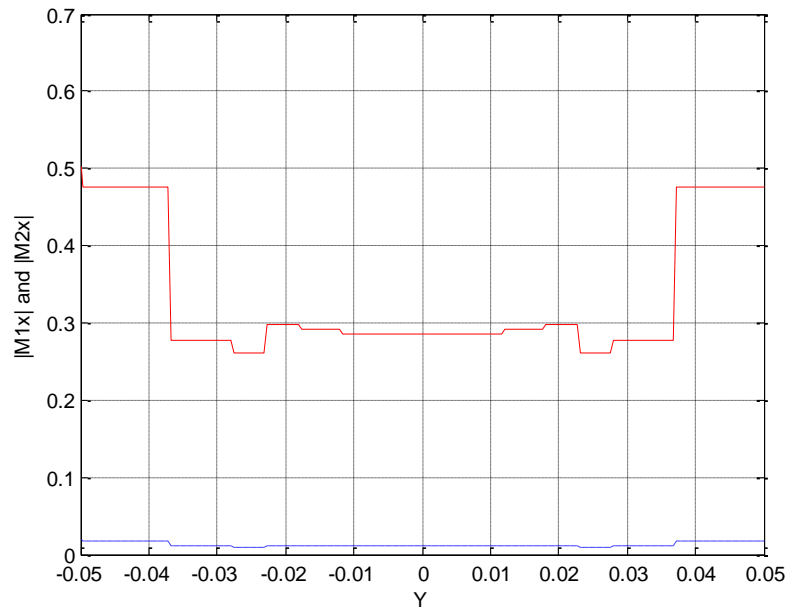


Fig. 3.19 Magnetic current on top aperture (solid line) and on bottom aperture (dashed line) along the y -axis for the problem in Fig. 3.16.

3.4 Effect of Conductor Thickness

Square apertures with varying conductor thicknesses are analyzed to understand the effect of thickness on transmission of the plane wave through the cavity. The problem geometries and corresponding magnetic current plots for the top and bottom apertures are given in Fig. 3.20 through Fig. 3.31.

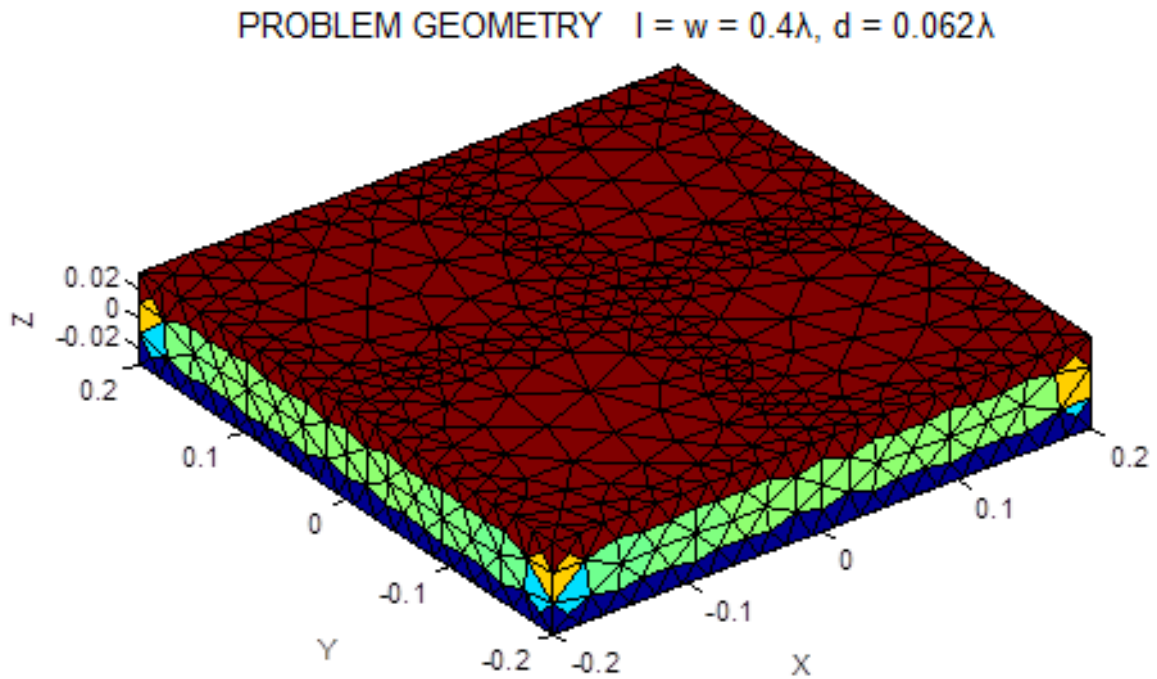


Fig. 3.20 Triangular meshing of the problem with square apertures (0.4λ -by- 0.4λ) on top and bottom; conductor thickness $d = 0.062\lambda$, $\epsilon_a = \epsilon_b = \epsilon_c = \epsilon_0$, $\mu_a = \mu_b = \mu_c = \mu_0$, $\vec{\mathbf{E}}^{\text{inc}} = \vec{\mathbf{y}}e^{jkz}$.

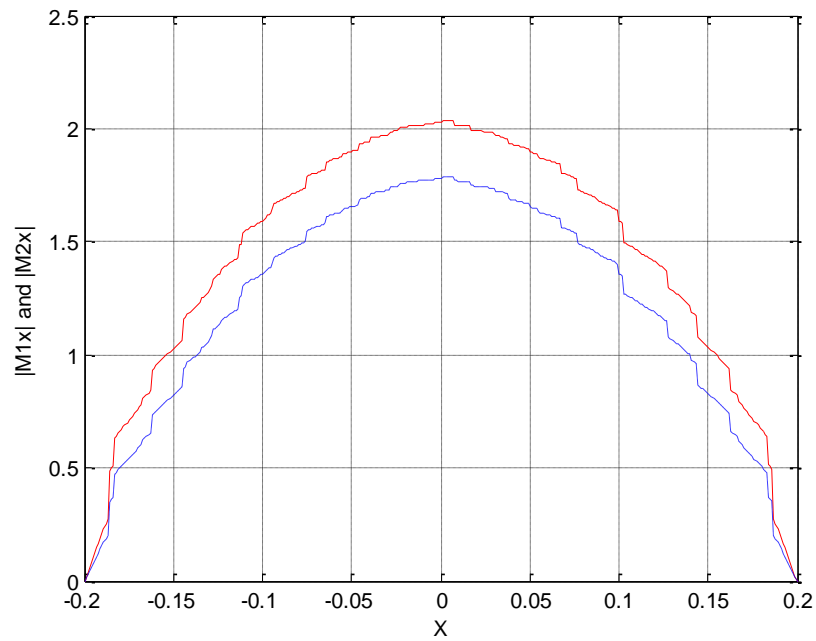


Fig. 3.21 Magnetic current on top aperture (solid line) and on bottom aperture (dashed line) along the x -axis for the problem in Fig. 3.20.

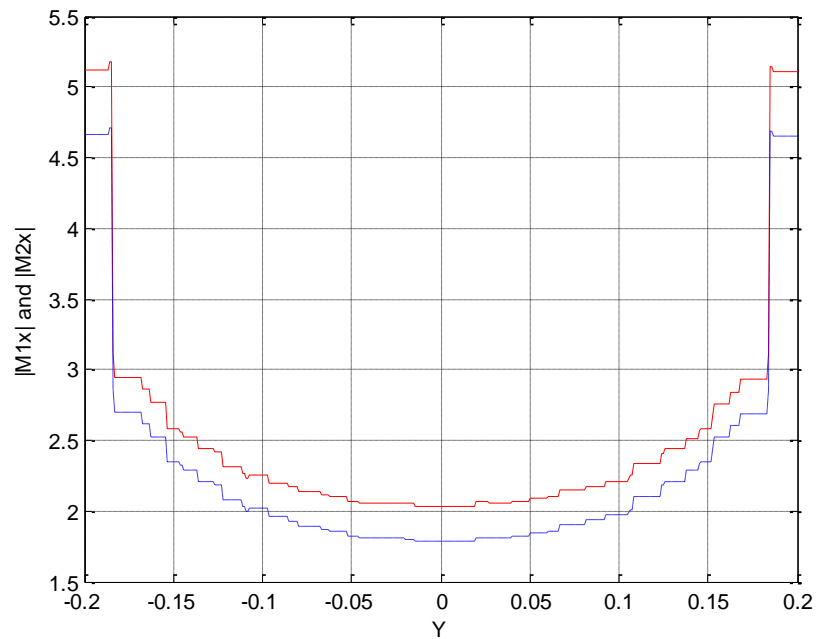


Fig. 3.22 Magnetic current on top aperture (solid line) and on bottom aperture (dashed line) along the y -axis for the problem in Fig. 3.20.

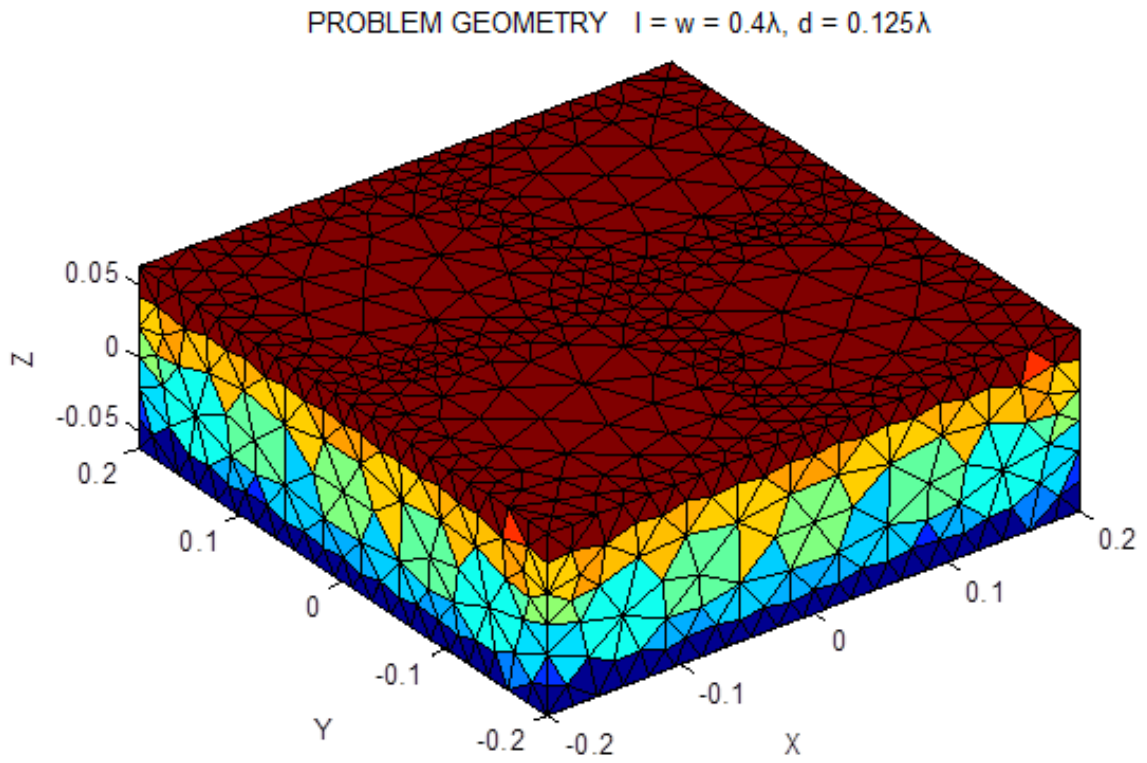


Fig. 3.23 Triangular meshing of the problem with square apertures (0.4λ -by- 0.4λ) on top and bottom; conductor thickness $d = 0.125\lambda$, $\varepsilon_a = \varepsilon_b = \varepsilon_c = \varepsilon_0$, $\mu_a = \mu_b = \mu_c = \mu_0$, $\vec{\mathbf{E}}^{\text{inc}} = \vec{\mathbf{y}}e^{jkz}$.

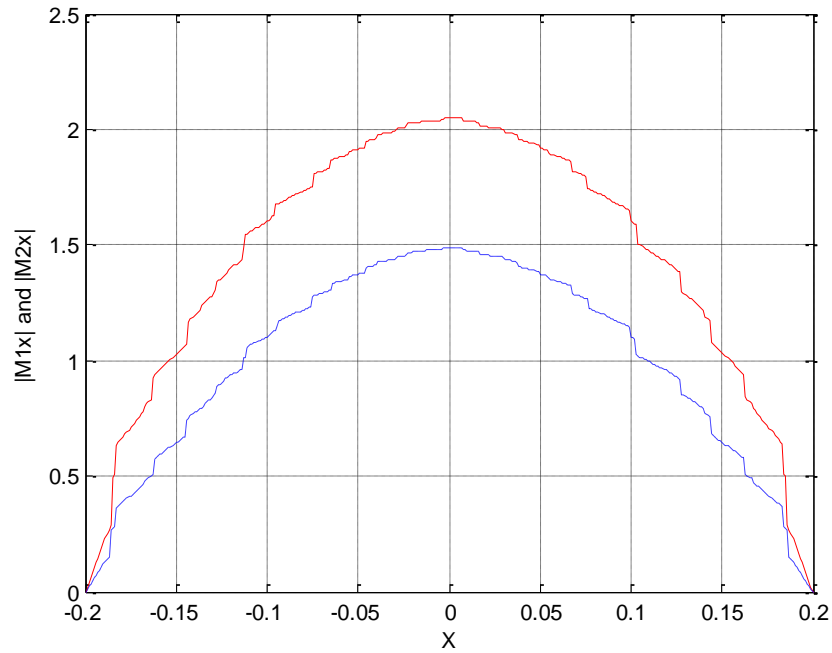


Fig. 3.24 Magnetic current on top aperture (solid line) and on bottom aperture (dashed line) along the x -axis for the problem in Fig. 3.23.

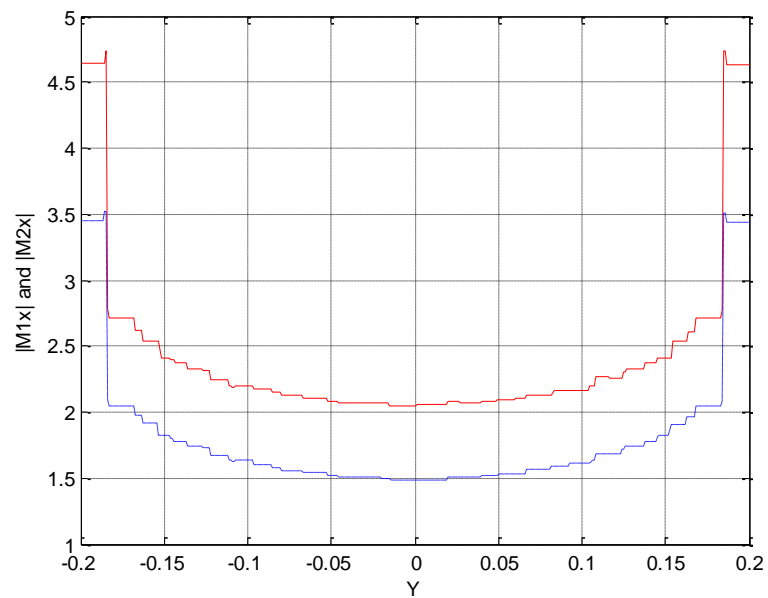


Fig. 3.25 Magnetic current on top aperture (solid line) and on bottom aperture (dashed line) along the y -axis for the problem in Fig. 3.23.

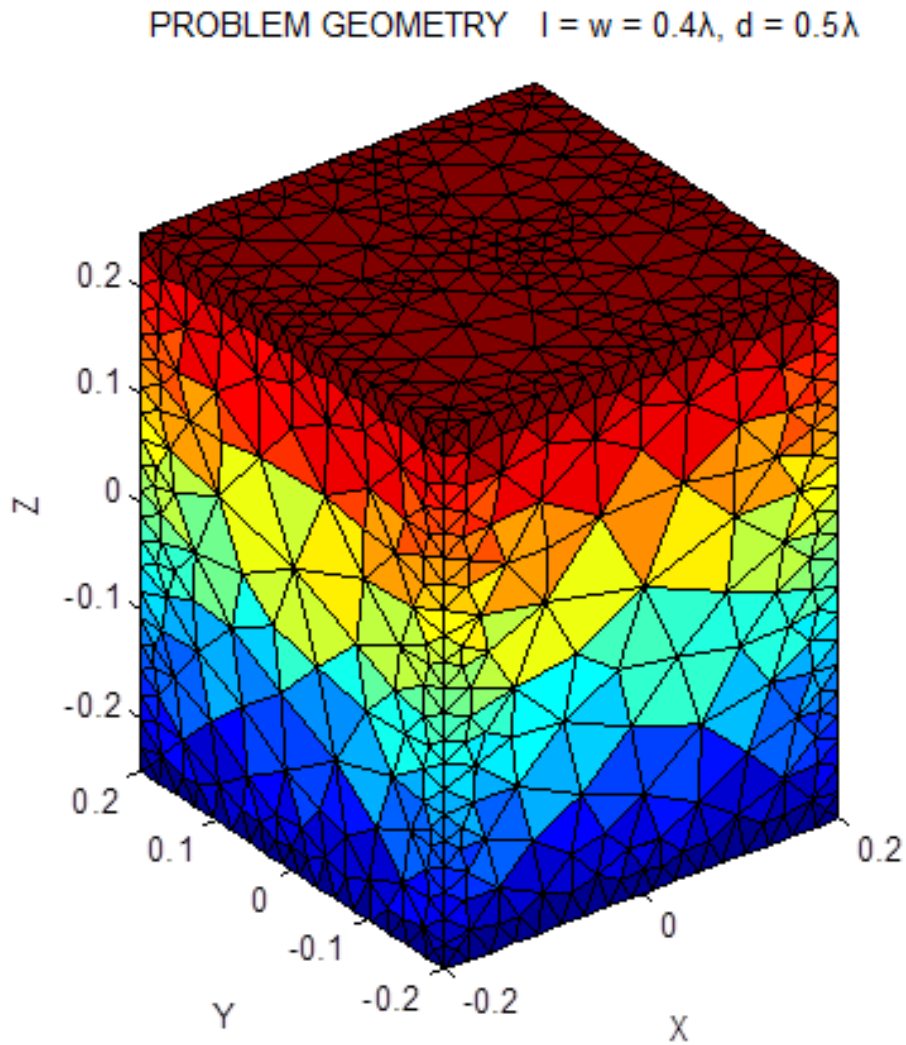


Fig. 3.26 Triangular meshing of the problem with square apertures (0.4λ -by- 0.4λ) on top and bottom; conductor thickness $d = 0.5\lambda$, $\varepsilon_a = \varepsilon_b = \varepsilon_c = \varepsilon_0$, $\mu_a = \mu_b = \mu_c = \mu_0$, $\vec{\mathbf{E}}^{\text{inc}} = \vec{\mathbf{y}}e^{jkz}$.

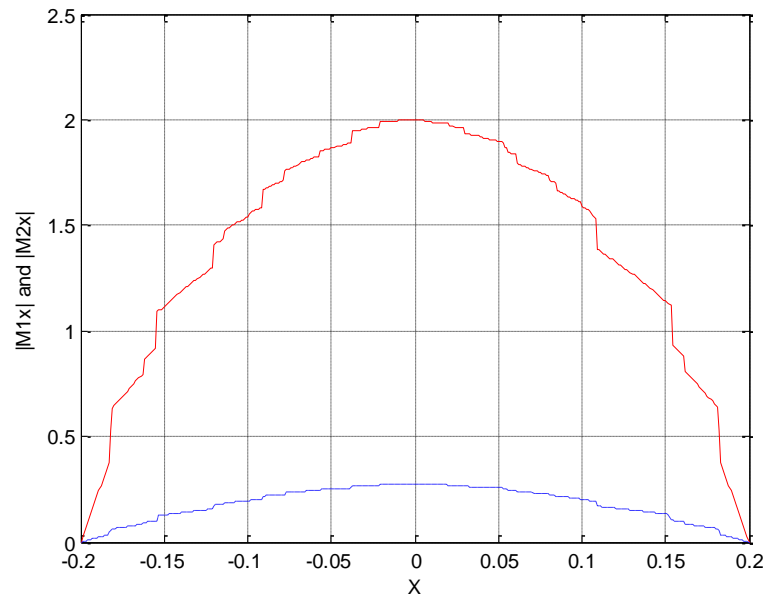


Fig. 3.27 Magnetic current on top aperture (solid line) and on bottom aperture (dashed line) along the x -axis for the problem in Fig. 3.26.

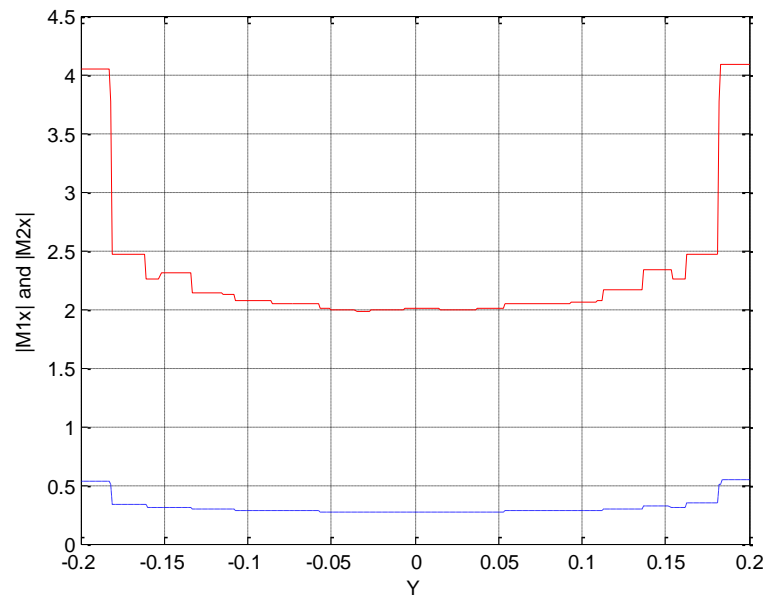


Fig. 3.28 Magnetic current on top aperture (solid line) and on bottom aperture (dashed line) along the y -axis for the problem in Fig. 3.26.

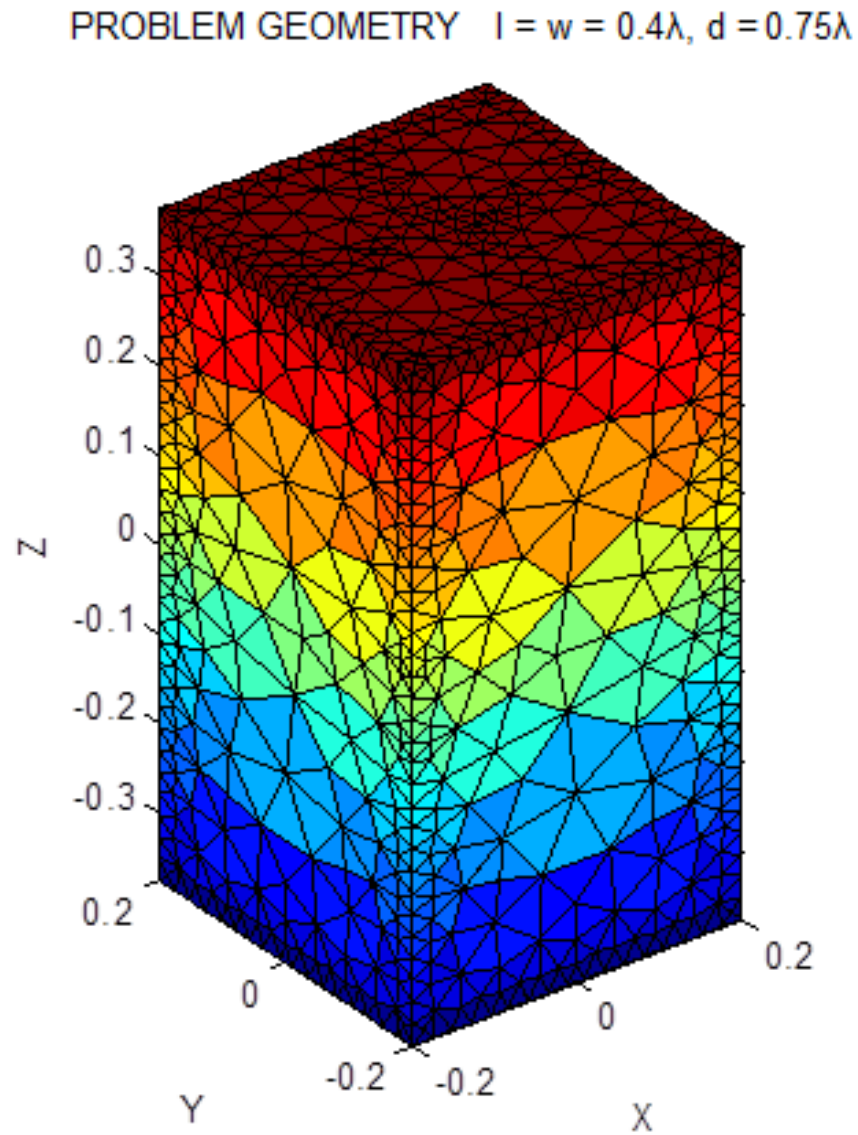


Fig. 3.29 Triangular meshing of the problem with square apertures (0.4λ -by- 0.4λ) on top and bottom; conductor thickness $d = 0.75\lambda$, $\epsilon_a = \epsilon_b = \epsilon_c = \epsilon_0$, $\mu_a = \mu_b = \mu_c = \mu_0$, $\vec{\mathbf{E}}^{\text{inc}} = \bar{\mathbf{y}}e^{jkz}$.

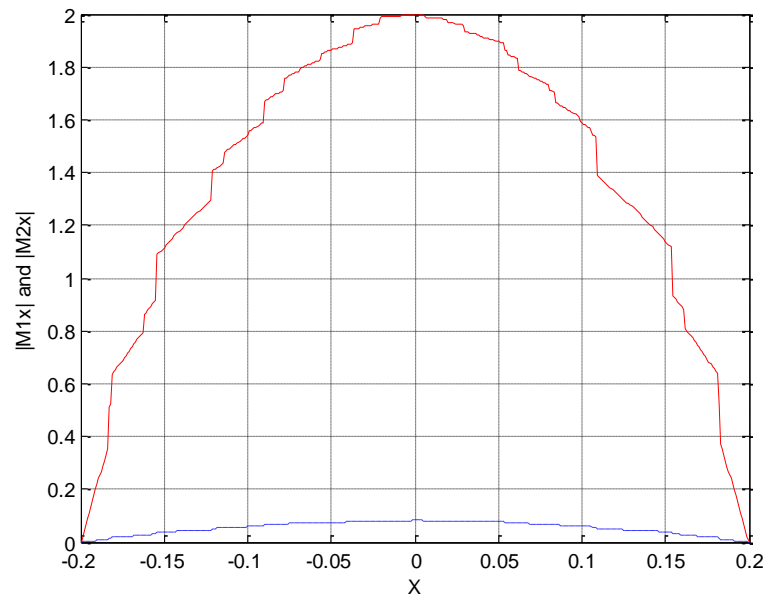


Fig. 3.30 Magnetic current on top aperture (solid line) and on bottom aperture (dashed line) along the x -axis for the problem in Fig. 3.29.

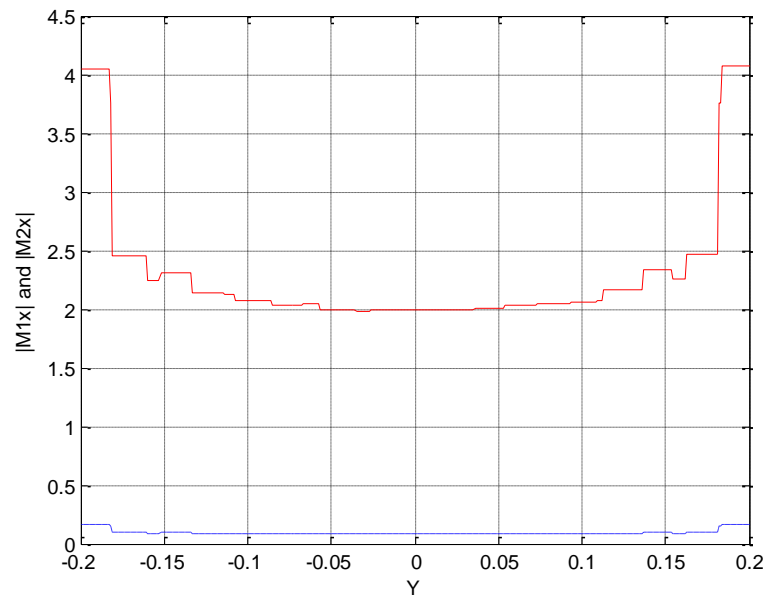


Fig. 3.31 Magnetic current on top aperture (solid line) and on bottom aperture (dashed line) along the y -axis for the problem in Fig. 3.29.

As seen from the magnetic current plots, increasing the conductor thickness reduces the magnetic current on the bottom aperture and therefore reduces the tangential electric field on the bottom aperture. Reduction of the tangential electric field on bottom aperture is generally accompanied by reduction of the transmission coefficient.

3.5 Results for Circular Apertures with a Conic Cavity

To prove the versatility of the method, a conic cavity in a thick conductor ($d = 0.5\lambda$) with circular apertures on top and bottom with radii of $R = 0.25\lambda$ and $r = 0.125\lambda$ respectively is analyzed. The problem geometry is shown in Fig 3.32.

The top and bottom magnetic currents along x and y axes are given in Fig. 3.33 and Fig. 3.34. RCS and transmission coefficients plots are shown in Fig. 3.35 and Fig.3.36.

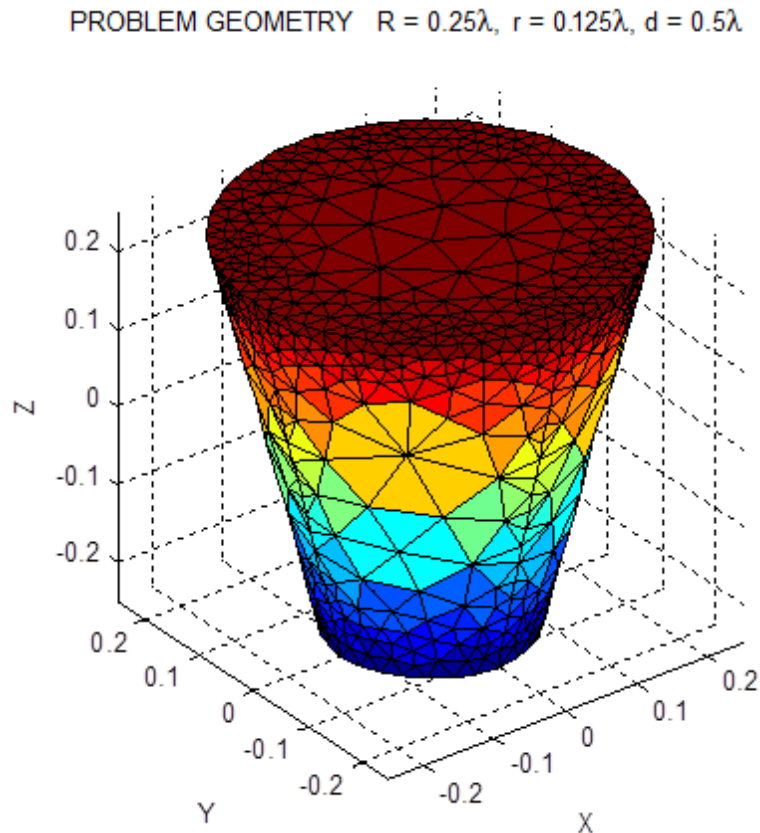


Fig. 3.32 Circular apertures with a conic cavity, $\vec{\mathbf{E}}^{\text{inc}} = \vec{\mathbf{y}}e^{jkz}$.

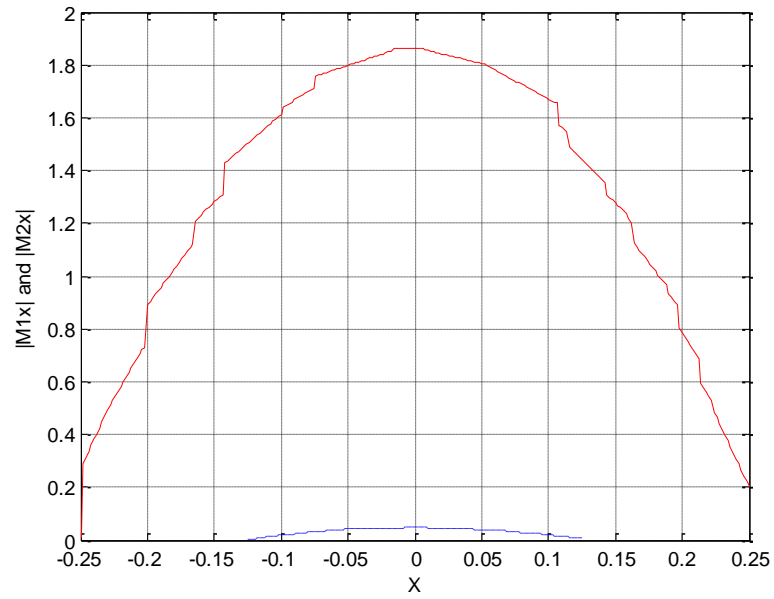


Fig. 3.33 Magnetic current on top aperture (solid line) and on bottom aperture (dashed line) along the x -axis for the problem in Fig 3.32.

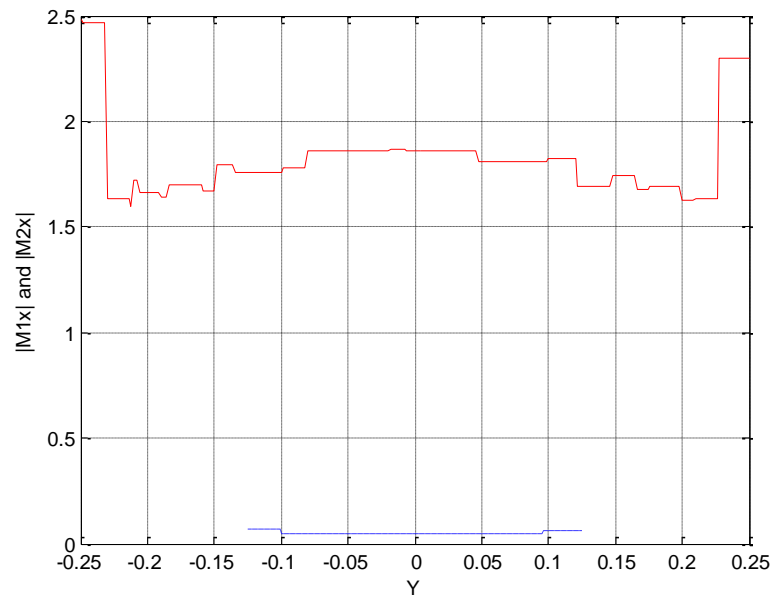


Fig. 3.34 Magnetic current on top aperture (solid line) and on bottom aperture (dashed line) along the y -axis for the problem in Fig 3.32.

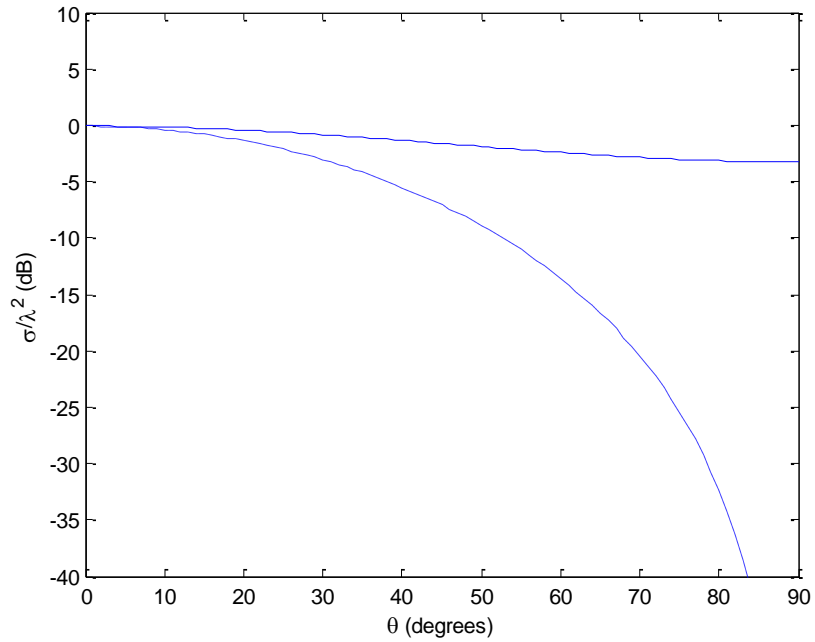


Fig. 3.35 Backscatter RCS of the structure in Fig 3.32 as a function of incidence angle in the $\phi = 0^\circ$ plane; solid line: $\vec{\mathbf{E}}^{\text{inc}}$ is phi polarized; dashed line: $\vec{\mathbf{E}}^{\text{inc}}$ is theta polarized.

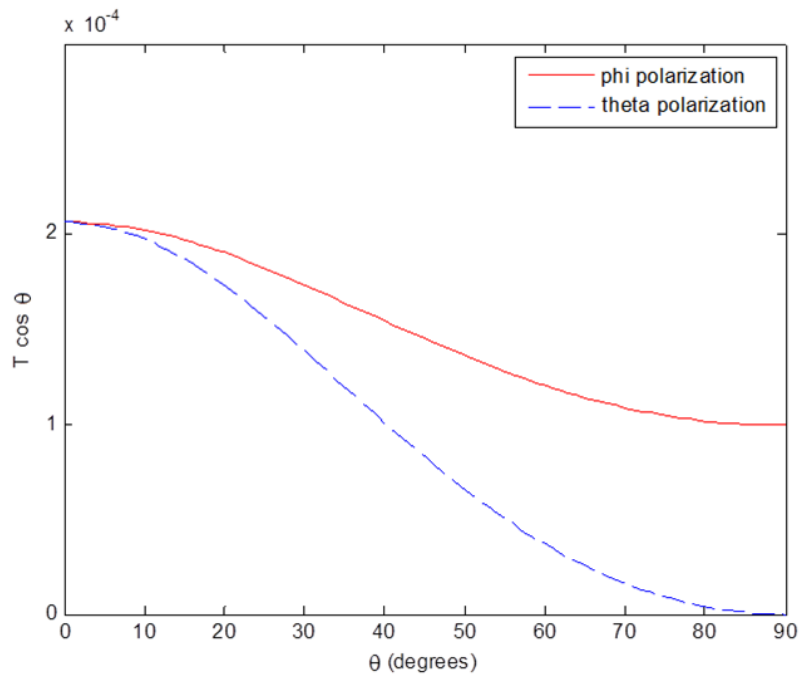


Fig. 3.36 Transmission coefficient plots of the structure in Fig 3.32 as a function of incidence angle in the $\phi = 0^\circ$ plane; solid line: $\vec{\mathbf{E}}^{\text{inc}}$ is phi polarized; dashed line: $\vec{\mathbf{E}}^{\text{inc}}$ is theta polarized.

3.6 Apertures in Ground Planes of Zero Thickness

The formulation developed in this dissertation is specifically for thick ground planes. However a zero thickness ground plane is the special case when the conductor thickness d goes to zero. The results from this dissertation should converge to the published results for apertures in thin ground planes. To check the validity of this claim, a circular aperture with a cylindrical cavity is analyzed. The results are compared to Chih Lin I [25]. The radius of the top and bottom circular apertures is $R = 0.25\lambda$. The incident field is $\vec{\mathbf{E}}^{\text{inc}} = \vec{\mathbf{y}}e^{jkz}$. The conductor thickness is initially taken as $d = 0.25\lambda$ and then reduced to 0.1λ and later to 0.01λ . The magnetic currents, RCS, and the transmission coefficient plots are provided for each of the three conductor thicknesses.

The triangulation of the circular aperture in a thin ground plane by [25] is given in Fig. 3.37. The transmission coefficient computed by [25] is given in Fig. 3.38. When computing the transmission coefficient, the incidence angle θ is varied from 0 degrees to 90 degrees. The incident electric field can be either theta polarized or phi polarized. Fig. 3.38 provides the results for both cases. Fig. 3.39 shows the problem geometry of a circular aperture with cylindrical cavity in $d = 0.25\lambda$ thick conducting plane. This problem is solved using the formulation developed in this dissertation. The corresponding plots are provided in Fig. 3.40–Fig. 3.43. Then, the conductor thickness is reduced to $d = 0.1\lambda$. The problem geometry is in Fig. 3.44. The computed results are in Fig. 3.45–Fig. 3.48. Finally, a very thin ($d = 0.01\lambda$) conducting plane is taken as shown in Fig. 3.49. The corresponding results are presented in Fig. 3.50–Fig. 3.53. The results of this final case are compared with Chih Lin I [25].

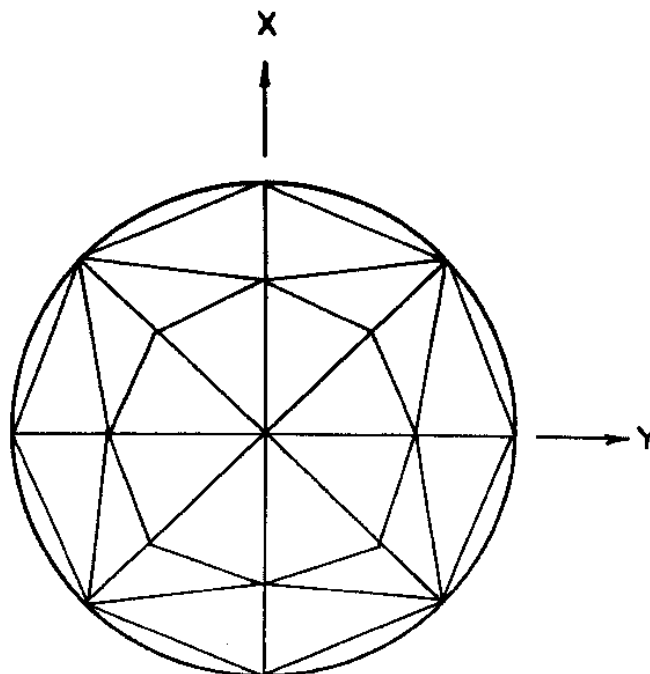


Fig. 3.37 Triangulation of the circular aperture ($R = 0.25\lambda$) in thin conducting plane, given by Chih Lin I [25].

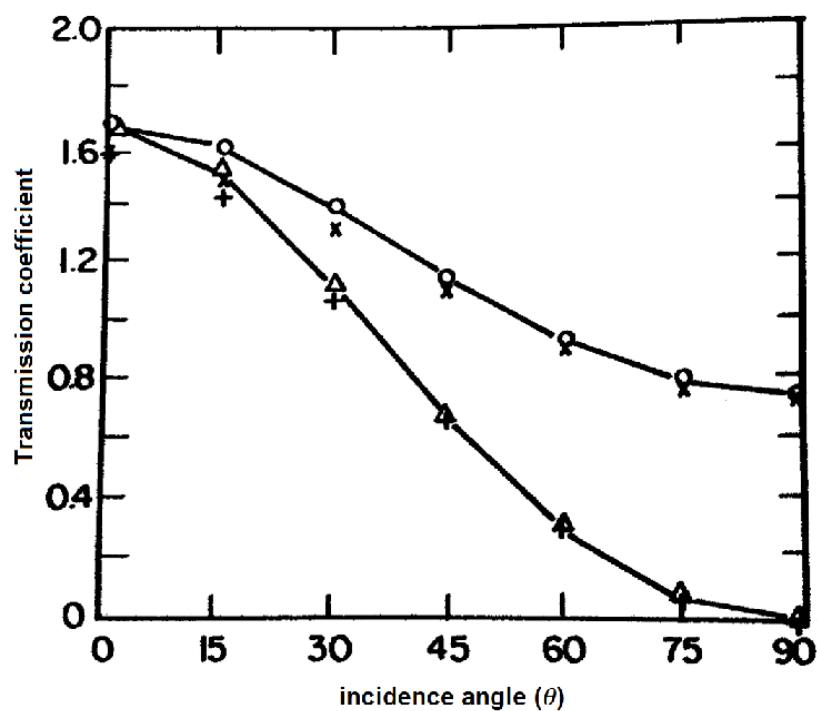


Fig. 3.38 Transmission coefficient for the circular aperture in Fig. 3.37 given by Chih Lin I [25]. x: computed result by [25] for phi polarization; +: computed result by [25] for theta polarization; o, Δ : corresponding data from another reference.

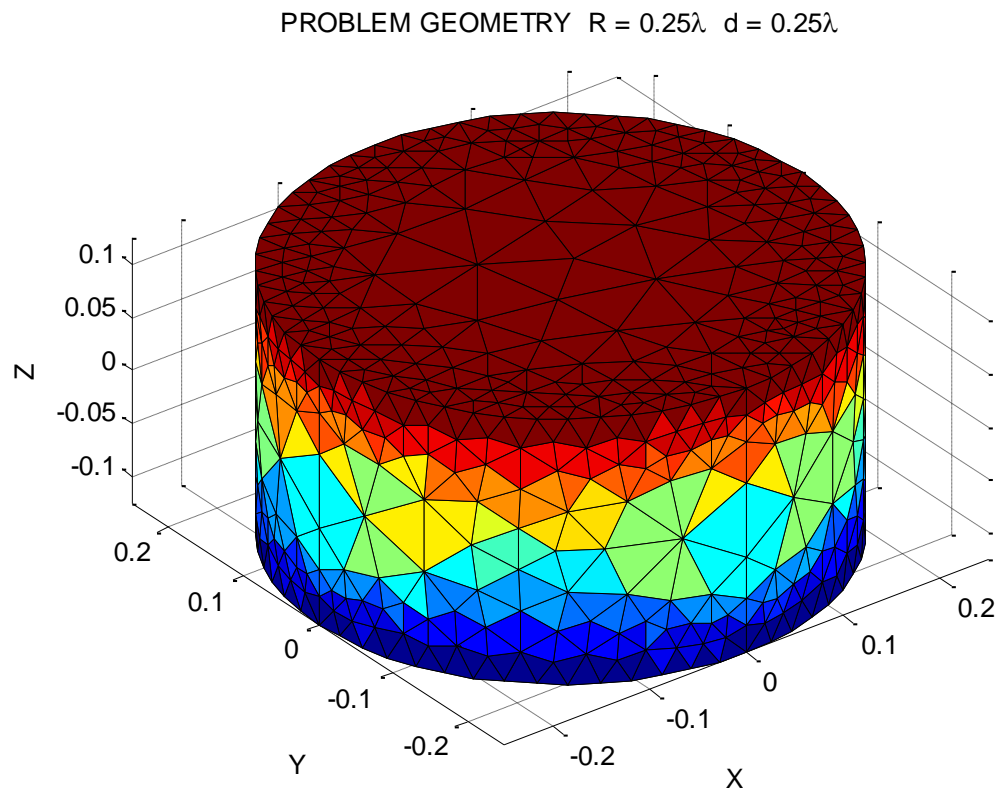


Fig. 3.39 Circular aperture with cylindrical cavity, $R = 0.25\lambda$, $d = 0.25\lambda$, $\vec{\mathbf{E}}^{\text{inc}} = \vec{\mathbf{y}}e^{jkz}$.

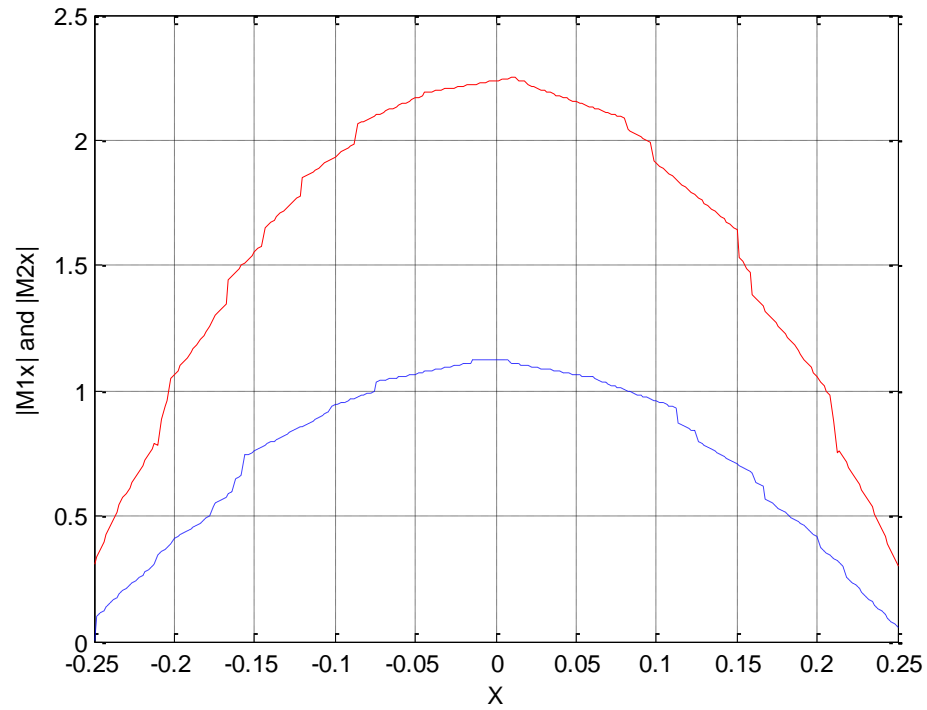


Fig. 3.40 Magnetic current on top aperture (solid line) and on bottom aperture (dashed line) along the x -axis for the problem in Fig. 3.39.

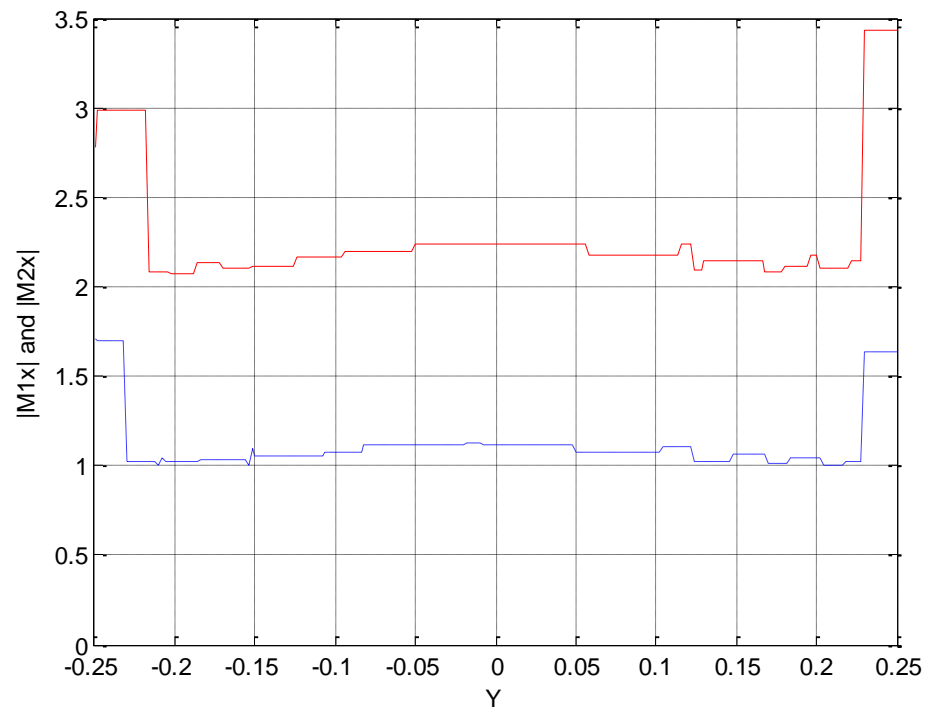


Fig. 3.41 Magnetic current on top aperture (solid line) and on bottom aperture (dashed line) along the y -axis for the problem in Fig. 3.39.

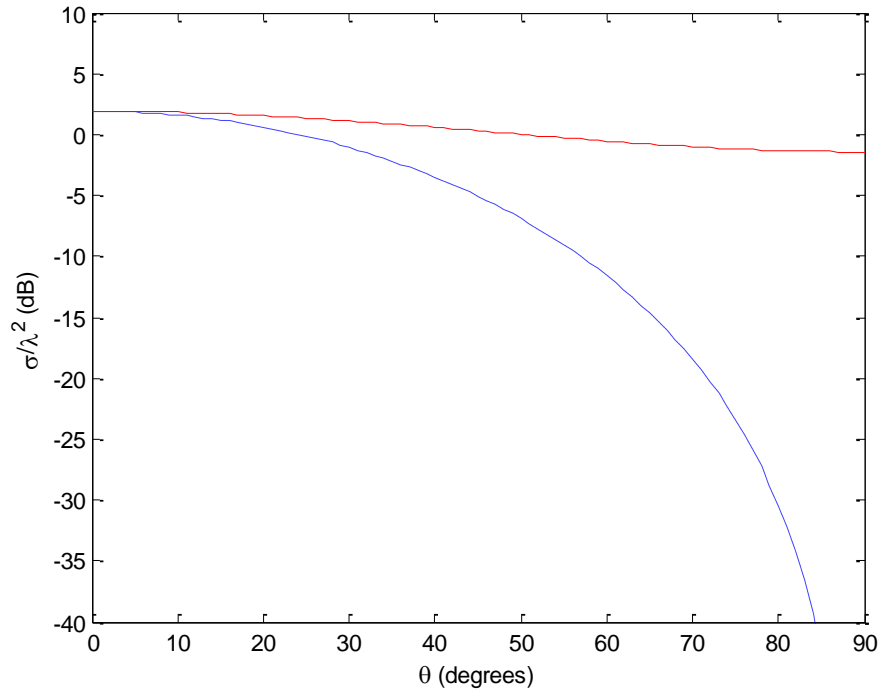


Fig. 3.42 Backscatter RCS of the structure in Fig. 3.39 as a function of incidence angle in the $\phi = 0^\circ$ plane; solid line: $\vec{\mathbf{E}}^{\text{inc}}$ is phi polarized; dashed line: $\vec{\mathbf{E}}^{\text{inc}}$ is theta polarized.

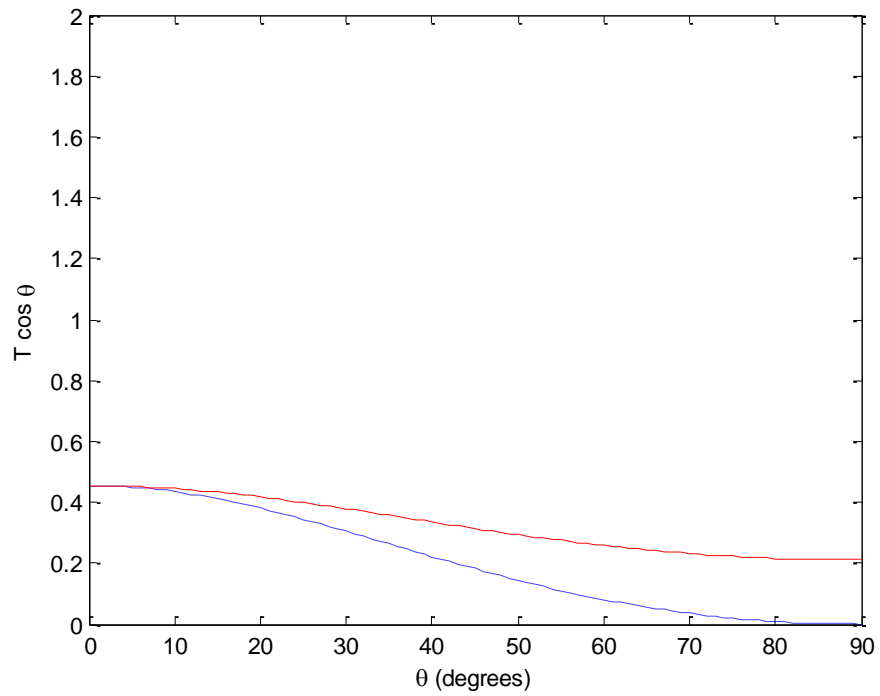


Fig. 3.43 Transmission coefficient plots of the structure in Fig. 3.39 as a function of incidence angle in the $\phi = 0^\circ$ plane; solid line: $\vec{\mathbf{E}}^{\text{inc}}$ is phi polarized; dashed line: $\vec{\mathbf{E}}^{\text{inc}}$ is theta polarized.

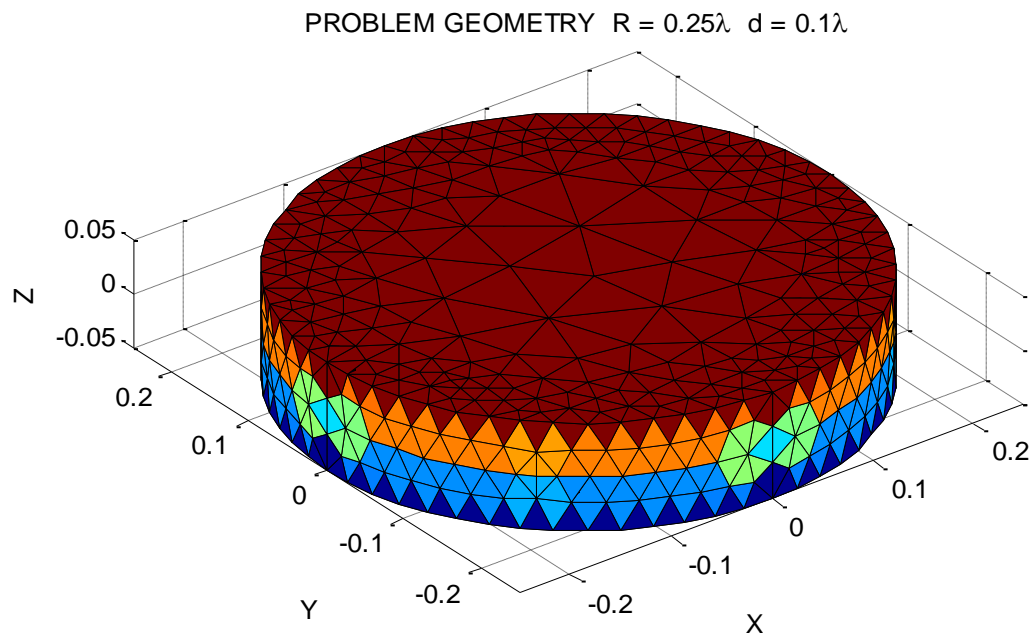


Fig. 3.44 Circular aperture with cylindrical cavity, $R = 0.25\lambda$, $d = 0.1\lambda$, $\vec{\mathbf{E}}^{\text{inc}} = \vec{\mathbf{y}}e^{jkz}$.

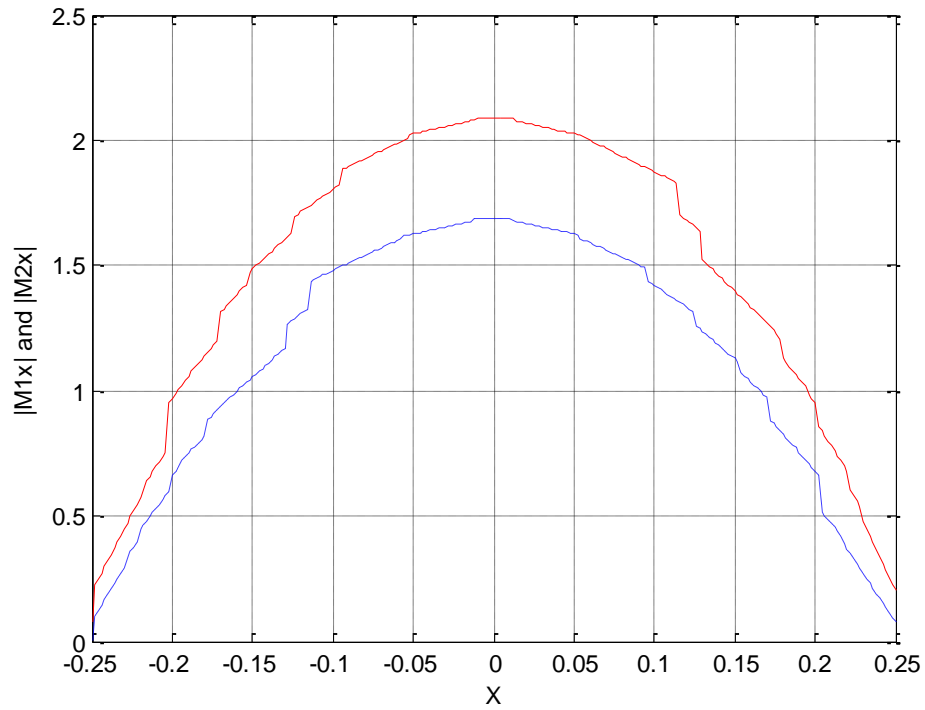


Fig. 3.45 Magnetic current on top aperture (solid line) and on bottom aperture (dashed line) along the x -axis for the problem in Fig. 3.44.

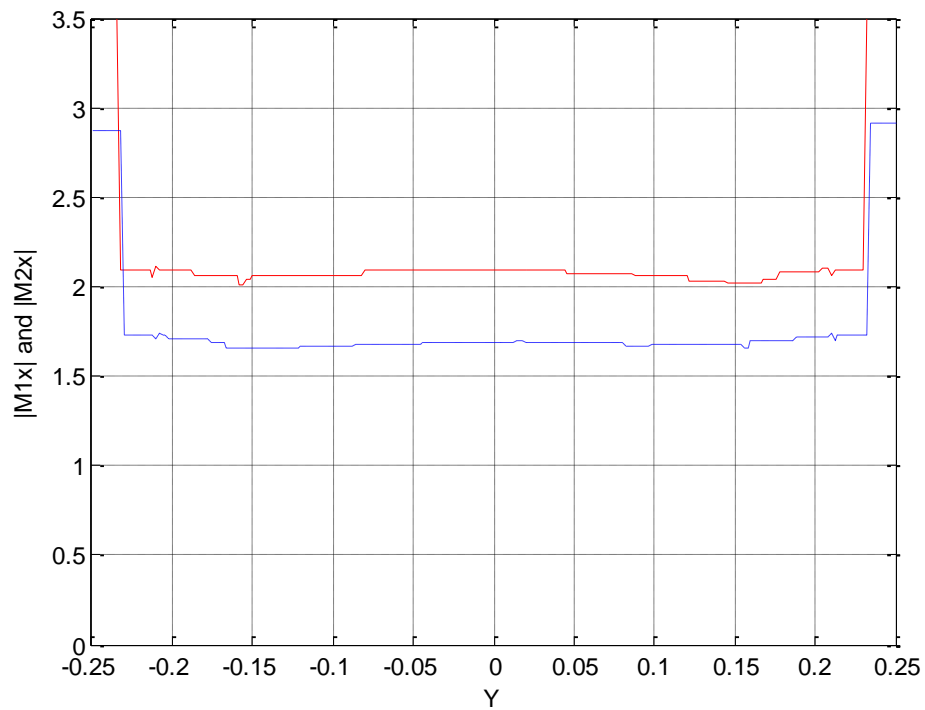


Fig. 3.46 Magnetic current on top aperture (solid line) and on bottom aperture (dashed line) along the y -axis for the problem in Fig. 3.44.

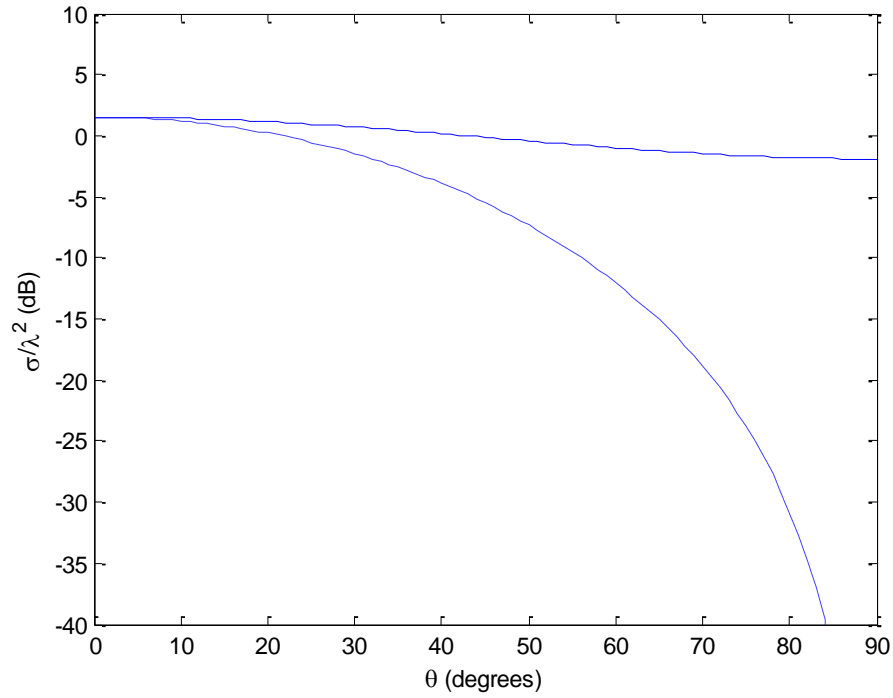


Fig. 3.47 Backscatter RCS of the structure in Fig. 3.44 as a function of incidence angle in the $\phi = 0^\circ$ plane; solid line: $\vec{\mathbf{E}}^{\text{inc}}$ is phi polarized; dashed line: $\vec{\mathbf{E}}^{\text{inc}}$ is theta polarized.

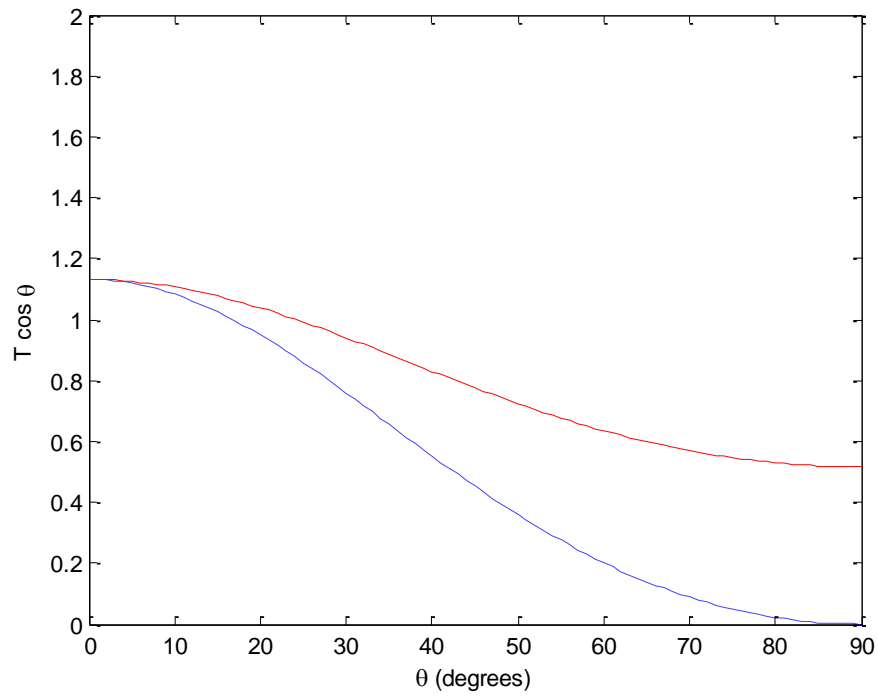


Fig. 3.48 Transmission coefficient plots of the structure in Fig. 3.44 as a function of incidence angle in the $\phi = 0^\circ$ plane; solid line: $\vec{\mathbf{E}}^{\text{inc}}$ is phi polarized; dashed line: $\vec{\mathbf{E}}^{\text{inc}}$ is theta polarized.

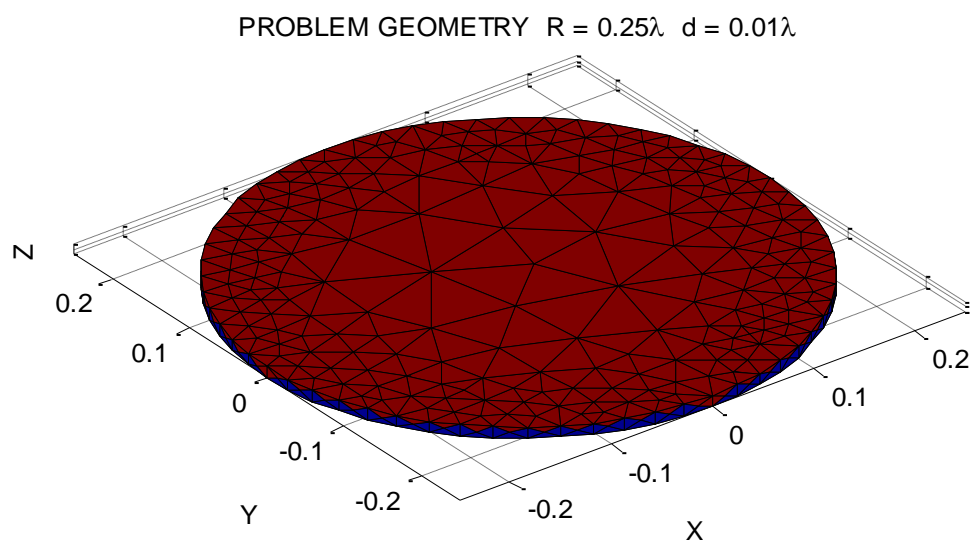


Fig. 3.49 Circular aperture with cylindrical cavity, $R = 0.25\lambda$, $d = 0.01\lambda$, $\vec{\mathbf{E}}^{\text{inc}} = \vec{\mathbf{y}}e^{jkz}$.

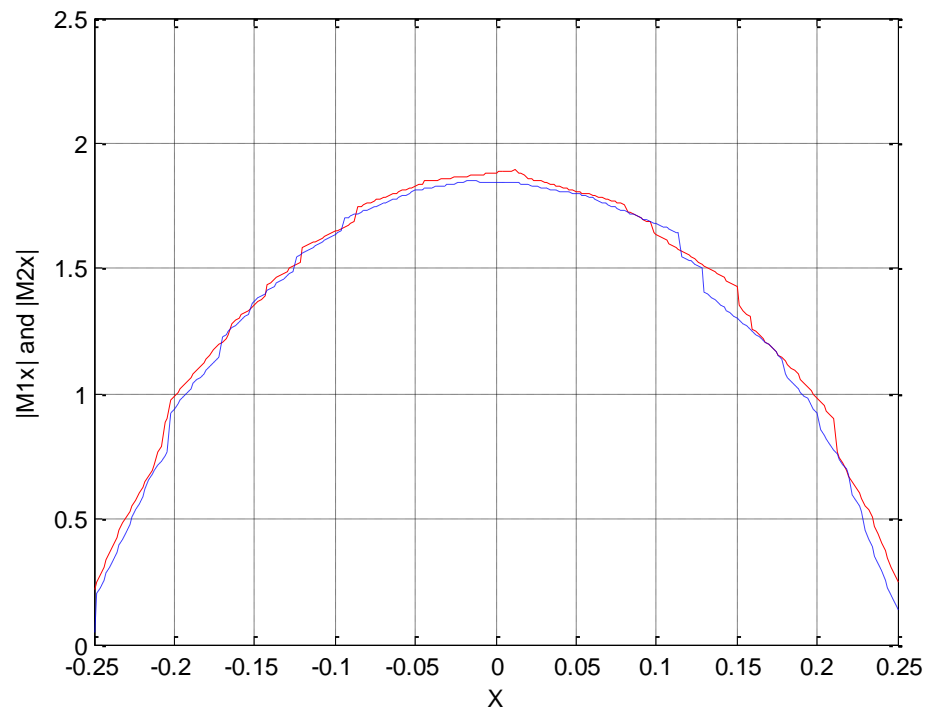


Fig. 3.50 Magnetic current on top aperture (solid line) and on bottom aperture (dashed line) along the x -axis for the problem in Fig. 3.49.

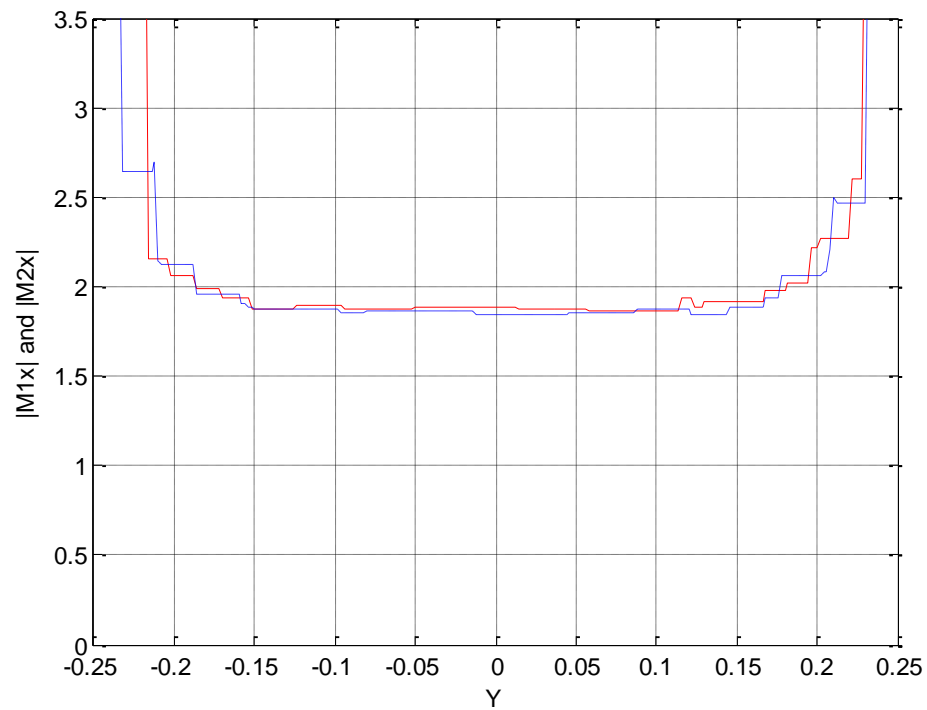


Fig. 3.51 Magnetic current on top aperture (solid line) and on bottom aperture (dashed line) along the y -axis for the problem in Fig. 3.49.

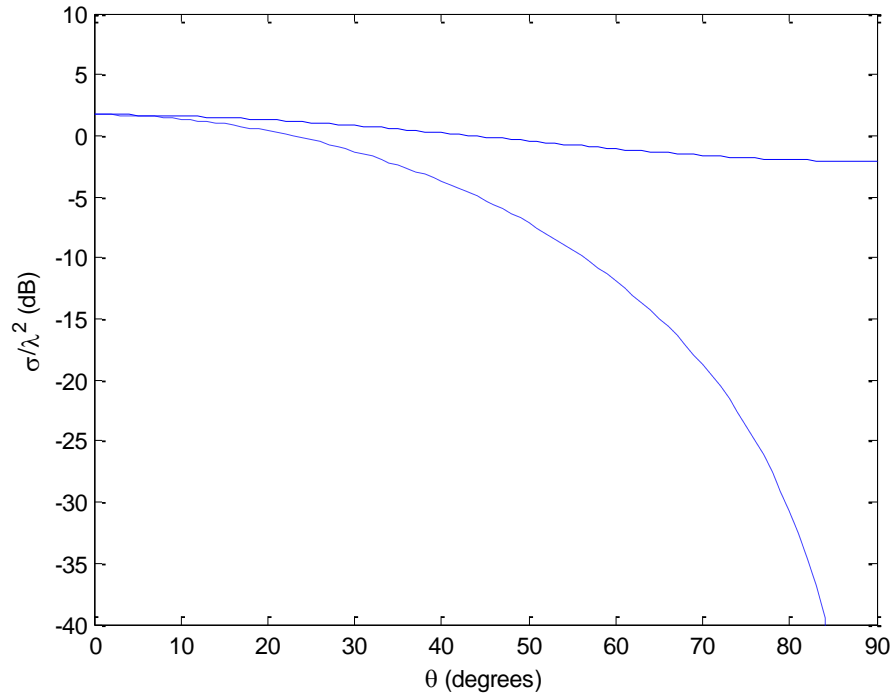


Fig. 3.52 Backscatter RCS of the structure in Fig. 3.49 as a function of incidence angle in the $\phi = 0^\circ$ plane; solid line: \vec{E}^{inc} is phi polarized; dashed line: \vec{E}^{inc} is theta polarized.

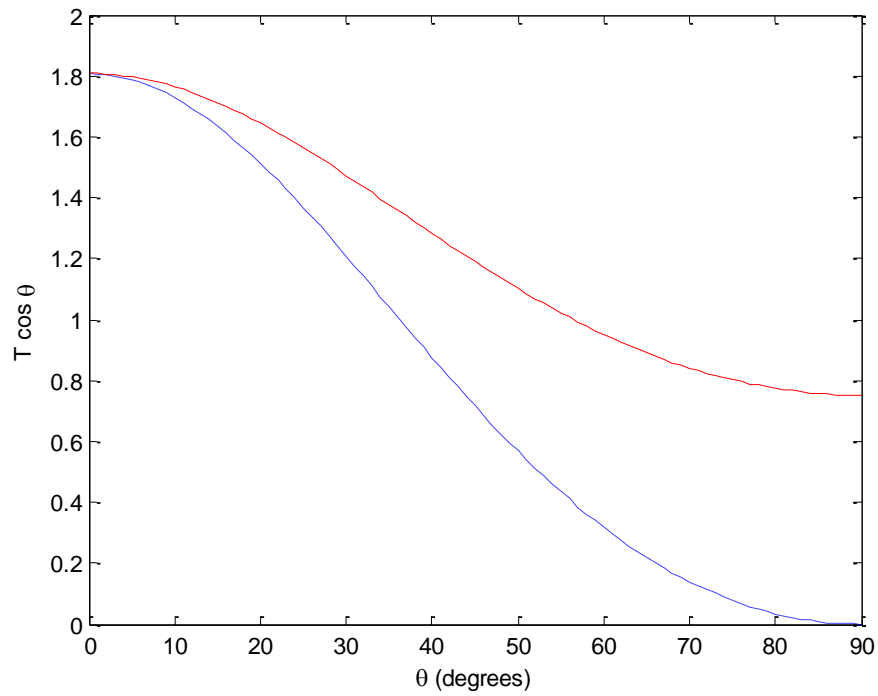


Fig. 3.53 Transmission coefficient plots of the structure in Fig. 3.49 as a function of incidence angle in the $\phi = 0^\circ$ plane; solid line: \vec{E}^{inc} is phi polarized; dashed line: \vec{E}^{inc} is theta polarized.

When Fig. 3.38 and Fig. 3.53 are compared, very good agreement is observed. If the thickness of the conducting plane is increased, the transmission coefficient becomes smaller as seen in Fig. 3.48 and Fig. 3.43. The thicker the conductor, the harder it is for the wave to penetrate through the aperture. Having the transmission coefficient larger than one in Fig. 3.48 and Fig. 3.53 may be unintuitive at first. The explanation for this is that, because it is calculated with the perforated ground plane present, the actual power passing through the top aperture could, because the incident power on the top aperture is calculated in the absence of the perforated ground plane, be more than the incident power on the top aperture. Therefore the transmitted power could be more than the incident power on the top aperture; hence the transmission coefficient could be larger than one.

The backscattering RCS in Fig. 3.42, Fig. 3.47, and Fig. 3.52 doesn't change much. This is expected because backscatter RCS depends on the magnetic current on the top aperture.

3.7 Effect of Meshing on Convergence

The results presented so far are obtained when the structure being analyzed is meshed with the refined triangular meshing scheme. The refined meshing generates triangles in such a way that the triangles closer to the boundaries of the apertures become smaller than the triangles further from the edges. As a result of this scheme, edge behavior of the current is more correctly captured. The current changes rapidly closer to the edges of the apertures and having smaller triangles closer to the edges helps to observe that change.

Another parameter of the meshing is the number of triangles. Due to limited computer resources, the number of triangles cannot be infinite. When running MATLAB

on a desktop computer with Intel Core2 2.4 GHz CPU and 4 GB memory, the limit on the number of triangles in a meshing is around 2000. Using that many triangles causes the moment matrix size to be around 5000 x 5000. The question then is how the number of triangles affects the convergence of numerical results to the solution.

In this section, the square aperture problem of Section 3.1 is going to be re-analyzed. The sizes of the top and bottom apertures are $l = w = 0.4\lambda$ and the conductor thickness is $d = 0.25\lambda$. The top aperture is illuminated by a plane wave $\vec{\mathbf{E}}^{\text{inc}} = \vec{\mathbf{y}}e^{jkz}$. The magnetic currents on the top and bottom apertures, RCS, and transmission coefficient plots will be presented when the problem geometry is meshed with 500, 1000, and 2000 triangles. Also results will be shown for each case when the refinement process is applied to the triangles closer to the edges.

Fig. 3.54–Fig. 3.56 show the meshing of the geometry with 500, 1000, and 2000 triangles respectively. The corresponding results are provided in Fig. 3.57–Fig. 3.64. In these figures, the results are plotted for each number of triangles so that the comparison is easier between varying levels of meshing. Fig. 3.65 and Fig. 3.66 show the meshing with 500 and 2000 triangles respectively with refinement applied to the edge triangles. The results are provided in Fig. 3.67–Fig. 3.74 for meshes with 500 and 2000 triangles with and without the refinement applied.

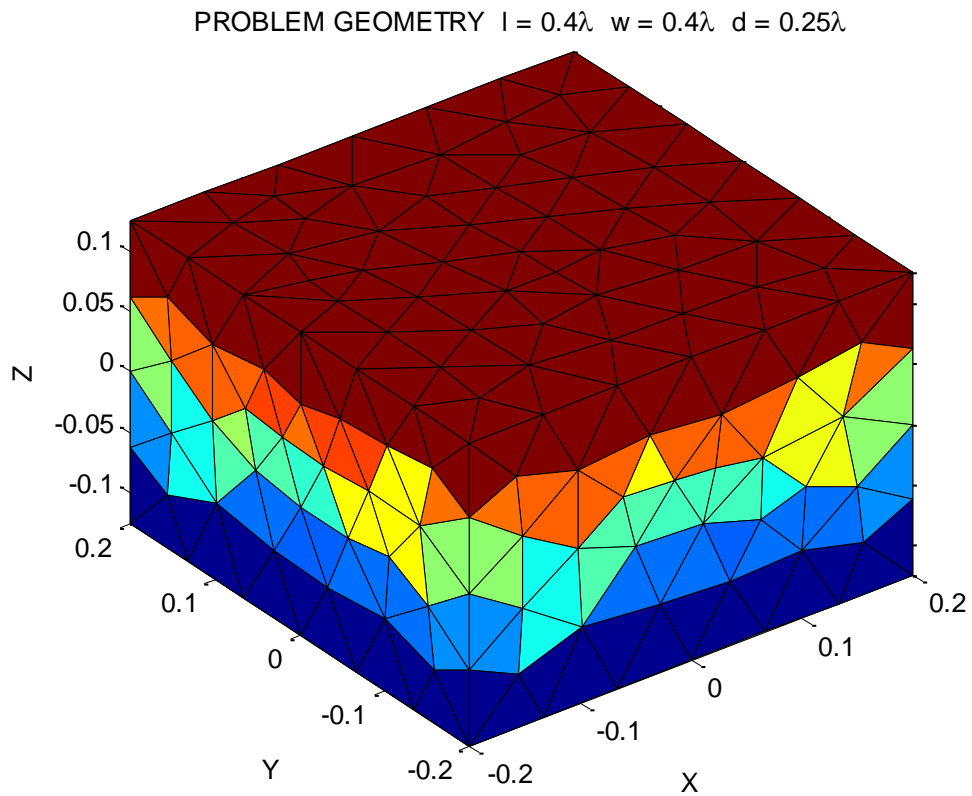


Fig. 3.54 The problem of square apertures (0.4λ -by- 0.4λ) with $d = 0.25\lambda$ is meshed with 500

triangles, $\epsilon_a = \epsilon_b = \epsilon_c = \epsilon_0$, $\mu_a = \mu_b = \mu_c = \mu_0$, $\vec{\mathbf{E}}^{\text{inc}} = \vec{\mathbf{y}}e^{jkz}$.

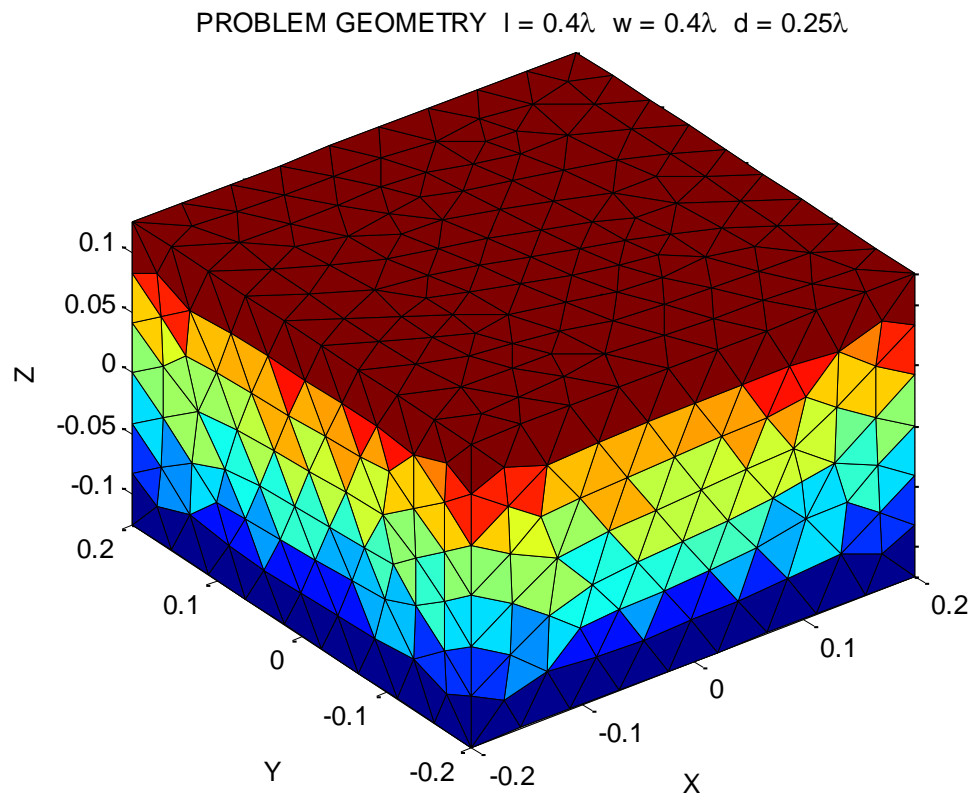


Fig. 3.55 The problem of square apertures (0.4λ -by- 0.4λ) with $d = 0.25\lambda$ is meshed with 1000

triangles, $\epsilon_a = \epsilon_b = \epsilon_c = \epsilon_0$, $\mu_a = \mu_b = \mu_c = \mu_0$, $\vec{\mathbf{E}}^{\text{inc}} = \vec{\mathbf{y}}e^{jkz}$.

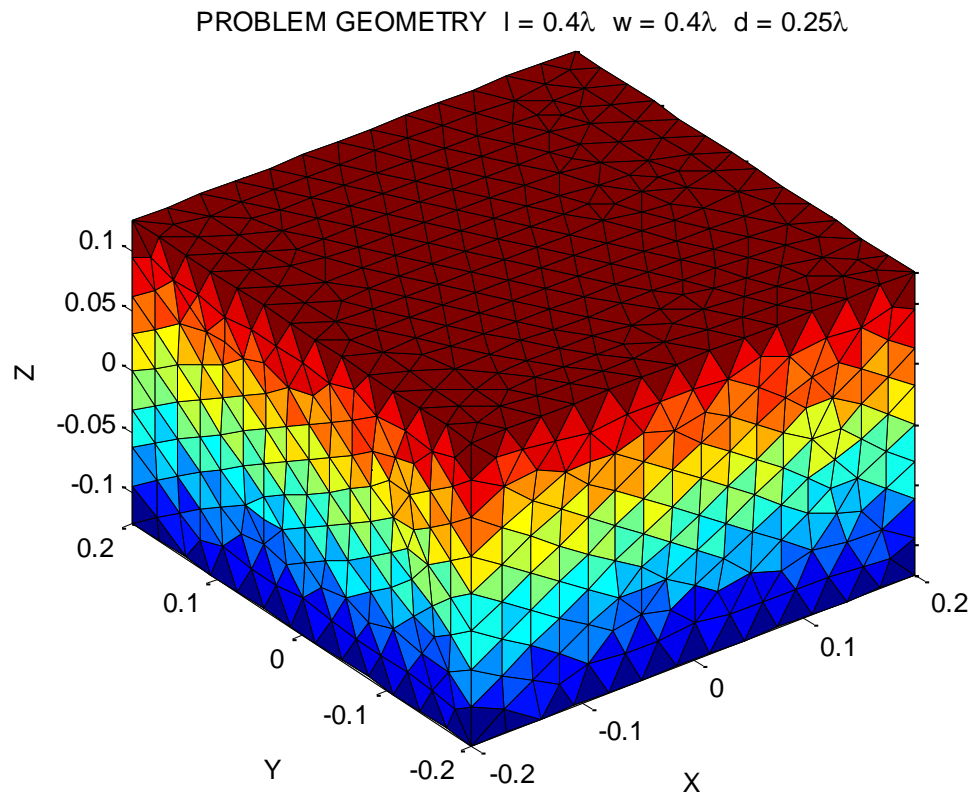


Fig. 3.56 The problem of square apertures (0.4λ -by- 0.4λ) with $d = 0.25\lambda$ is meshed with 2000

triangles, $\varepsilon_a = \varepsilon_b = \varepsilon_c = \varepsilon_0$, $\mu_a = \mu_b = \mu_c = \mu_0$, $\vec{\mathbf{E}}^{\text{inc}} = \vec{\mathbf{y}}e^{jkz}$.

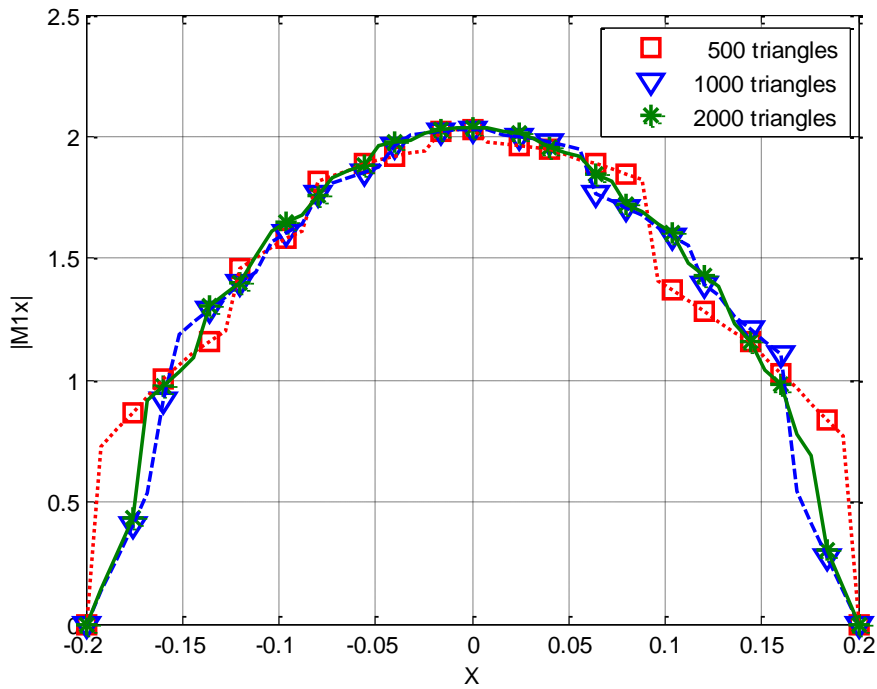


Fig. 3.57 Magnetic current on the top aperture along the x -axis when the meshing is done using 500, 1000, and 2000 triangles.

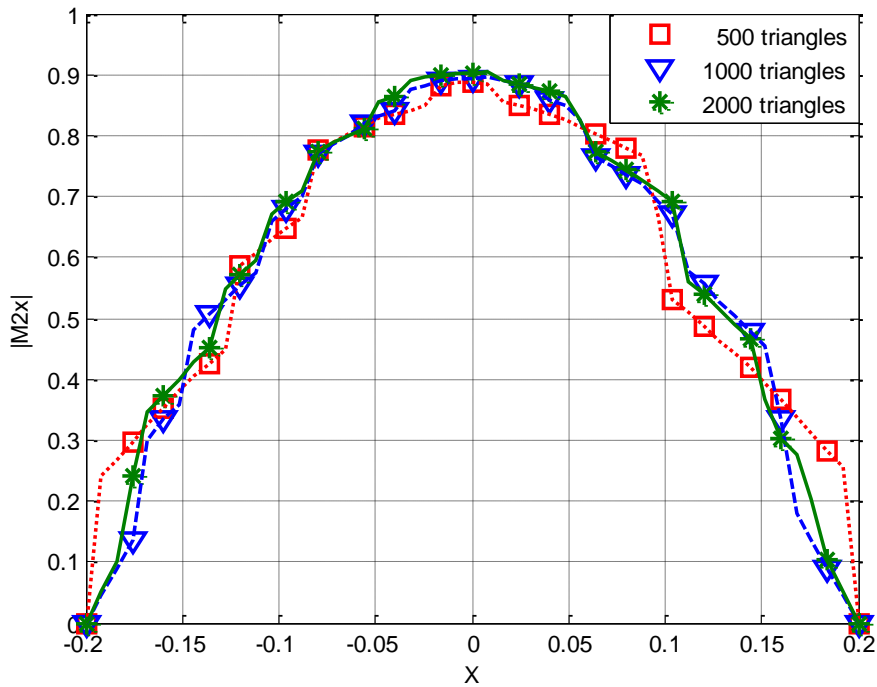


Fig. 3.58 Magnetic current on the bottom aperture along the x -axis when the meshing is done using 500, 1000, and 2000 triangles.

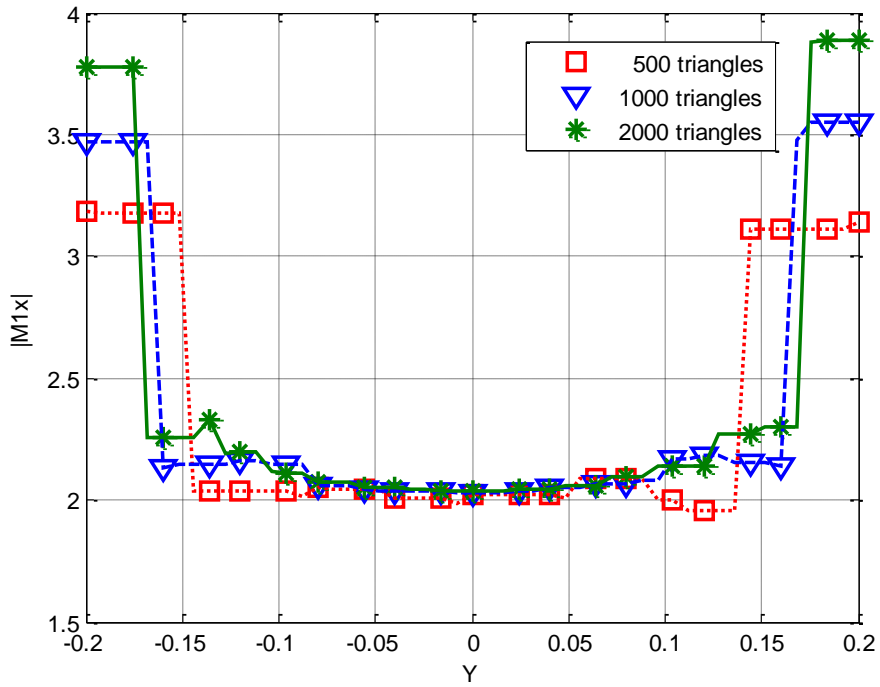


Fig. 3.59 Magnetic current on the top aperture along the y -axis when the meshing is done using 500, 1000, and 2000 triangles.

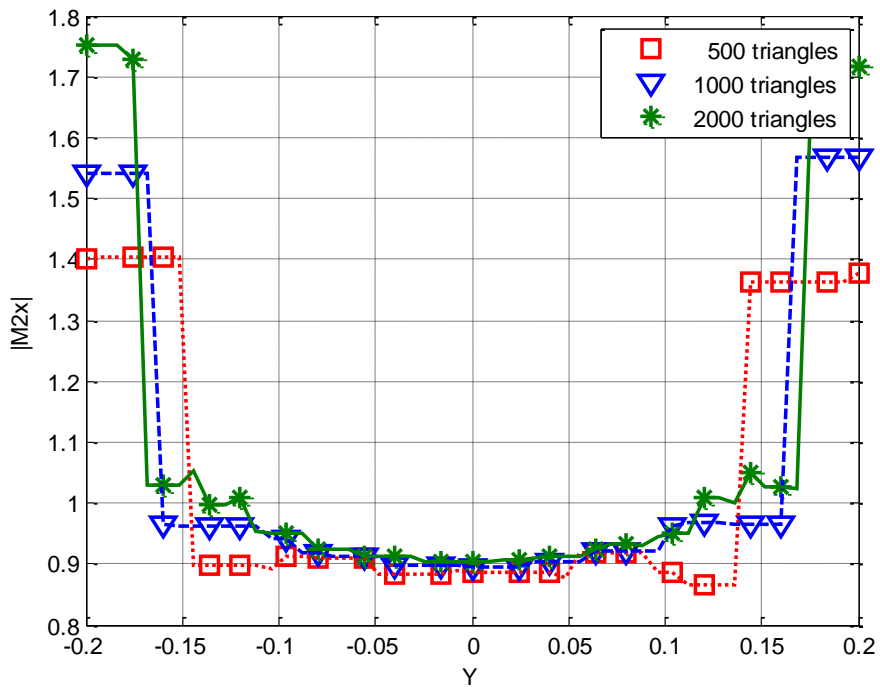


Fig. 3.60 Magnetic current on the bottom aperture along the y -axis when the meshing is done using 500, 1000, and 2000 triangles.

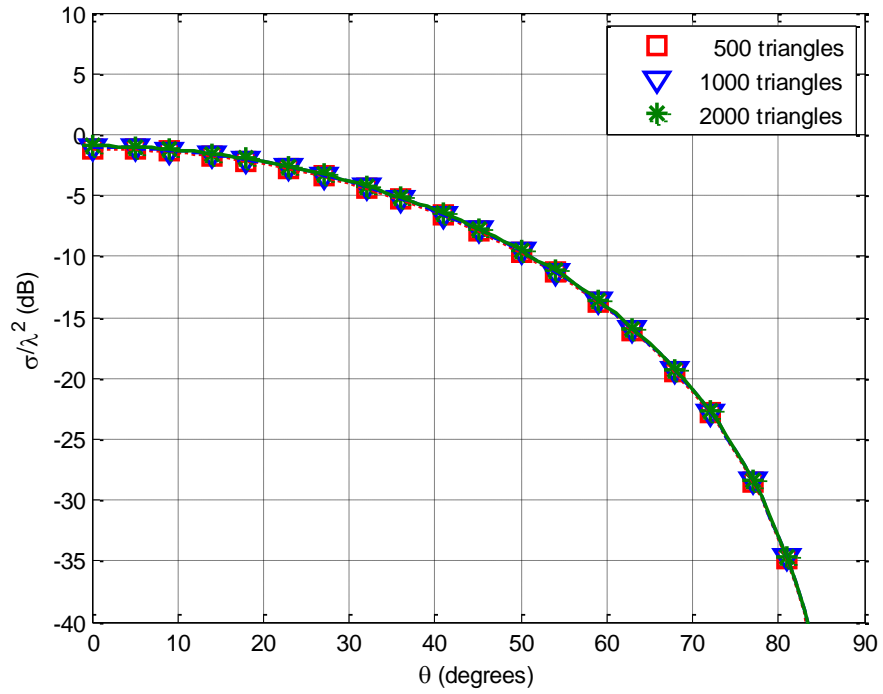


Fig. 3.61 Backscatter RCS in the $\phi = 0^\circ$ plane when \vec{E}^{inc} is theta polarized. The meshing is done using 500, 1000 and 2000 triangles.

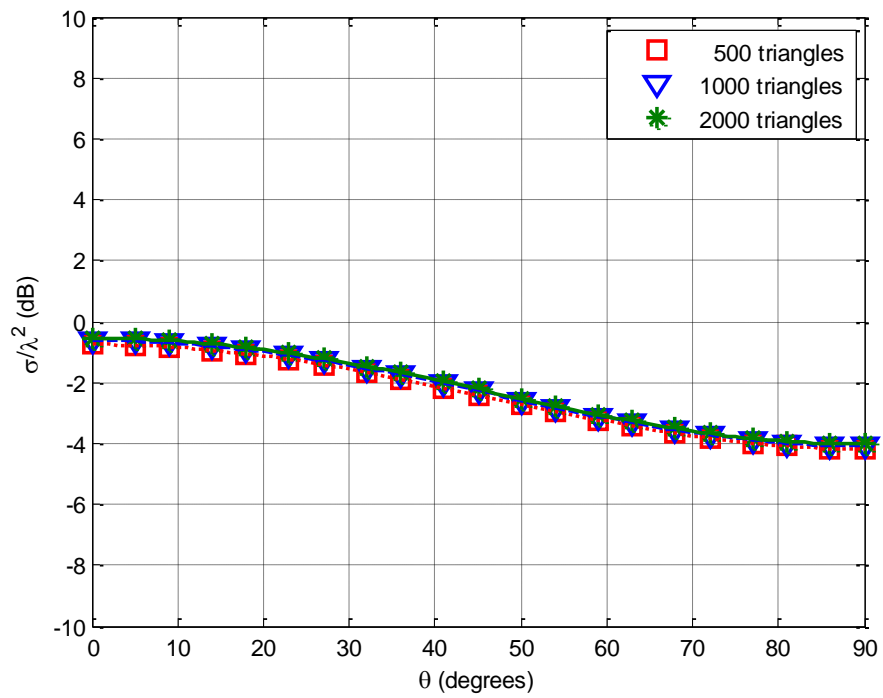


Fig. 3.62 Backscatter RCS in the $\phi = 0^\circ$ plane when \vec{E}^{inc} is phi polarized. The meshing is done using 500, 1000 and 2000 triangles.

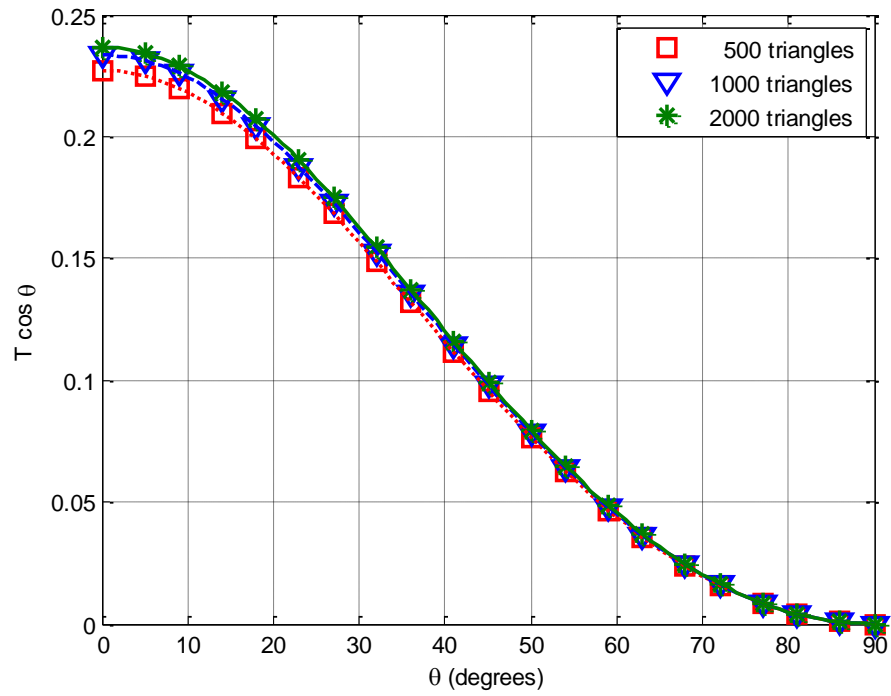


Fig. 3.63 Transmission coefficient plots in the $\phi = 0^\circ$ plane when $\vec{\mathbf{E}}^{\text{inc}}$ is theta polarized. The meshing is done using 500, 1000 and 2000 triangles.

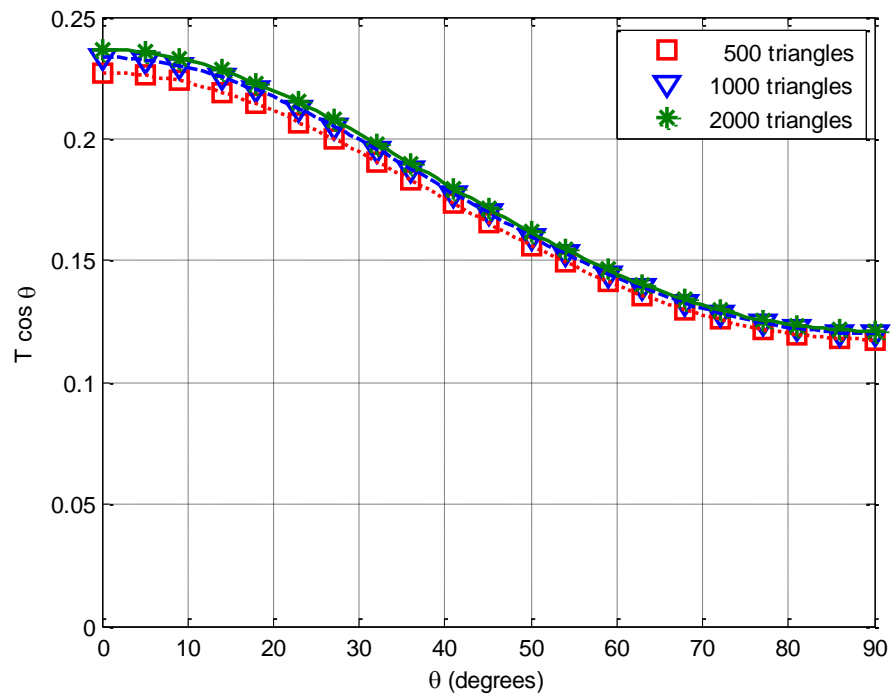


Fig. 3.64 Transmission coefficient plots in the $\phi = 0^\circ$ plane when $\vec{\mathbf{E}}^{\text{inc}}$ is phi polarized. The meshing is done using 500, 1000 and 2000 triangles.

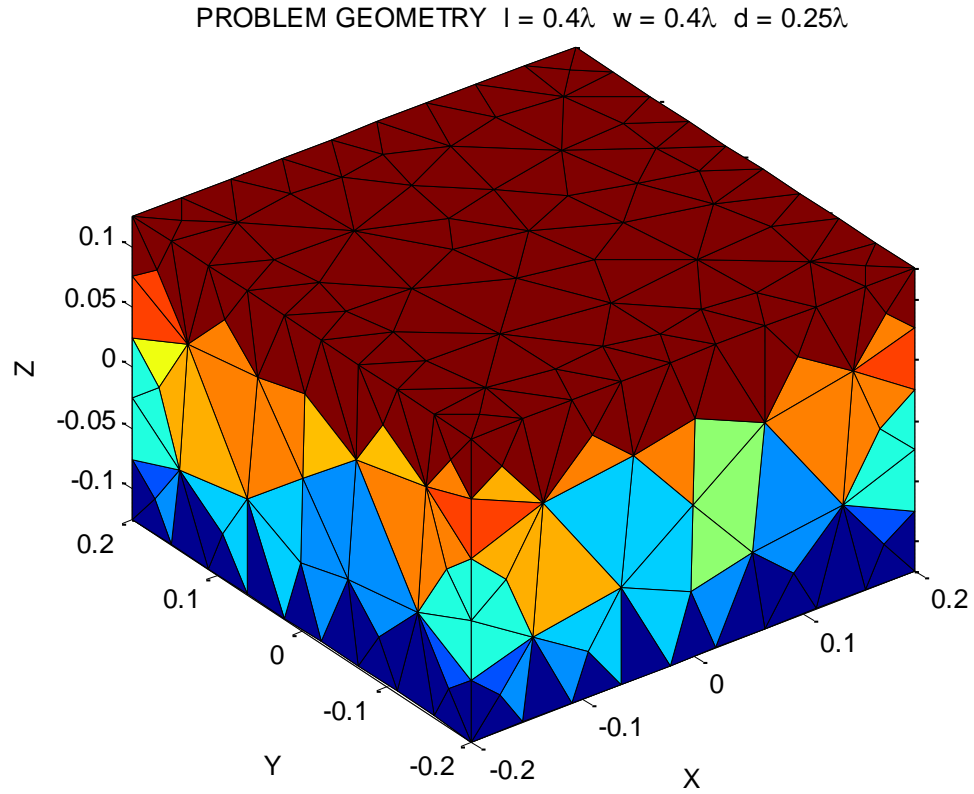


Fig. 3.65 The problem of square apertures (0.4λ -by- 0.4λ) with $d = 0.25\lambda$ is meshed with 500

refined triangles, $\epsilon_a = \epsilon_b = \epsilon_c = \epsilon_0$, $\mu_a = \mu_b = \mu_c = \mu_0$, $\vec{\mathbf{E}}^{\text{inc}} = \vec{\mathbf{y}}e^{jkz}$.

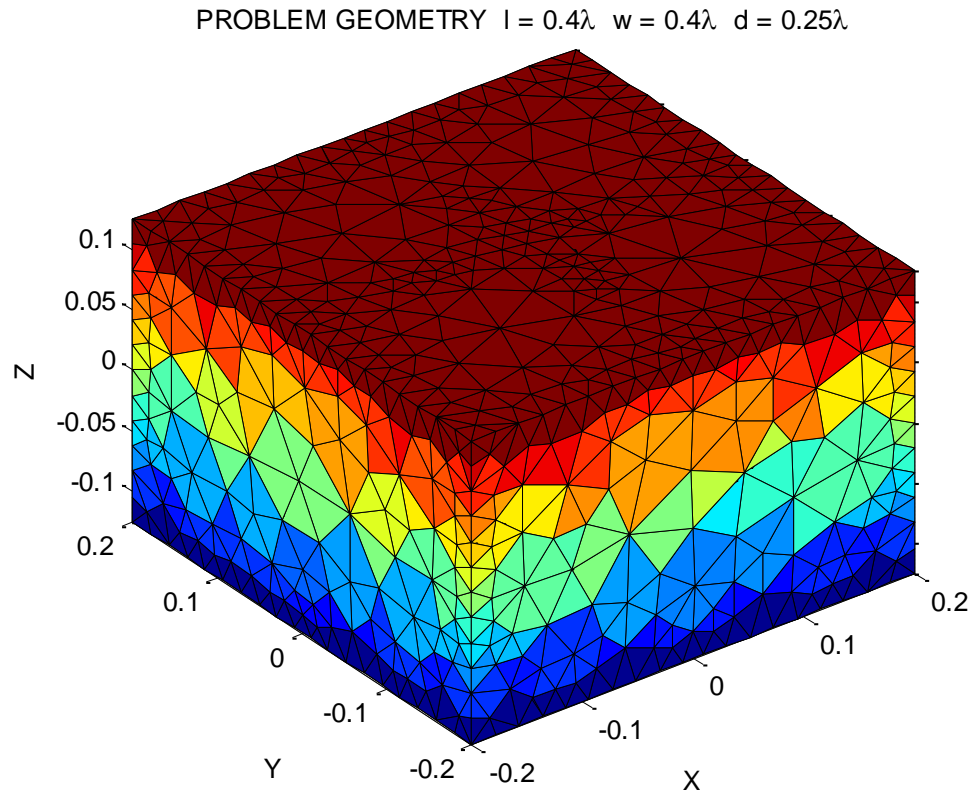


Fig. 3.66 The problem of square apertures (0.4λ -by- 0.4λ) with $d = 0.25\lambda$ is meshed with 2000

refined triangles, $\varepsilon_a = \varepsilon_b = \varepsilon_c = \varepsilon_0$, $\mu_a = \mu_b = \mu_c = \mu_0$, $\vec{\mathbf{E}}^{\text{inc}} = \vec{\mathbf{y}}e^{jkz}$.

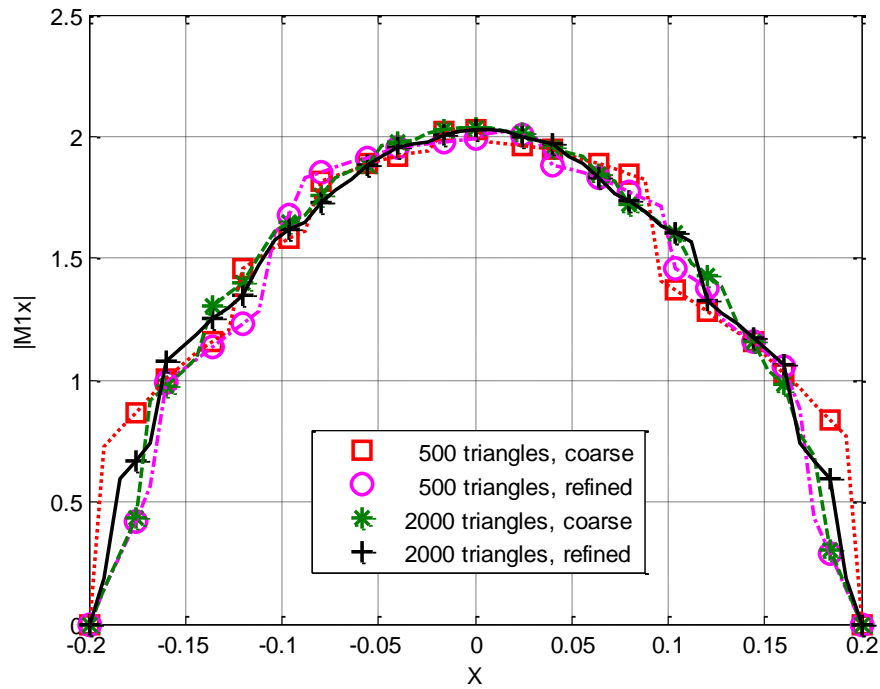


Fig. 3.67 Magnetic current on the top aperture along the x -axis when the meshing is done using 500 and 2000 triangles. Triangle refinement is applied.

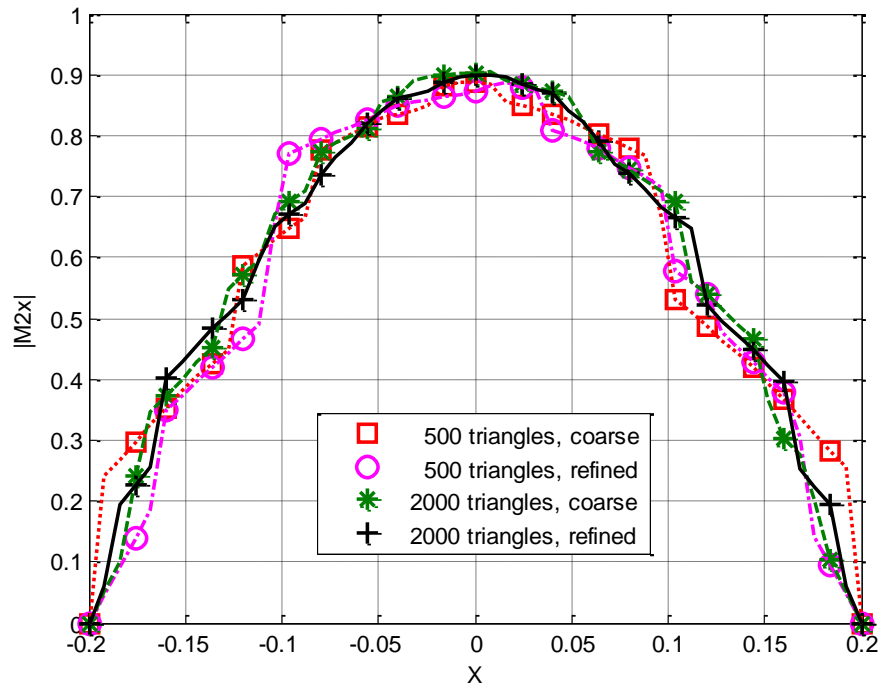


Fig. 3.68 Magnetic current on the bottom aperture along the x -axis when the meshing is done using 500 and 2000 triangles. Triangle refinement is applied.

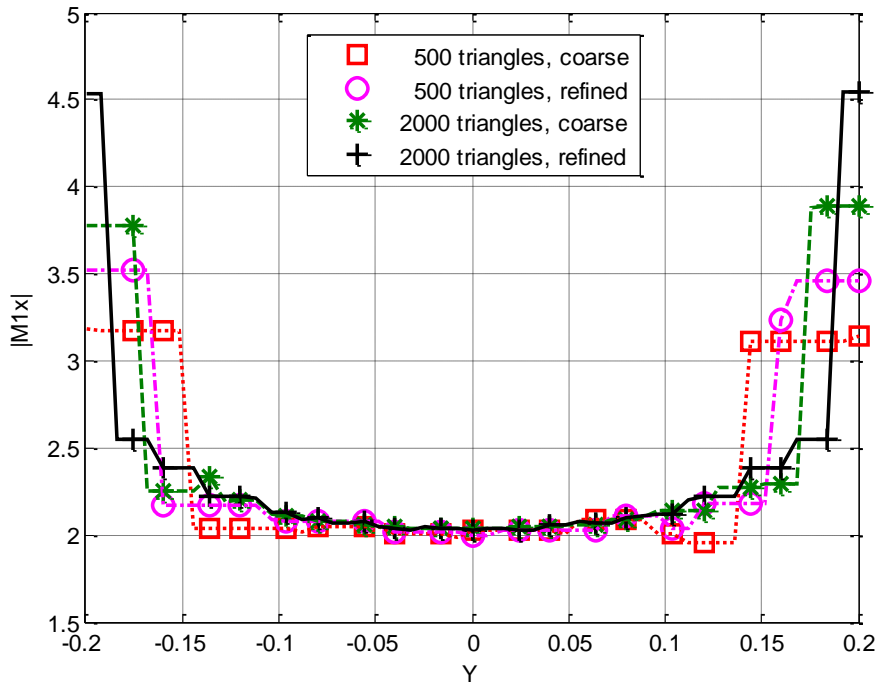


Fig. 3.69 Magnetic current on the top aperture along the y -axis when the meshing is done using 500 and 2000 triangles. Triangle refinement is applied.

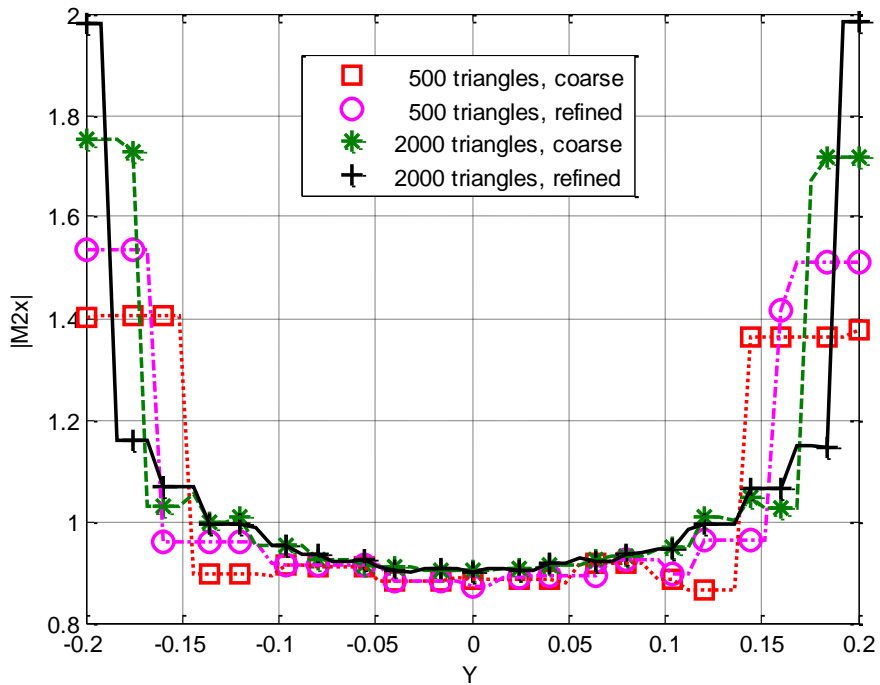


Fig. 3.70 Magnetic current on the bottom aperture along the y -axis when the meshing is done using 500 and 2000 triangles. Triangle refinement is applied.

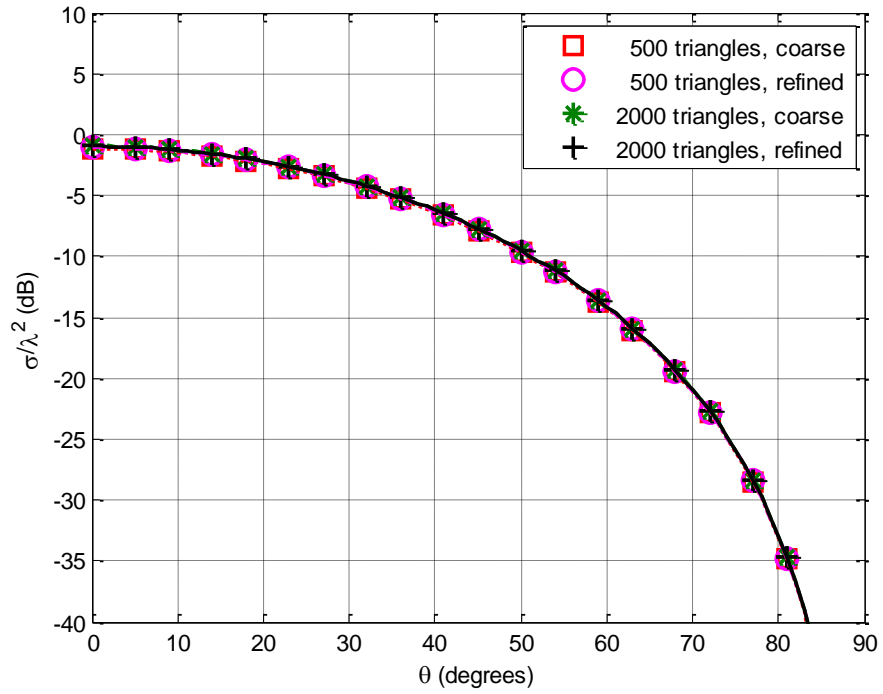


Fig. 3.71 Backscatter RCS in the $\phi = 0^\circ$ plane when \vec{E}^{inc} is theta polarized. The meshing is done using 500 and 2000 triangles. Triangle refinement is applied.

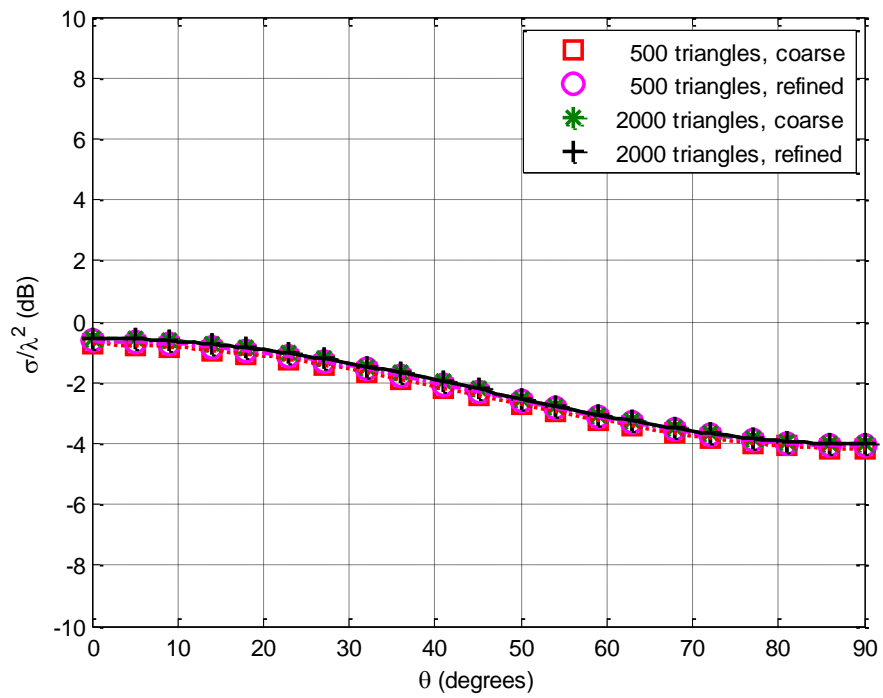


Fig. 3.72 Backscatter RCS in the $\phi = 0^\circ$ plane when \vec{E}^{inc} is phi polarized. The meshing is done using 500 and 2000 triangles. Triangle refinement is applied.

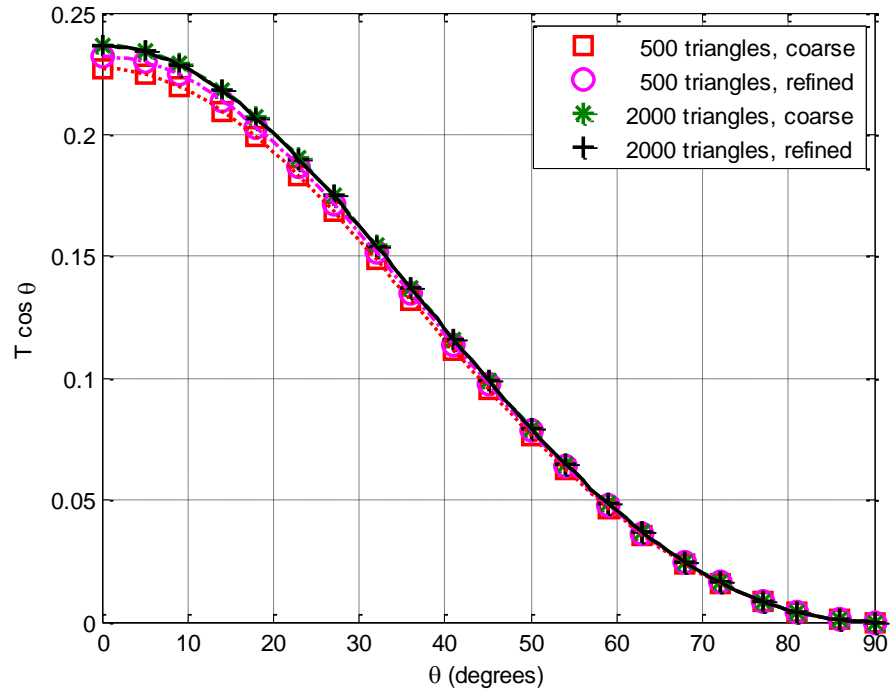


Fig. 3.73 Transmission coefficient plots in the $\phi = 0^\circ$ plane when $\vec{\mathbf{E}}^{\text{inc}}$ is theta polarized. The meshing is done using 500 and 2000 triangles. Triangle refinement is applied.

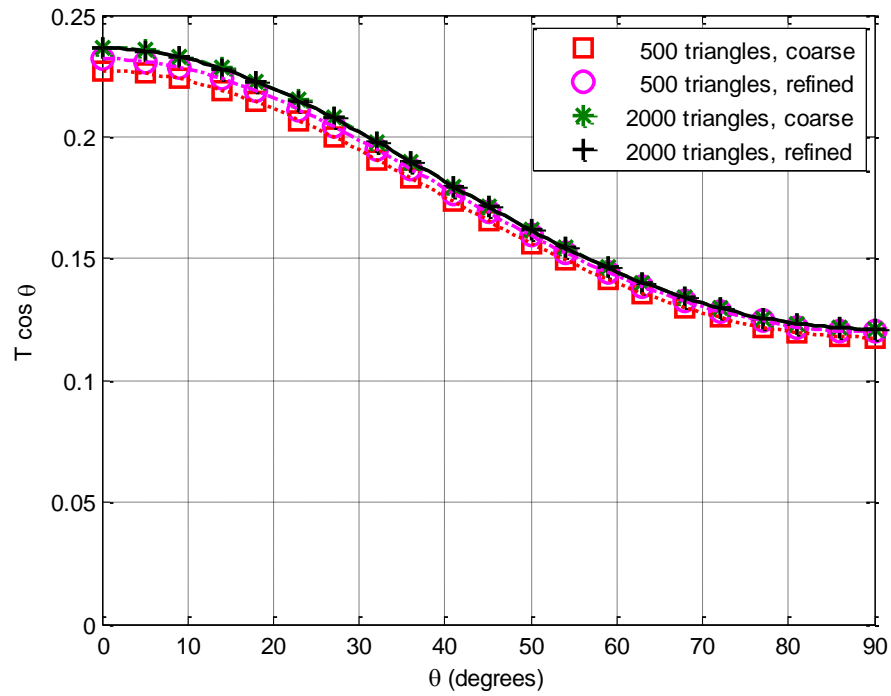


Fig. 3.74 Transmission coefficient plots in the $\phi = 0^\circ$ plane when $\vec{\mathbf{E}}^{\text{inc}}$ is phi polarized. The meshing is done using 500 and 2000 triangles. Triangle refinement is applied.

After checking the provided results, it is seen that the density of the meshing mostly affects the magnetic currents. Backscattering RCS and the transmission coefficient plots don't change much with varying number of triangles. That is because these parameters involve integrations over the sources and the integral of a quantity is generally smoother than the quantity. When the number of triangles in a mesh is increased, edge behavior is more accurately observed. Close to the center of the aperture, the currents don't vary much so good results can be obtained even with 500 triangles. It is found out that 500 triangles in this specific problem amounts to 15 triangles per wavelength. When the current on the edges is considered, having a mesh with 1000 triangles provides a noticeable improvement in accuracy. However, having 2000 triangles in a mesh doesn't add much improvement over having 1000 triangles. 1000 triangles in this problem means 22 triangles per wavelength and 2000 triangles means 32 triangles per wavelength. It is concluded that having 20 triangles per wavelength is enough to obtain good results; increasing the density of triangles doesn't justify the additional computer resources used.

The doubling of the number of triangles in a mesh increases the computer time and memory resource requirement about four-fold. Table 3.1 shows the required time and memory to solve the square aperture problem of Section 3.1 while using 500, 1000, and 2000 triangles. As seen in Table 3.1, ninety percent of the time is spent filling up the moment matrix. If 1000 triangles are used for the meshing, results can be obtained under one minute.

Another observation is made about the benefit of the refinement process. When 500 triangles are generated in the mesh with the refinement applied, the computed results

are very similar to the results of 1000 triangle mesh without the refinement. So almost same results can be achieved with a quarter of computer resources if refinement is used on the edges and the number of triangles is halved.

	500 triangles	1000 triangles	2000 triangles
1) Total time required for the complete program (seconds)	17.87	55.92	242.69
• Filling the moment matrix (seconds)	15.19	50.58	219.83
• Solving for the coefficients matrix (seconds)	0.62	3.33	20.76
2) Memory required for the moment matrix	19 MB	76 MB	304 MB

Table 3.1 Required time and memory for solving the square aperture problem of Section 3.1 while using a mesh of 500, 1000, and 2000 triangles.

CHAPTER 4

CONCLUSIONS AND FUTURE WORK

A simple moment solution is given to numerically analyze the problem of electromagnetic scattering from and transmission through an arbitrarily shaped aperture in a thick perfectly conducting ground plane. The structure is illuminated by an incident plane electromagnetic wave. The surface equivalence principle is used to reduce this complex problem into three simpler ones. Each such problem consists of equivalent surface currents radiating in unbounded media. Therefore the free space Green's function is used for each problem. An equivalent surface magnetic current placed on the top aperture produces the scattered field in the region where the impressed sources are. The total field inside the cavity is produced by two surface equivalent magnetic currents on the apertures and an equivalent surface electric current residing on the walls of the cavity as well as on both apertures. The transmitted field on the opposite side of the impressed sources is computed by an equivalent surface magnetic current residing on the bottom aperture. Coupling between these three regions is established by satisfying boundary conditions. Tangential electric field is forced to be zero on the side walls of the cavity connecting the two semi-infinite regions, and continuity of the tangential components of both electric and magnetic fields was enforced on the apertures at both ends of the cavity. Image theory is used to simplify the equations.

The integral equations for the equivalent surface currents were numerically solved using the method of moments. The surfaces are approximated by planar triangular

patches. RWG functions are used for expansion functions. An approximate Galerkin method is used for testing.

Computed results included the surface current densities, the scattering cross sections, and the transmission coefficients. Results were computed for two square apertures connected by a square prism, two cross apertures connected by a square prism cavity, two circular apertures connected by a cylindrical cavity, and finally two circular apertures connected by a conical cavity. The computed results were validated by comparing them with available results in the literature. Very good agreement is observed. Results were further validated by investigating the effect of meshing on the convergence of the results.

The above computed results cannot be predicted by a simple theory. However, we can say that, in general the fields on the shadow side of the aperture are much smaller than those on the lit side even when the thickness of the ground plane is small.

The method is applicable to the general case where all three regions have different material parameters. Results are computed for the case where all these parameters are the same. Use of different materials is left as a future work. It will cause an increase in the electrical sizes of apertures and/or cavity. This in turn will require more computing resources.

The method is applicable to arbitrarily sized apertures and cavities. However due to limited computing resources, only problems in the resonance region, where dimensions are comparable to wavelength, are considered here. Larger structures can be considered in the future.

An advantage of the method of moments formulation compared to the finite element method is; only surface meshing is required for the method of moments. However, FEM requires a volume meshing of the problem space. Therefore the formulation introduced in this dissertation can give results very fast in a computer compared to FEM, especially for larger problems. Computed results for problems in the resonance region can be obtained under one minute.

A comprehensive analysis of sub-wavelength transmission requires a relatively thick ground plane. This in turn needs more computing resources, and hence can be a future work.

BIBLIOGRAPHY

- [1] H. A. Bethe, "Theory of diffraction by small holes," *Phys. Rev.*, vol. 66, pp. 163–182, Oct. 1944.
- [2] C. J. Bouwkamp, "On Bethe's theory of diffraction by small holes," *Philips Res. Rep.*, vol. 5, pp. 321–332, Oct. 1950.
- [3] S. B. Cohn, "Determination of aperture parameters by electrolytic-tank measurements," *Proc. IRE*, vol. 39, no. 11, pp. 1416–1421, Nov. 1951.
- [4] S. B. Cohn, "The electric polarizability of apertures of arbitrary shape," *Proc. IRE*, vol. 40, pp. 1069–1071, Sep. 1952.
- [5] N. A. McDonald, "Electric and magnetic coupling through small apertures in shield walls of any thickness," *IEEE Trans. Microwave Theory Tech.*, vol. MTT-20, no. 10, pp. 689–695, Oct. 1972.
- [6] C. C. Chen, "Transmission through a conducting screen perforated periodically with apertures," *IEEE Trans. Microwave Theory Tech.*, vol. MTT-18, pp. 627–632, Sep. 1970.
- [7] C. C. Chen, "Diffraction of electromagnetic waves by a conducting screen perforated periodically with circular holes," *IEEE Trans. Microwave Theory Tech.*, vol. MTT-19, no. 5, pp. 475–481, May 1971.
- [8] C. C. Chen, "Transmission of microwave through perforated flat plates of finite thickness," *IEEE Trans. Microwave Theory Tech.*, vol. MTT-21, no. 1, pp. 1–6, Jan. 1973.
- [9] R. F. Harrington and J. R. Mautz, "A generalized network formulation for aperture problems," *IEEE Trans. Antennas Propag.*, vol. AP-24, no. 6, pp. 870–873, Nov. 1976.
- [10] R. F. Harrington, *Field Computation by Moment Methods*. New York: Macmillan, 1968.
- [11] J. R. Mautz and R. F. Harrington, "Electromagnetic transmission through a rectangular aperture in a perfectly conducting plane," Tech. Rep. TR-76-1, Dept. Elec. Comp. Eng., Syracuse Univ., Syracuse, NY, Feb. 1976.
- [12] R. F. Harrington and J. R. Mautz, "Electromagnetic transmission through an aperture in a conducting plane," *AEÜ*, vol. 31, pp. 81–87, Feb. 1977.

- [13] J. R. Mautz and R. F. Harrington, "Transmission from a rectangular waveguide into half space through a rectangular aperture," Tech. Rep. TR-76-5, Dept. Elec. Comp. Eng., Syracuse Univ., Syracuse, New York, May 1976.
- [14] C. M. Butler and K. R. Umashankar, "Electromagnetic excitation of a wire through an aperture-perforated conducting screen," *IEEE Trans. Antennas Propag.*, vol. AP-24, no. 4, pp. 456–462, Jul. 1976.
- [15] C. M. Butler, Y. Rahmat-Samii, and R. Mittra, "Electromagnetic penetration through apertures in conducting surfaces," *IEEE Trans. Antennas Propag.*, vol. AP-26, no. 1, pp. 82–93, Jan. 1978.
- [16] D. T. Auckland and R. F. Harrington, "Electromagnetic transmission through a filled slit in a conducting plane of finite thickness, TE case," *IEEE Trans. Microwave Theory Tech.*, vol. MTT-26, pp. 499–505, Jul. 1978.
- [17] D. T. Auckland and R. F. Harrington, "A nonmodal formulation for electromagnetic transmission through a filled slot of arbitrary cross section in a thick conducting screen," *IEEE Trans. Microwave Theory Tech.*, vol. MTT-28, pp. 548–555, Jun. 1980.
- [18] R. F. Harrington, J. R. Mautz, and D. T. Auckland, "Electromagnetic coupling through apertures," Tech. Rep. TR-81-4, Dept. Elec. Comput. Eng., Syracuse Univ., Syracuse, NY, Aug. 1981.
- [19] S. M. Rao, "Electromagnetic scattering and radiation of arbitrarily-shaped surfaces by triangular patch modeling," Ph.D. Dissertation, The University of Mississippi, 1980.
- [20] S. M. Rao, D. R. Wilton, and A. W. Glisson, "Electromagnetic scattering by surfaces of arbitrary shape," *IEEE Trans. Antennas Propag.*, vol. AP-30, no. 3, pp. 409–418, May 1982.
- [21] Y. Leviatan, R. F. Harrington, and J. R. Mautz, "Electromagnetic transmission through apertures in a cavity in a thick conductor," *IEEE Trans. Antennas Propag.*, vol. AP-30, no. 6, pp. 1153–1165, Nov. 1982.
- [22] E. Arvas, "Radiation and scattering from electrically small conducting bodies of arbitrary shape," Ph.D. Dissertation, Dept. Elec. Comp. Eng., Syracuse Univ., Syracuse, NY, May 1983.
- [23] E. Arvas and R. F. Harrington, "Computation of the magnetic polarizability of conducting disks and the electric polarizability of apertures," *IEEE Trans. Antennas Propag.*, vol. AP-31, no. 5, pp. 719–725, Sep. 1983.

- [24] R. F. Harrington, "Resonant behavior of a small aperture backed by a conducting body," *IEEE Trans. Antennas Propag.*, vol. AP-30, no. 2, pp. 205–212, Mar. 1982.
- [25] C. L. I and R. F. Harrington, "Electromagnetic transmission through an aperture of arbitrary shape in a conducting screen," Technical Report TR-82-5, Syracuse University, Syracuse, NY, Apr. 1982.
- [26] T. K. Sarkar, M. F. Costa, C. L. I, and R. F. Harrington, "Electromagnetic transmission through mesh covered apertures and arrays of apertures in a conducting screen," *IEEE Trans. Antennas Propag.*, vol. AP-32, no. 9, pp. 908–913, Sep. 1984.
- [27] S. W. Hsi, R. F. Harrington, and J. R. Mautz, "Electromagnetic coupling to a conducting wire behind an aperture of arbitrary size and shape," *IEEE Trans. Antennas Propag.*, vol. AP-33, no. 6, pp. 581–587, Jun. 1985.
- [28] J. M. Jin and J. L. Volakis, "A finite element–boundary integral formulation for scattering by three-dimensional cavity-backed apertures," *IEEE Trans. Antennas Propag.*, vol. 39, no. 1, pp. 97–104, Jan. 1991.
- [29] J. M. Jin and J. L. Volakis, "Electromagnetic scattering by and transmission through a three-dimensional slot in a thick conducting plane," *IEEE Trans. Antennas Propag.*, vol. 39, no. 4, pp. 543–550, Apr. 1991.
- [30] R. Luebbers and C. Penney, "Scattering from apertures in infinite ground planes using FDTD," *IEEE Trans. Antennas Propag.*, vol. 42, no. 5, pp. 731–736, May 1994.
- [31] H. H. Park and H. J. Eom, "Electromagnetic scattering from multiple rectangular apertures in a thick conducting screen," *IEEE Trans. Antennas Propag.*, vol. 47, no. 6, pp. 1056–1060, Jun. 1999.
- [32] Y. B. Park and H. J. Eom, "Electromagnetic transmission through multiple circular apertures in a thick conducting plane," *IEEE Trans. Antennas Propag.*, vol. 52, no. 4, pp. 1049–1055, Apr. 2004.
- [33] T. Andersson, "Moment-method calculations on apertures using basis singular functions," *IEEE Trans. Antennas Propag.*, vol. 41, no. 12, pp. 1709–1716, Dec. 1993.
- [34] S. Caorsi, D. Moreno, and F. Sidoti, "Theoretical and numerical treatment of surface integrals involving the free-space Green's function," *IEEE Trans. Antennas Propag.*, vol. 41, no. 9, pp. 1296–1301, Sep. 1993.

- [35] R. D. Graglia, "On the numerical integration of the linear shape functions times the 3-D Green's function or its gradient on a plane triangle," *IEEE Trans. Antennas Propag.*, vol. 41, no. 10, pp. 1448–1455, Oct. 1993.
- [36] T. F. Eibert and V. Hansen, "On the calculation of potential integrals for linear source distributions on triangular domains," *IEEE Trans. Antennas Propag.*, vol. 43, no. 12, pp. 1499–1502, Dec. 1995.
- [37] P. Arcioni, M. Bressan, and L. Perregrini, "On the evaluation of the double surface integrals arising in the application of the boundary integral method to 3-D problems," *IEEE Trans. Microwave Theory Tech.*, vol. 45, no. 3, pp. 436–439, Mar. 1997.
- [38] D. J. Taylor, "Accurate and efficient numerical integration of weakly singular integrals in Galerkin EFIE solutions," *IEEE Trans. Antennas Propag.*, vol. 51, no. 7, pp. 1630–1637, Jul. 2003.
- [39] M. A. Khayat and D. R. Wilton, "Numerical evaluation of singular and near-singular potential integrals," *IEEE Trans. Antennas Propag.*, vol. 53, no. 10, pp. 3180–3190, Oct. 2005.
- [40] R. D. Graglia and G. Lombardi, "Machine precision evaluation of singular and nearly singular potential integrals by use of Gauss quadrature formulas for rational functions," *IEEE Trans. Antennas Propag.*, vol. 56, no. 4, pp. 981–998, Apr. 2008.
- [41] I. Bogaert and D. De Zutter, "High precision evaluation of the selfpatch integral for linear basis functions on flat triangles," *IEEE Trans. Antennas Propag.*, vol. 58, no. 5, pp. 1813–1816, May 2010.
- [42] R. F. Harrington, *Time-Harmonic Electromagnetic Fields*. New York: McGraw-Hill, 1961.
- [43] P. O. Persson and G. Strang, "A simple mesh generator in MATLAB," *SIAM Review*, vol. 46, no. 2, pp. 329–345, Jun. 2004.
- [44] C. Geuzaine and J. F. Remacle, "Gmsh: A 3-D finite element mesh generator with built-in pre- and post-processing facilities," *Int. J. Num. Meth. Eng.*, vol. 79, no. 11, pp. 1309–1331, 2009.
- [45] N. Morita, N. Kumagai, and J. R. Mautz, *Integral Equation Methods for Electromagnetics*. Boston: Artech House, 1990.

- [46] D. Worasawate, “Electromagnetic scattering from an arbitrarily shaped three-dimensional chiral body,” Ph.D. Dissertation, Syracuse University, 2002.
- [47] T. Wang, “Electromagnetic scattering from and transmission through arbitrary apertures in conducting bodies,” Ph.D. Dissertation, Syracuse University, 1989.
- [48] D. A. Dunavant, “High degree efficient symmetrical Gaussian quadrature rules,” *Int. J. Num. Meth. Eng.*, vol. 21, pp. 1129–1148, 1985.
- [49] D. R. Wilton, S. M. Rao, A. W. Glisson, D. H. Schaubert, O. M. Al-Bundak, and C. M. Butler, “Potential integrals for uniform and linear source distributions on polygonal and polyhedral domains,” *IEEE Trans. Antennas Propag.*, vol. AP-32, no. 3, pp. 276–281, Mar. 1984.
- [50] MATLAB R2009b, Natick, MA: The MathWorks Inc., 2009.

VITA

NAME OF AUTHOR: Ahmet Burak Olcen

PLACE OF BIRTH: Istanbul, Turkiye

DATE OF BIRTH: May 24, 1978

GRADUATE AND UNDERGRADUATE SCHOOLS ATTENDED:

Syracuse University, Syracuse, New York, USA

Istanbul Technical University, Istanbul, Turkiye

DEGREES AWARDED:

Master of Science in Electrical Engineering, 2002, Syracuse University

Bachelor of Science in Electronics and Comm. Eng., 1999, Istanbul Tech. Univ.

AWARDS AND HONORS:

US Patents:

1. 8,134,818 Quarter wave stub surge suppressor with coupled pins (2008)
2. 7,777,595 Multi-channel filter assemblies (2008)
3. 20090113504 Digital signal converter device (2007)
4. 20080127287 Apparatus and method for embedding/detecting an auxiliary signal within a CATV traffic stream (2006)
5. 20060195862 Trap/filter verification system and method of use thereof (2006)
6. 8,150,004 Low-pass step attenuator (2006)
7. 7,420,794 Compact spark gap for surge protection of electrical componentry (2005)
8. 7,739,719 All-pass network for data transmission over a CATV system (2004)
9. 6,930,872 Spark gap device (2003)
10. 6,784,760 Step attenuator using frequency dependent components and method of effecting signal attenuation (2002)
11. 6,697,239 Ground fault circuit interrupter for coaxial drop cable and method of operation (2002)
12. 6,510,034 Spark gap device having multiple nodes (2001)

PROFESSIONAL EXPERIENCE:

2/2007–9/2009 Co-founder and Technical Director, NBS Technology, Bursa, Turkiye

5/2000–2/2007 RF Design Engineer, Electronics Dept., PPC, Syracuse, NY

8/1999–5/2000 Research Assistant, Dept. of Electrical Engineering, Syracuse University